Single-Molecule Fluorescence Imaging of the Electrochemical Interface

Zhuoyu Peng

A dissertation

submitted in partial fulfillment of the

requirements for the degree of

Doctor of Philosophy

University of Washington

2021

Reading Committee:

Bo Zhang, Chair

Dan Fu

Robert E. Synovec

Program Authorized to Offer Degree:

Chemistry

University of Washington

Abstract

Single-Molecule Fluorescence Imaging of the Electrochemical Interface

Zhuoyu Peng

Chair of the Supervisory Committee:
Professor Bo Zhang
Department of Chemistry

In this dissertation, I firstly aim to use a solvatochromic dye, Nile red, to probe the dynamics of translocating oil emulsions through a nanopore, as well as to probe the hydrophobicity of bubble surface. Chapter 2 presents the work using Nile red as a fluorescent dye to only label oil emulsions, where we observe the collision and coalescence of single emulsion droplets at a nanopore orifice. This work is believed to have a significant impact on future studies of the stability of emulsion droplets, droplet−droplet interactions, and ion-transfer processes, and micro-scale oil/water interface. In Chapter 3, Nile red is used to probe the electrochemically generated surface nanobubbles. Nanobubble detections are observed, indicating that the bubble surface (e.g., gas/liquid interface) is hydrophobic because of the solvatochromism of Nile red. The step-wise increase in fluorescence intensity indicates multi-fluorophore labeling, possibly caused by

molecular aggregation. This work also verifies the high stability and long lifetime of surface nanobubbles. To better and further understand how fluorophores behave at the bubble surface, a series of rhodamine dyes are used to study the kinetics of fluorophore adsorption and desorption, presented in Chapter 4. Langmuir isotherm adsorption model is applied to extract the equilibrium constants of fluorophore adsorption at the bubble surface. This is the first application of the Langmuir model at the gas/liquid nano-interface. We believe that the ability to apply the Langmuir model at nano-interface would be beneficial for studies on various interfaces down to the nanoscale in the future. Lastly, in Chapter 5, some of the ongoing and future works are discussed, including combining TIRF imaging and electrochemistry measurement, dual fluorophore labeling, etc.

TABLE OF CONTENTS

LIST OF FIGURES

LIST OF TABLES

ACKNOWLEDGEMENTS

This thesis becomes a reality with the kind support and help of many individuals, and I would like to express my sincere thanks to all of them.

I cannot begin to express my sincere gratitude to my advisor Prof. Bo Zhang for his unwavering support and for imparting his knowledge and expertise throughout these years. Words fail to express how thankful I am to have you as my advisor, and it is a person like you who continues to inspire students every single day.

I am also highly indebted to my committees: Prof. Dan Fu, Prof. Robert Synovec, and Prof. Xiaohu Gao for their insightful comments and support on my research. Also, thank you to my former committee Prof. Joshua Vaughan for sharing his expertise in the field of single-molecule imaging.

My appreciation also extends to my colleagues. Dr. Rui Hao and Dr. Yunshan Fan's introduction and guidance to the world of single molecules have been motivating me to delve deeper. Thanks also go to Milomir Suvira for all those valuable and countless discussions. To Dr. Chris Gunderson, Dr. Chu Han, Dr. Samual Barlow, Dr. Peter Defnet, Dr. Todd Anderson, Dr. Hongfang Gao, Ruixuan Wan, Chris McAllister, Todd Lewis, thank you for always lending a hand when I need help. I am so blessed to work in such a great lab!

Finally, and the most importantly, I am genuinely thankful for having absolute love and encouragement from my family. My parents have been continuously supporting me throughout my life and thank you for giving me the strength and courage to reach for the stars and chase my dreams. My beloved husband, who is always by my side when times I need him the most.

Without you all, none of this would indeed be possible.

Chapter 1. INTRODUCTION

1.1 THE BIRTH OF ELECTROCHEMISTRY AND THE STUDY OF VARIOUS INTERFACIAL REGIONS

The study of electrochemistry began in the 18th century when the first modern electrical battery was invented by Alessandro Volta. The electrochemical interface, where redox reactions take place, plays an essential role in nearly all aspects of electrochemistry.[1] The study of the electrochemical interface continues to be one of the most exciting directions in modern electrochemistry research. Electrochemical reactions can take place in various interfaces, including but not limited to liquid/liquid, solid/solid, and solid/liquid interface. Specifically, I will emphasize more on the solid/liquid (electrode/electrolyte) interface in this thesis.

1.1.1 *Liquid/Liquid Interface*

Liquid/liquid interface could be polarized by an external potential, which was firstly reported by Gavach 50 years ago.[2] Charge transfer at the liquid/liquid interface between two immiscible electrolyte solutions becomes one of the most fundamental electrochemical processes to be studied.[3,4] In the liquid/liquid interface experiment, the potential is applied between two reference electrodes, and the current flows between two counter electrodes via an interfacial area (e.g., from mm^2 to nm^2).

There are three major methods to approach these liquid/liquid interface experiments: pulled glass pipettes (micro-, nano-, and dual pipettes), polymer or silicon membranes, and micro-cavity. Applications of different types of macro- or nano-liquid/liquid interfaces have been investigated in the past few decades. Girault and coworkers used a micropipette (with a water/1,2-dichloroethane(W/DCE) interface) to determine the limiting ions of an ion transfer process

because the transfer of ions from inside the pipette to the interface (e.g., egress transfer) was controlled by linear diffusion, while the transfer of ions from outside to the interface (e.g., ingress transfer) was controlled by spherical diffusion.[5] By scanning cyclic voltammetry (CV), these processes can be distinguished, and limiting ions can be determined. Later, Girault and coworkers utilized AC impedance to measure the transfer of tetramethylammonium (TMA^+) and K^+ at the micro-W/DCE interface and determine the standard rate constant (k^0) to be at least 1.6 cm s^{-1}.[6] Liquid/liquid interface also extends its applications to detect biological macromolecules. Arrigan et al. have reported the label-free detections of seven oligopeptides based on their voltammetric behaviors at the liquid/liquid interfaces The combination of micropores with stripping voltammetry allowed the limit of detection to be at submicromolar level.[7] Nanopipettes can also be used to probe surface topography. Mirkin and coworkers used a nanopipette, acting as a scanning electrochemical microscopy (SECM) tip, to image various substrates with nanoscale resolution by tip current, which was produced by reduction (or oxidation) of the mediator species at its surface.[8]

1.1.2 *Solid/Solid Interface*

Electrochemistry of solid/solid interface is more frequently studied in the solid-state battery. All-solid-state Li batteries face a challenge that the resistance at the interface between Li and the solid electrolyte is large that would severely be affecting the performance of the battery. Some traditional electrochemistry measurements like cyclic response and charge/discharge profiles are used to characterize interfacial charge transfer.[9,10] Besides electrochemical signals, Chi and coworkers used in situ scanning transmission electron microscopy (STEM) to observe the solid/solid interface (solid electrolyte – Li interface) behavior with high spatial resolution.[11]

1.1.3 *Solid/Liquid Interface (Electrode/electrolyte interface)*

Solid/liquid interface, also known as electrode/electrolyte interface, is the conventional electrochemical interfacial region that has been extensively studied over the past decades. Much of our existing knowledge about the electrochemical interface comes from ensemble measurements and *ex situ* imaging of the electrode surface. Due to its enormous complexity and highly dynamic nature, however, new imaging tools that can probe the interface *in situ* with ultrahigh spatial and temporal resolution and single-molecule sensitivity are apparently needed. Single-molecule fluorescence microscopy (SMFM) has emerged as a powerful tool that is uniquely suited for studying the electrochemical interface. SMFM is used for studying surface-immobilized single molecules, single freely diffusing molecules, single molecules as catalytic reaction indicators, and single-molecule labeling and imaging of interfacial nanobubbles at electrode/electrolyte interface. More fundamental knowledge regarding SMFM is presented in section 1.2.

1.1.3.1 Immobilization of single molecules at the electrode/electrolyte interface

To study electrode/electrolyte interface via single molecules, immobilization is necessary. There are several ways to immobilize single molecules on the surface. In Pan's work, a redox chromophore 4,4-difluoro-4-bora-3a,4a-diaza-s-indacene (BODIPY) with polystyrene was spin-cast on prepared substrates.[12] The purpose of this inert polystyrene film was to reserve the stability of individual BODIPY molecules. The fluorescence of BODIPY was turned "off" upon electrochemical oxidation, and observations of differences in fluorescence stability and intensity were explained by different charge transfer activities from the chromophore to the metal oxide surface. Electron transfer rates were also calculated for further understanding of distinct

observations of BODIPY on different substrates. Zhang et al. studied electrochemical responses of covalently bonded single methylene blue molecules on an electrode via (3-Aminopropyl)triethoxysilane (APTES) modification.[13] Also, sodium montmorillonite (SM), a member of the smectite group of clays, is a good binding material for single molecules because of its high chemical stability and high surface area.[14] SM colloid, the dispersions of nanoscale SM particles in water, was deposited on an ITO coverslip, followed by the formation of a thin transparent film. This transparent clay-modified surface not only allowed single-molecule immobilization but also enabled electrochemical measurements coupled with optical detection. The Ackerman group used this clay-modified ITO electrode to study single redox events of cresyl violet: a nonfluorescent cresyl violet can be oxidized to a fluorescent cresyl violet^{+} by a one-electron oxidation process. The fluorescent and nonfluorescent responses were observed and correlated to cyclic voltammetry scans, corresponding to the oxidized and reduced states of cresyl violet. Intensity fluctuations and blinking represented for the intermittency of the interfacial electron-transfer processes modulated by a potential scan. Meanwhile, the duration time of "on" and "off" states could be used to determine electron-transfer rates of reduction and oxidation, which was comparable to their ensemble-averaged measurements.

SMFM can also be applied to larger molecules, such as proteins. A notable mechanism called Förster (fluorescence) resonance energy transfer (FRET) is widely used in studying single proteins. FRET, developed by Theodor Förster, is a process in which an excited donor transfers energy to an acceptor via a nonradiative pathway.[15] The Aartsma group developed a FRET-based method to probe the immobilized redox proteins azurin on a gold surface, where fluorescence enhancement and quenching coexisted on the short distance regime (<2 nm).[16] The oxidized state

of azurin shows an intense absorption at ~600 nm, while it is absent in the reduced state. Voltage can be applied to manipulate the redox state of individual azurin molecules.[17]

1.1.3.2 Confining single molecules in an electrochemical cell

Developing strategies for studying single freely diffusing molecules could allow us to correlate molecular motion and collision with electron transfer at the electrode/electrolyte interface. The ability to directly probe single redox molecules on an electrode may also enable the development of highly sensitive electroanalytical sensors. Since molecules are moving randomly and quickly, it is necessary to confine their moving space.

Our group used a modified ITO electrode to confine motions of single molecules in solutions, allowing us to explore single redox events at the ITO surface.[18] An ultrathin mesoporous silica film (~70 nm in thickness) containing highly ordered parallel nanochannels (~3 nm in diameter), was electrochemically deposited onto a transparent ITO electrode. Such narrow channels allowed access to redox molecules while restricting their diffusional motions. Only when single molecules were transiently trapped in a nanochannel could they be fluorescently detected. Herein, adsorption, desorption, and redox dynamics of transiently immobilized molecules could be studied at the electrode/solution interface. Later, our group developed a diffusion-confined device---a Pt nanocell to study freely diffusing single redox molecules in solutions. [19] To make a nanocell, a Pt nanoparticle was deposited at the orifice of a laser-pulled nanopipette.[20] In the SMFM application, similarly, using a ~100 nm diameter tip, diffusional motions were constrained and the probability of transient adsorption of molecules on pipet wall was increased. Those adsorbed single molecules, herein, can be easily detected when they collide on the Pt nanoparticle electrode, which functioned as a closed bipolar nanoelectrode. Counting individual resorufin molecules at various concentrations and redox potentials offered new insights on detection

efficiency. This study demonstrated the redox reaction was observed at the electrode/solution interface in real-time.

1.1.3.3 Observation of catalytic reactions at the electrode/electrolyte interface

The ability to study the reactants and/or products of a catalytic reaction at the electrode/solution interface allows us to further understand the structure-property relationship of the catalysts, which could be beneficial for designing and developing new and more efficient catalysts. The Chen group reported the use of wide-field SMFM to study electrocatalysis on single-walled carbon nanotubes (SWNTs) with single-reaction resolution.[21] To study electrocatalysis of SWNTs at a single-molecule level, they deposited individual SWNTs onto an ITO working electrode. Under a constant reductive potential, fluorescence bursts were observed due to electrochemical reduction of resazurin to resorufin. The fact that reactions occurred at discrete locations instead of on the entire SWNTs was visually confirmed. They later discussed rate constants for possible corresponding reduction and oxidation processes and the results suggested that interfacial electron transfer kinetics between SWNTs and adsorbed molecules are dependent on the applied potential. Later, Chen group reported an innovative work for optimization of the catalyst-modified photoanode for the water-splitting process.[22] The authors used a microfluidic photoelectrochemical cell, with rutile TiO_2 nanorods deposited on an ITO electrode. By passing fluorogenic substrates, both hole and electron-based active sites were mapped out with 30 nm and 15 ms spatial and temporal resolutions, respectively.

1.1.3.4 Probing the electrochemically generated nanobubbles

Surface nanobubbles are defined as gas-filled hemispherical pockets on a surface usually with a height less than 100 nm and with a radius between 50 – 500 nm.[23–26] The very first report

on the presence of nanobubble is published in 1994, where Parker et al. proposed that the attractive force between two hydrophobic surfaces was due to the presence of nanosized bubbles on the hydrophobic surface.[27] Until 2000, nanobubbles were firstly imaged by atomic force microscopy (AFM) on various hydrophobic surfaces.[28,29] Nanobubbles have been playing a significant role in many fields, including froth flotation,[30] drug delivery,[31–33] nanomaterial engineering,[34,35] etc. More importantly, nanobubbles are of great fundamental interest due to their unexpected long-lived properties and high stability.[36–41]

Research on interfacial nanobubbles has greatly attracted a lot of attention in the past decades, including different generation methods, various detection methods, and different theories and mechanisms of nanobubble formation and long-lived stability.[28,36,37,40,42–49] Because of the small size and transparency of nanobubbles, surface nanobubbles are challenging to detect with high spatiotemporal resolution. Many techniques have been developed, such as AFM,[28,43,50,51] dark field microscopy,[52] electrochemical techniques,[53–55] infrared spectroscopy,[56] fluorescence microscopy [57–60] etc. In this section, we focus on the discussion on the detection of electrochemically generated surface nanobubbles. In the water electrolysis reaction, hydrogen and oxygen gases are generated on the cathode and anode, respectively. Insulating gas bubbles are generated from these reactions, which cover the electrode surface causing electrode deactivation. Understanding the bubble nucleation and growth therefore could provide valuable information for designing new electrochemical interfaces for improved energy efficiency.

The electrochemical technique is one of the fundamental ways to detect nanobubbles. The White group reported the usage of a single Pt nanodisk (27nm) to detect the formation of individual nanobubbles back to 2013.[54] When scanning CV over the Pt nanodisk (towards the negative direction to have water reduction), the current increased rapidly because of the H_2 production until

it reached a current peak. Then current suddenly dropped due to the bubble formation that partially blocked the proton transfer to the electrode surface. Electrochemistry is a quick and sensitive method, but it is only limited to one bubble generation and detection.

Scanning transmission X-ray microscopy (STXM) is another method to detect surface nanobubbles. The Zhang and Hu group used an STXM to detect the highly condensed oxygen gas molecules, surface nanobubbles, generated by water electrolysis.[61] They found that there was a high density of "interior" gas inside the bubble and a gas oversaturation in the water from the bubble surrounded regions. This work demonstrated the oversaturation situation on the gas aggregation behavior at the nanoscale level.

Our group later reported the usage of single fluorophore molecules to label and detect nanobubbles electrochemically generated on a macro-ITO electrode using total internal reflection fluorescence microscopy.[58,59] By optimizing the fluorophore concentration, single-molecule occupancy of the nanobubble was achieved. The single-molecule occupancy on the bubble can also be confirmed by the abrupt on/off behavior of the fluorescent puncta. The nanobubble detection was performed with a potential scan from 0 to -2 V vs Pt QRE on an ITO electrode using TIRFM, with rhodamine 6G (R6G) as the labeling molecule (Figure 1.1A). As seen in Figure 1.1B, initially, there were no R6G molecules detected. At intermediate potentials, several molecules can be seen with high fluorescent intensities. The number of fluorescence spots increased when the potential was further decreased, indicating more nanobubbles were generated at more negative potentials. The detection puncta can be located via super-resolution localization. Our results show that nanobubbles could appear 500 mV prior to reaching the thermal dynamic potential for water reduction. The intensity of each labeling R6G molecule can also be extracted, which can be used to estimate the size of the nanobubble (assuming a hemispherical shape). The negative correlation

between the puncta intensity and the applied potential indicated the growth of the nanobubble at more negative potentials. Furthermore, we used the single molecule labeling method to probe the catalytic activity of single gold nanoplates supported on an ITO electrode. The electrode potential was scanned from +0.5 to -2.0 V vs Pt QRE to reduce protons to molecular hydrogen. Nanobubbles were observed on both ITO and gold at more positive potentials. When the potential reached ~-1.6 V, however, significantly more nanobubbles were generated on the gold and its surrounding area. Interestingly, more nanobubbles were detected around the Au plate region, which was likely due to the "hydrogen spillover" effect. The electrochemically generated hydrogen atoms can rapidly diffuse from the gold catalyst to the surrounding area where they form H_2 molecules. Later, our group successfully imaged both H_2 and O_2 using the Au/Pd alloy modified ITO electrode. O_2 generation was not observed in the previous study possibly due to the low catalytic activity of the ITO electrode for oxygen evolution reaction (OER). Herein, by depositing a thin layer (30nm) of Au/Pd on ITO, we can increase the catalytic activity of ITO and retain the transparency of the electrode. O_2 nanobubbles were generated and detected at an early stage during oxygen evolution reaction, while H_2 nanobubbles were detected was "delayed". This late H_2 nanobubble generation could be attributed to the storage or hydrogen adsorption property of the Au/Pd alloy ITO electrode.

1.2 Single-Molecule Fluorescence Microscopy

Single-molecule fluorescence microscopy (SMFM) is based on conventional fluorescence microscopy with its unique characteristics.[62–64] A key factor of SMFM is its ability to distinguish and resolve single fluorescent molecules from the background signal. Traditional epi-fluorescence microscopy illuminates the whole sample volume at the same time without selection yielding a higher fluorescence background. Therefore, it could be very challenging to detect single

fluorescent molecules with epi-fluorescence. Some of the most common strategies for detecting single molecules, especially in the electrochemistry systems, involve minimizing the illumination/sampling volume. The emission from the target fluorophores can be detected more easily with reduced background. Two major approaches can be adapted for achieving a higher signal/noise ratio in the optical microscopy: 1) selectively collecting the emission from the molecules on the focal plane, such as confocal microscopy, and 2) selectively exciting the molecules on the focal plane, such as total internal reflection fluorescence (TIRF) microscopy. Alternatively, one can also reduce the background signal by creating a spatially confined structure and only allowing molecules of interest to be present and detected. In this thesis, we primarily focus on the discussion on TIRF.

1.2.1 *Total Internal Reflection Fluorescence Microscopy*

TIRF microscopy remains one of the most useful imaging methods for SMFM.[63] The key concept of TIRF is based on illuminating the sample with an ultra-thin evanescent field (<200 nm) on the interface generated from the total internal reflection phenomenon. When light is incident on an interface from a medium with a higher refractive index (e.g., glass, 1.5, n_1) into another medium with a lower refractive index (e.g. water, 1.33, n_2) with an incident angle greater than a certain angle (critical angle, $\theta = \arcsin(n_2/n_1)$), no transmission light can be seen and the incident light will be totally reflected, i.e., the total internal reflection phenomenon. The electromagnetic field extends across the interface into the medium with a lower refractive index with an exponential decay intensity with distance from the interface. The extended electromagnetic field called the "evanescent field", can be used to selectively illuminate molecules near the electrode/solution interface allowing detection of single molecules.

Although TIRF can be achieved with both prism-based and objective-based setups, objective-based TIRF has been used more frequently for single-molecule studies. Since no scanning is needed, the entire field of view can be imaged simultaneously at a high acquisition speed. Combined with the super-resolution localization techniques, the spatial resolution of TIRF can be as high as ~10 nm.[65–67] All those unique features allow TIRF to image the electrochemical interface in real-time with high spatiotemporal resolution. It is now possible to correlate morphological and structural information obtained from electron microscopy with the electrochemical properties from optical microscopy and reveal the heterogeneity of the electrode surface.[22,58,68]

1.2.2 *Super-resolution Microscopy---Stochastic Optical Reconstruction Microscopy (STORM)*

The resolution of a visible light microscope is usually taken to be about half of the wavelength, with any objects smaller than this distance are considered as diffraction-limited spots. Super-resolution microscopy is a powerful optical approach that circumvents the diffraction limit of conventional optical microscopy to achieve nanometer resolution.[69] Several super-resolution microscopy methods have been developed for imaging ultrafine features; these include near-field scanning optical microscopy (NSOM), stimulated emission depletion microscopy (STED), photoactivated localization microscopy (PALM), or stochastic optical reconstruction microscopy (STORM), and structured illumination microscopy (SIM).[70] In this thesis, I especially focused on the usage of STORM/PALM, which has been greatly applied since its first introduction in 2006.[65,66] The fundamental principle behind STORM is that photoswitchable molecules will be activated sequentially and lead to consecutive emissions that enable precise localization. All should take place before a molecule enters a dark state or is deactivated by photobleaching. Also,

to distinguish individual fluorescent molecules, they need to be activated separately by a distance greater than the Abbe diffraction limit.[69,71–76] The point-spread function of the fluorescent puncta can be easily obtained through a simple 2D Gaussian fitting of the measured photon signal.[77] By utilizing STORM, the diffraction limit is solved, allowing imaging at a truly molecular-scale resolution. Single fluorophore molecules are seen as discrete puncta on an electrochemical interface, which perfectly meet the single emitter requirement. This allows one to locate the molecules with high precision and to image surface heterogeneity at high spatial resolution by single molecule fluorescence microscopy.[78] Interfacial properties can be studied by utilizing this technique, presented in Chapter 3 and Chapter 4.

1.2.3 *A unique probing fluorophore --- Nile red*

To probe a hydrophilic/hydrophobic interface, Nile red, 9-diethylamino-5H-benzo[α]phenoxazin-5-one, has attracted plenty of attention due to its interesting photo-physical properties.[79–81] Nile red has a flat aromatic core connected with a diethylamino terminal group. In a polar solvent, intramolecular charge transfer during the S0 → S1 transition induces a large change in the molecule's dipole moment, resulting in a redshift of emission.[82] This corresponds to the charge transfer between the diethylamino group which acts as an electron donor and the aromatic acceptor system (quinoid), resulting in a twisted intramolecular charge transfer state (TICT) in a more polar environment.[83] Nile red is sensitive to the local polarity of the medium; therefore, it has been applied to probe the local polarity in various systems, including micelles, proteins, and liposomes.[84–87] Also, encapsulation of Nile red has been discussed in terms of hydrophobic interactions between the dye molecules and the nonpolar environment.[88,89]

1.3 FIGURES

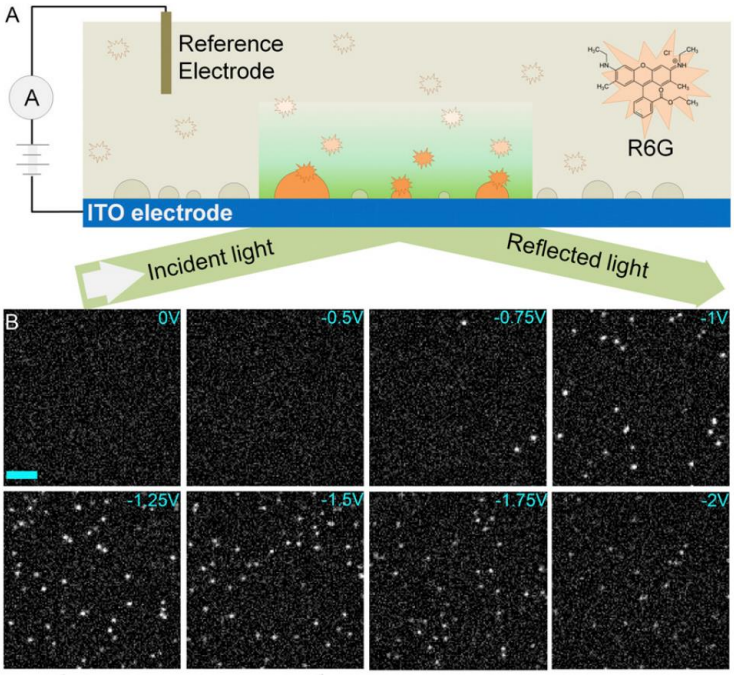

Figure 1.1 Nanobubble detections using single molecule fluorescence microscopy

(A) A scheme of the experimental setup used for imaging H_2 nanobubbles in electrocatalytic water splitting. H_2 nanobubbles generated on an ITO surface are labeled by single R6G molecules and imaged by TIRF microscopy. (B) A series of TIRF images of a 22.8 × 22.8-μm^2 area on an ITO electrode taken from a potential scan from 0 V to −2.0 V at 100 mV/s vs. Pt QRE in water containing 1 M Na_2SO_4 and 10 nM R6G. Fluorescence images were recorded at 19.81 frames per second with a 50-ms exposure time. (Scale bar, 5 μm).[58] Copyright 2018 the US National Academy of Sciences.

1.4 REFERENCES

(1) Anderson, A. B. Concepts and Computational Methods for the Electrochemical Interface and Applications: Past, Present, and Future. *Curr. Opin. Electrochem.* **2017**, *1*, 27–33.

(2) Gavach, C.; D'Epenoux, B. Chronopotentiometric Investigation of the Diffusion Overvoltage at the Interface between Two Non-Miscible Solutions. II. Potassium Halide Aqueous Solution-Hexadecyl-Trimethylammonium Picrate Nitrobenzene Solution. *J. Electroanal. Chem.* **1974**, *55*, 59–67.

(3) Samec, Z. Dynamic Electrochemistry at the Interface between Two Immiscible Electrolytes. *Electrochim. Acta* **2012**, *84*, 21–28.

(4) Liu, S.; Li, Q.; Shao, Y. Electrochemistry at Micro- and Nanoscopic Liquid/Liquid Interfaces. *Chem. Soc. Rev.* **2011**, *40*, 2236–2253.

(5) Stewart, A. A.; Shao, Y.; Pereira, C. M.; Girault, H. H. Micropipette as a Tool for the Determination of the Ionic Species Limiting the Potential Window at Liquid/Liquid Interfaces. *J. Electroanal. Chem.* **1991**, *305*, 135–139.

(6) Beattie, P. D.; Delay, A.; Girault, H. H. Investigation of the Kinetics of Ion and Assisted Ion Transfer by the Technique of Ac Impedance of the Micro-Ities. *Electrochim. Acta* **1995**, *40*, 2961–2969.

(7) Sairi, M.; Arrigan, D. W. M. Electrochemical Detection of Ractopamine at Arrays of Micro-Liquid | Liquid Interfaces. *Anal. Chem* **2008**, *80*, 5743–5749.

(8) Sun, P.; Mirkin, M. V. Scanning Electrochemical Microscopy with Slightly Recessed Nanotips. *Anal. Chem.* **2007**, *79*, 5809–5816.

(9) Liu, B.; Gong, Y.; Fu, K.; Han, X.; Yao, Y.; Pastel, G.; Yang, C.; Xie, H.; Wachsman, E. D.; Hu, L. Garnet Solid Electrolyte Protected Li-Metal Batteries. *ACS Appl. Mater. Interfaces* **2017**, *9*, 18809–18815.

(10) Zhang, Z.; Zhao, Y.; Chen, S.; Xie, D.; Yao, X.; Cui, P.; Xu, X. An Advanced Construction Strategy of All-Solid-State Lithium Batteries with Excellent Interfacial Compatibility and Ultralong Cycle Life. *J. Mater. Chem. A* **2017**, *5*, 16984–16993.

(11) Ma, C.; Cheng, Y.; Yin, K.; Luo, J.; Sharafi, A.; Sakamoto, J.; Li, J.; More, K. L.; Dudney, N. J.; Chi, M. Interfacial Stability of Li Metal-Solid Electrolyte Elucidated via in Situ Electron Microscopy. *Nano Lett.* **2016**, *16*, 7030–7036.

(12) Liu, J.; Hill, C. M.; Pan, S.; Liu, H. Interfacial Charge Transfer Events of BODIPY Molecules: Single Molecule Spectroelectrochemistry and Substrate Effects. *Phys. Chem. Chem. Phys.* **2014**, *16*, 23150–23156.

(13) Zhang, W.; Caldarola, M.; Pradhan, B.; Orrit, M. Gold Nanorod Enhanced Fluorescence Enables Single-Molecule Electrochemistry of Methylene Blue. *Angew. Chemie - Int. Ed.* **2017**, *56*, 3566–3569.

(14) Lei, C.; Hu, D.; Ackerman, E. Clay Nanoparticle-Supported Single-Molecule Fluorescence Spectroelectrochemistry.

(15) Waters, J. C. Accuracy and Precision in Quantitative Fluorescence Microscopy. *J. Cell Biol.* **2009**, *185*, 1135–1148.

(16) Elmalk, A. T.; Salverda, J. M.; Tabares, L. C.; Canters, G. W.; Aartsma, T. J. Probing Redox Proteins on a Gold Surface by Single Molecule Fluorescence Spectroscopy. *J. Chem. Phys.* **2012**, *136*.

(17) Akkilic, N.; Van Der Grient, F.; Kamran, M.; Sanghamitra, N. J. M. Chemically-Induced Redox Switching of a Metalloprotein Reveals Thermodynamic and Kinetic Heterogeneity, One Molecule at a Time. *Chem. Commun.* **2014**, *50*, 14523–14526.

(18) Lu, J.; Fan, Y.; Howard, M. D.; Vaughan, J. C.; Zhang, B. Single-Molecule Electrochemistry on a Porous Silica-Coated Electrode. *J. Am. Chem. Soc.* **2017**, *139*, 2964–2971.

(19) Fan, Y.; Hao, R.; Han, C.; Zhang, B. Counting Single Redox Molecules in a Nanoscale Electrochemical Cell. *Anal. Chem* **2018**, *90*, 6.

(20) Hao, R.; Zhang, B. Nanopipette-Based Electroplated Nanoelectrodes. *Anal. Chem.* **2016**, *88*, 614–620.

(21) Xu, W.; Shen, H.; Kim, Y. J.; Zhou, X.; Liu, G.; Park, J.; Chen, P. Single-Molecule Electrocatalysis by Single-Walled Carbon Nanotubes. *Nano Lett.* **2009**, *9*, 3968–3973.

(22) Sambur, J. B.; Chen, T. Y.; Choudhary, E.; Chen, G.; Nissen, E. J.; Thomas, E. M.; Zou, N.; Chen, P. Sub-Particle Reaction and Photocurrent Mapping to Optimize Catalyst-Modified Photoanodes. *Nature* **2016**, *530*, 77–80.

(23) Lohse, D.; Zhang, X. Surface Nanobubbles and Nanodroplets. *Rev. Mod. Phys.* **2015**, *87*, 981–1035.

(24) Peng, H.; Birkett, G. R.; Nguyen, A. V. Progress on the Surface Nanobubble Story: What Is in the Bubble? Why Does It Exist? *Adv. Colloid Interface Sci.* **2015**, *222*, 573–580.

(25) Alheshibri, M.; Qian, J.; Jehannin, M.; Craig, V. S. J. A History of Nanobubbles. *Langmuir* **2016**, *32*, 11086–11100.

(26) Craig, V. S. J. Very Small Bubbles at Surfaces - The Nanobubble Puzzle. *Soft Matter* **2011**, *7*, 40–48.

(27) Parker, J. L.; Claesson, P. M.; Attard, P. Bubbles, Cavities, and the Long-Ranged Attraction between Hydrophobic Surfaces. *J. Phys. Chem.* **1994**, *98*, 8468–8480.

(28) Lou, S.-T.; Ouyang, Z.-Q.; Zhang, Y.; Li, X.-J.; Hu, J.; Li, M.-Q.; Yang, F.-J. Nanobubbles on Solid Surface Imaged by Atomic Force Microscopy. *J. Vac. Sci. Technol., B Microelectron. Process. Phenom.* **2000**, *18*, 2573.

(29) Ishida, N.; Inoue, T.; Miyahara, M.; Higashitani, K. Nano Bubbles on a Hydrophobic Surface in Water Observed by Tapping-Mode Atomic Force Microscopy. *Langmuir* **2000**, *16*, 6377–6380.

(30) Calgaroto, S.; Wilberg, K. Q.; Rubio, J. On the Nanobubbles Interfacial Properties and Future Applications in Flotation. *Miner. Eng.* **2014**, *60*, 33–40.

(31) Batchelor, D. V. B.; Abou-Saleh, R. H.; Coletta, P. L.; McLaughlan, J. R.; Peyman, S. A.; Evans, S. D. Nested Nanobubbles for Ultrasound-Triggered Drug Release. *ACS Appl. Mater. Interfaces* **2020**, *12*, 29085–29093.

(32) Cavalli, R.; Bisazza, A.; Trotta, M.; Argenziano, M.; Civra, A.; Donalisio, M.; Lembo, D. New Chitosan Nanobubbles for Ultrasound-Mediated Gene Delivery: Preparation and in Vitro Characterization. *Int. J. Nanomedicine* **2012**, *7*, 3309–3318.

(33) Nguyen, A. T.; Wrenn, S. P. Acoustically Active Liposome-Nanobubble Complexes for Enhanced Ultrasonic Imaging and Ultrasound-Triggered Drug Delivery. *Wiley Interdiscip. Rev. Nanomedicine Nanobiotechnology* **2014**, *6*, 316–325.

(34) Huango, C.; Jiangs, J.; Lu, M.; Sun, L.; Meletis, E. I.; Hao, Y. Capturing Electrochemically Evolved Nanobubbles by Electroless Deposition. A Facile Route to the Synthesis of Hollow Nanoparticles. *Nano Lett.* **2009**, *9*, 4297–4301.

(35) Hui, F.; Li, B.; He, P.; Hu, J.; Fang, Y. Electrochemical Fabrication of Nanoporous Polypyrrole Film on HOPG Using Nanobubbles as Templates. *Electrochem. commun.* **2009**, *11*, 639–642.

(36) Ducker, W. A. Contact Angle and Stability of Interfacial Nanobubbles. *Langmuir* **2009**, *25*, 8907–8910.

(37) Zhang, X. H.; Quinn, A.; Ducker, W. A. Nanobubbles at the Interface between Water and a Hydrophobic Solid. *Langmuir* **2008**, *24*, 4756–4764.

(38) Zhang, X. H.; Maeda, N.; Craig, V. S. J. Physical Properties of Nanobubbles on Hydrophobic Surfaces in Water and Aqueous Solutions. *Langmuir* **2006**, *22*, 5025–5035.

(39) Brenner, M. P.; Lohse, D. Dynamic Equilibrium Mechanism for Surface Nanobubble Stabilization. *Phys. Rev. Lett.* **2008**, *101*, 1–4.

(40) Zhang, X.; C Chan, D. Y.; Wang, D.; Maeda, N. Stability of Interfacial Nanobubbles. *Langmuir* **2013**, *29*, 1017–1023.

(41) Sun, Y.; Xie, G.; Peng, Y.; Xia, W.; Sha, J. Stability Theories of Nanobubbles at Solid–Liquid Interface: A Review. *Colloids Surfaces A Physicochem. Eng. Asp.* **2016**, *495*, 176–186.

(42) Zhang, X. H.; Li, G.; Maeda, N.; Hu, J. Removal of Induced Nanobubbles from Water/Graphite Interfaces by Partial Degassing. *Langmuir* **2006**, *22*, 9238–9243.

(43) Zhang, L.; Zhang, Y.; Zhang, X.; Li, Z.; Shen, G.; Ye, M.; Fan, C.; Fang, H.; Hu, J. Electrochemically Controlled Formation and Growth of Hydrogen Nanobubbles. *Langmuir* **2006**, *22*, 8109–8113.

(44) Yang, S.; Tsai, P.; Kooij, E. S.; Prosperetti, A.; Zandvliet, H. J. W.; Lohse, D. Electrolytically Generated Nanobubbles on Highly Orientated Pyrolytic Graphite Surfaces. *Langmuir* **2009**, *25*, 1466–1474.

(45) Liu, Y.; Zhang, X. Nanobubble Stability Induced by Contact Line Pinning. *J. Chem. Phys.* **2013**, *138*.

(46) Lou, S.; Gao, J.; Xiao, X.; Li, X.; Li, G.; Zhang, Y.; Li, M.; Sun, J.; Li, X.; Hu, J. Studies of Nanobubbles Produced at Liquid/Solid Interfaces. *Mater. Charact.* **2002**, *48*, 211–214.

(47) Zhang, X. H.; Zhang, X.; Sun, J.; Zhang, Z.; Li, G.; Fang, H.; Xiao, X.; Zeng, X.; Hu, J. Detection of Novel Gaseous States at the Highly Oriented Pyrolytic Graphite-Water Interface. *Langmuir* **2007**, *23*, 1778–1783.

(48) Van Limbeek, M. A. J.; Seddon, J. R. T. Surface Nanobubbles as a Function of Gas Type. *Langmuir* **2011**, *27*, 8694–8699.

(49) Li, D.; Pan, Y.; Zhao, X.; Bhushan, B. Study on Nanobubble-on-Pancake Objects Forming at Polystyrene/ Water Interface. **2016**.

(50) Tyrrell, J. W. G.; Attard, P. Images of Nanobubbles on Hydrophobic Surfaces and Their Interactions. *Phys. Rev. Lett.* **2001**, *87*, 1–4.

(51) Ishida, N.; Sakamoto, M.; Miyahara, M.; Higashitani, K. Attraction between Hydrophobic Surfaces with and without Gas Phase. *Langmuir* **2000**, *16*, 5681–5687.

(52) Li, S.; Du, Y.; He, T.; Shen, Y.; Bai, C.; Ning, F.; Hu, X.; Wang, W.; Xi, S.; Zhou, X. Nanobubbles: An Effective Way to Study Gas-Generating Catalysis on a Single Nanoparticle. *J. Am. Chem. Soc.* **2017**, *139*, 14277–14284.

(53) German, S. R.; Edwards, M. A.; Chen, Q.; White, H. S. Laplace Pressure of Individual H2 Nanobubbles from Pressure-Addition Electrochemistry. *Nano Lett.* **2016**, *16*, 6691–6694.

(54) Luo, L.; White, H. S. Electrogeneration of Single Nanobubbles at Sub-50-Nm-Radius Platinum Nanodisk Electrodes. *Langmuir* **2013**, *29*, 11169–11175.

(55) German, S. R.; Chen, Q.; Edwards, M. A.; White, H. S. Electrochemical Measurement of Hydrogen and Nitrogen Nanobubble Lifetimes at Pt Nanoelectrodes. *J. Electrochem. Soc.* **2016**, *163*, H3160–H3166.

(56) Zhang, X. H.; Khan, A.; Ducker, W. A. A Nanoscale Gas State. *Phys. Rev. Lett.* **2007**, *98*, 136101.

(57) Chan, C. U.; Ohl, C. D. Total-Internal-Reflection-Fluorescence Microscopy for the Study of Nanobubble Dynamics. *Phys. Rev. Lett.* **2012**, *109*, 174501.

(58) Hao, R.; Fan, Y.; Howard, M. D.; Vaughan, J. C.; Zhang, B. Imaging Nanobubble Nucleation and Hydrogen Spillover during Electrocatalytic Water Splitting. *Proc. Natl. Acad. Sci. U. S. A.* **2018**, *115*, 5878–5883.

(59) Suvira, M.; Zhang, B. Effect of Surfactant on Electrochemically Generated Surface Nanobubbles. *Anal. Chem.* **2021**, 5170–5176.

(60) Hao, R.; Fan, Y.; Anderson, T. J.; Zhang, B. Imaging Single Nanobubbles of H2 and O2 during the Overall Water Electrolysis with Single-Molecule Fluorescence Microscopy. *Anal. Chem.* **2020**, *92*, 3682–3688.

(61) Zhou, L.; Wang, X.; Shin, H. J.; Wang, J.; Tai, R.; Zhang, X.; Fang, H.; Xiao, W.; Wang, L.; Wang, C.; et al. Ultrahigh Density of Gas Molecules Confined in Surface Nanobubbles in Ambient Water. *J. Am. Chem. Soc.* **2020**.

(62) Shashkova, S.; Leake, M. C. Single-Molecule Fluorescence Microscopy Review: Shedding New Light on Old Problems. *Biosci. Rep.* **2017**, *37*, 1–19.

(63) Moerner, W. E.; Fromm, D. P. Methods of Single-Molecule Fluorescence Spectroscopy and Microscopy. *Rev. Sci. Instrum.* **2003**, *74*, 3597–3619.

(64) Lei, C.; Hu, D.; Ackerman, E. J. Single-Molecule Fluorescence Spectroelectrochemistry of Cresyl Violet. *Chem. Commun.* **2008**, *7345*, 5490–5492.

(65) Rust, M.; Bates, M.; Zhuang, X. Sub-Diffraction-Limit Imaging by Stochastic Optical Reconstruction Microscopy (STORM). *Nat. Methods* **2006**, *3*, 793–795.

(66) Betzig, E.; Patterson, G. H.; Sougrat, R.; Lindwasser, O. W.; Olenych, S.; Bonifacino, J. S.; Davidson, M. W.; Lippincott-Schwartz, J.; Hess, H. F. Imaging Intracellular Fluorescent Proteins at Nanometer Resolution. *Science (80-.).* **2006**, *313*, 1642–1645.

(67) Andresen, M.; Stiel, A. C.; Fölling, J.; Wenzel, D.; Schönle, A.; Egner, A.; Eggeling, C.; Hell, S. W.; Jakobs, S. Photoswitchable Fluorescent Proteins Enable Monochromatic Multilabel Imaging and Dual Color Fluorescence Nanoscopy. *Nat. Biotechnol.* **2008**, *26*, 1035–1040.

(68) Mao, X.; Liu, C.; Hesari, M.; Zou, N.; Chen, P. Super-Resolution Imaging of Non-Fluorescent Reactions via Competition. *Nat. Chem.* **2019**, *11*.

(69) Huang, B.; Bates, M.; Zhuang, X. Super-Resolution Fluorescence Microscopy. *Annu. Rev. Biochem.* **2009**, *78*, 993–1016.

(70) Sydor, A. M.; Czymmek, K. J.; Puchner, E. M.; Mennella, V. Super-Resolution Microscopy: From Single Molecules to Supramolecular Assemblies. *Trends Cell Biol.* **2015**, *25*, 730–748.

(71) Betzig, E. Proposed Method for Molecular Optical Imaging. *Opt. Lett.* **1995**, *20*, 237.

(72) Schindler, H.; Feher, G. Imaging of Single Molecule Diffusion. *Proc. Natl. Acad. Sci. U. S. A.* **1996**, *93*, 2926–2929.

(73) Lacoste, T. D.; Michalet, X.; Pinaud, F.; Chemla, D. S.; Alivisatos, A. P.; Weiss, S. Ultrahigh-Resolution Multicolor Colocalization of Single Fluorescent Probes. *Proc. Natl. Acad. Sci. U. S. A.* **2000**, *97*, 9461–9466.

(74) Huang, B.; Babcock, H.; Zhuang, X. Breaking the Diffraction Barrier: Super-Resolution Imaging of Cells. *Cell* **2010**, *143*, 1047–1058.

(75) Hell, S. W. Microscopy and Its Focal Switch. *Nat. Methods* **2009**, *6*, 24–32.

(76) Hell, S. W. Far-Field Optical Nanoscopy. *Science (80-.).* **2007**, *316*, 1153–1158.

(77) Huang, B.; Wang, W.; Bates, M.; Zhuang, X. Three-Dimensional Super-Resolution Imaging by Stochastic Optical Reconstruction Microscopy. *Science (80-.).* **2008**, *319*, 810–813.

(78) Fernández-Suárez, M.; Ting, A. Y. Fluorescent Probes for Super-Resolution Imaging in Living Cells. *Nat. Rev. Mol. Cell Biol.* **2008**, *9*, 929–943.

(79) Greenspan, P.; Fowler, S. D. Spectrofluorometric Studies of the Lipid Probe, Nile Red. *J. Lipid Res.* **1985**, *26*, 781–789.

(80) Deye, J. F.; Berger, T. A.; Anderson, A. G. Nile Red as a Solvatochromic Dye for Measuring Solvent Strength in Normal Liquids and Mixtures of Normal Liquids with Supercritical and Near Critical Fluids. *Anal. Chem.* **1990**, *62*, 1552.

(81) Reichardt, C. Solvatochromic Dyes as Solvent Polarity Indicators. *Chem. Rev.* **1994**, *94*, 2319–2358.

(82) Teo, W.; Caprariello, A. V.; Morgan, M. L.; Luchicchi, A.; Schenk, G. J.; Joseph, J. T.; Geurts, J. J. G.; Stys, P. K. Nile Red Fluorescence Spectroscopy Reports Early Physicochemical Changes in Myelin with High Sensitivity. *Proc. Natl. Acad. Sci. U. S. A.* **2021**, *118*, 1–11.

(83) Dutta, A. K.; Kamada, K.; Ohta, K. Spectroscopic Studies of Nile Red in Organic Solvents and Polymers. *J. Photochem. Photobiol. A Chem.* **1995**, *93*, 57–64.

(84) Datta, A.; Mandal, D.; Pal, S. K.; Bhattacharyya, K. Intramolecular Charge Transfer Processes in Confined Systems. Nile Red in Reverse Micelles. *J. Phys. Chem. B* **1997**, *101*, 10221–10225.

(85) Kurniasih, I. N.; Liang, H.; Choudhary Mohr, P.; Khot, G.; Rgen, J.; Rabe, P.; Mohr, A. Nile Red Dye in Aqueous Surfactant and Micellar Solution. *Langmuir* **2015**.

(86) Sackett, D. L.; Wolff, J. Nile Red as a Polarity-Sensitive Fluorescent Probe of Hydrophobic Protein Surfaces. *Anal. Biochem.* **1987**, *167*, 228–234.

(87) Mukherjee, S.; Raghuraman, H.; Chattopadhyay, A. Membrane Localization and Dynamics of Nile Red: Effect of Cholesterol. *Biochim. Biophys. Acta - Biomembr.* **2007**, *1768*, 59–66.

(88) Gillies, E. R.; Fréchet, J. M. J. A New Approach towards Acid Sensitive Copolymer Micelles for Drug Delivery. *Chem. Commun.* **2003**, *3*, 1640–1641.

(89) Copolymers, L.; Gillies, E. R.; Jonsson, T. B.; Fre, J. M. J. Stimuli-Responsive Supramolecular Assemblies Of. **2004**, No. c, 11936–11943.

Chapter 2. STUDY ON THE COLLISION AND COALESCENCE OF OIL EMULSIONS USING NILE RED[1]

2.1 ABSTRACT

Oil/water interface or emulsion oil droplets has rarely been studied in the field of electrochemistry. Here, we describe the use of a quartz pipet nanopore to study the collision and coalescence of individual emulsion oil droplets and their subsequent nanopore translocation. Specially, we use Nile red, a solvatochromic dye, to selectively label the oil emulsion droplets. Collision and coalescence of single toluene droplets at a nanopore orifice are driven primarily by electroosmosis and electrophoresis and lead to the fast growth of a trapped oil droplet. This results in a stepwise current response due to the coalesced oil droplet increasing its volume and its ability to partially block the nanopore's ionic current, allowing us to use the resistive-pulse method to resolve single droplet collisions. Further growth of the trapped oil droplet leads to a complete blockage of the nanopore and a nearly 100% current decay. The trapped oil droplet shows enormous mechanical stability at lower voltages and stays in its trapped status for hundreds of seconds. An increased voltage can be used to drive the trapped droplet into the pipet pore within several milliseconds. Simultaneous fluorescence imaging and amperometry were performed to examine droplet collision, coalescence, and translocation, further confirming the proposed mechanism of droplet-nanopore interaction. This work has demonstrated that the unique properties of Nile red facilitate our study at the oil/water interface.

[1] This chapter is adapted with permission from: Christopher G. G.; Zhuoyu P.; and Bo, Z; "Collision and Coalescence of Single Attoliter Oil Droplets on a Pipet Nanopore" *Langmuir* 2018, 34, 2699−2707. Copyright (2018) American Chemical Society.

2.2 INTRODUCTION

Nanopores are nanometer-scale apertures formed in a biological or artificial membrane that can act as ultrafast, highly sensitive, and selective sensors for various analyte species ranging from small molecules, viruses, single-stranded DNA, and RNA to larger nanoparticles.[1–10] Nanopore sensors often detect individual analyte molecules and particles by a resistive-pulse mechanism, also known as the Coulter-counter method.[11] In such measurements, one normally holds a constant voltage across the nanopore membrane while measuring the transient changes to the nanopore's ionic current when analyte species pass through or interact with the pore orifice. In a simple case, a transient decrease in the ionic current is anticipated when an analyte particle translocates through the nanopore due to the particle partially blocking the flow of the ions. Nanopore-based sensing is fast and simple and can provide useful information about the analyte particle, such as shape, electrophoretic mobility, charge, and size. The detection frequency can be used to analyze particle concentration. Based on the shape and duration of the current pulse, one can also obtain information about the pore geometry.[12]

Most of the previous nanopore studies have focused on the use of small molecules, larger polymers, and hard particles. Despite the enormous progress, only a few studies have used soft particles such as liposomes, microgels, and oil emulsions.[13,14] Their elasticity permits soft particles which are larger than the nanopore to pass through the orifice. Elastic deformation of soft particles can also occur in the concentrated electric field at the nanopore orifice.[15,16] The structure of soft nanoparticles can result in a separate volume within the particle with contents that can differ from that of the outside electrolyte solution.[17] Emulsions are metastable dispersions of small droplets of one liquid in a different immiscible liquid. Depending on their droplet size, emulsions can be categorized into microemulsions (droplet size >200 nm) and nanoemulsions (droplet size between

50 and 200 nm).[18] Emulsions are widely used in a variety of applications including cosmetics, painting, lubricating, and the food industry.[19,20] Unlike microemulsions, nanoemulsions are considered only kinetically stable due to their small droplet size and high surface energy. Two general pathways have been considered for emulsion destruction: (1) Ostwald ripening or diffusion of dispersed phase through the continuous phase and (2) droplet coalescence.[20] As a popular method, emulsions can be characterized using dynamic light scattering (DLS) to measure their size distribution and stability. Bard and co-workers have recently proposed an interesting method to use electrochemistry to study the collision of individual emulsion droplets on the surface of an ultramicroelectrode (UME).[21]

Here we use a laser-pulled quartz pipet nanopore and the resistive-pulse mechanism to observe the dynamic collision, coalescence, and translocation of individual emulsion droplets. The emulsions we use in this work are toluene nanodroplets dispersed in water and are prepared based on chemistry described previously.[21] The toluene emulsion droplets are mixed and emulsified with an ionic liquid, trihexyltetradecyl-phosphonium bis(trifluoromethylsulfonyl)amide (IL-PA). The ionic liquid acts as an emulsifier to provide stability through particle surface charge as well as an electrolyte to increase the conductivity of the droplet. In this article, we first describe the observation, characterization, and analysis of the phenomenon of collision and coalescence of single oil droplets at the nanopore orifice and the voltage-dependent translocation of a trapped droplet. We then use this method to trap a droplet in the orifice with a highly resistive seal to perform single-droplet voltammetry. The ion transfer voltammogram is obtained and explained to demonstrate the unique capability of this method for repeatable electrochemical interrogation of a solitary attoliter oil droplet volume. Finally, a lipophilic dye is added to the droplet, and the collision, coalescence, and translocation processes are monitored with fluorescence microscopy in

real-time. To our knowledge, this is the first time the nanopore method is used to study collision and coalescence of individual emulsion droplets and ion-transfer electrochemistry across a single attoliter oil droplet. We believe this method will have significant impacts on future studies of the stability of emulsion droplets, droplet-droplet interactions, and ion-transfer processes across the oil/water interface.

2.3 Experimental Section

2.3.1 *Nanopore Fabrication and Characterization.*

Quartz pipet pores were fabricated using a P-2000 laser puller (Sutter Instrument). Quartz capillaries of dimensions 0.7 mm i.d. and 1.0 mm o.d. with filament (Sutter Instrument) were rinsed with isopropanol and dried before laser-pulling with a previously reported recipe.[22] Pulling parameters were heat 450-470, filament 1, velocity 30, delay 145, and pull 175 where a higher heat parameter resulted in a smaller diameter nanopipette. Nanopores were electrically tested in aqueous 5 mM tetrabutylammonium chloride (TBACl, 97%, Sigma-Aldrich) that had been filtered through a 200 nm PTFE syringe filter prior to emulsion droplet experiments. The inside of the nanopipet was filled with an aqueous 5 mM TBACl solution and then submerged in the same solution. Ag/AgCl quasi-reference electrodes (QRE) were made by leaving 0.5 mm silver wire (Alfa-Aesar) in ultrableach (Tough Guy brand) until the wires turned a noticeable shade of purple-gray. The Ag/AgCl QREs were then placed into the back of the nanopipet and the 5 mM TBACl solution. The potential was controlled by an EG&G PAR Model 175 function generator connected to a Dagan Chem- Clamp potentiostat. The potentiostat was interfaced to a Dell PC through a National Instruments 6281 DAQ card and a National Instruments BNC-2120 breakout box with signal data recorded with a homemade LabVIEW program. The potential was scanned between -

1 and +1 V at 100 mV/s until a stable i−V response was produced. All potentials in this work were applied inside the nanopipet relative to the outside

2.3.2 *Oil Droplet Emulsification and Detection.*

The emulsion was created from toluene (Fisher Scientific) and the ionic liquid trihexyltetradecylphosphonium bis(trifluoromethylsulfonyl)amide (IL-PA, 95%, Sigma-Aldrich) using a procedure modified from elsewhere.[21] Briefly, 56 μL of IL-PA was added to 200 μL of toluene and mixed to create a 400 mM IL-PA in toluene solution. This solution was added to 10 mL of 200 nm-filtered 5 mM TBACl in DI H_2O. This combined solution was vortexed for 20 s then immediately ultrasonicated at 10 W for 60 s by a QSonica XL-2000 probe sonicator. The resulting emulsion was milky white and was immediately diluted to the desired concentration in 200 nm-filtered 5 mM TBACl. The 5 mM TBACl aqueous solution outside of the nanopipet was replaced with the diluted emulsion solution in 5 mM TBACl with the entire setup shown in Figure 2.1a. For recording amperometry of emulsion droplets, the Dagan Chem-Clamp was interfaced to a Digidata 1440A digitizer (Molecular Devices) which was connected to a PC through USB. Amperometry was recorded using Axoscope 10.2 software with a sampling frequency of 50 kHz using a 10 kHz low-pass filter on the Dagan Chem-Clamp.

2.3.3 *Emulsion Characterization.*

Following amperometry, each emulsion solution was characterized with a NanoSight LM10 (Malvern) to measure the size distribution and ensure that it matched previous size data. After each emulsion-nanopore experiment, 1 mL of the outer solution volume from the beaker was injected into the NanoSight and analyzed in a 2 min recording to measure particle diffusion coefficients and radii. The zeta potential of emulsion droplets following emulsification in 5 mM

TBACl was found to be +35 mV as measured with a Zetasizer Nano (Malvern), suggesting that the TBA^+ ions partition into the toluene phase.

2.3.4 *Data Analysis.*

Prior to analysis, every 50 points of the current-time traces were averaged to increase the signal-to-raise ratio to resolve the few-pA current steps. Steps were analyzed using a script written in R that used a changepoint detection algorithm made available as a package. After changepoint detection, the results were compared with the raw data to ensure that changepoints were placed accurately. Python and its libraries Matplotlib, NumPy, and tiff files were used to construct videos displaying voltage, ionic current, and mean fluorescence counts along with recorded camera frames simultaneously.

2.3.5 *Simultaneous Optical and Electrical Recording.*

Electrical recordings were made with the same equipment outlined previously. The simultaneous optical recording was made with a Nikon Eclipe Ti microscope with a 60× objective. The excitation source was a Thorlabs M530L2 collimated LED powered by a DC2100 LED driver. The light was filtered with a Cy3 emission/excitation filter cube. The camera used was an Andor Clara capturing images from a binned 512 × 512 pixel area at a frequency of 6.57 Hz. The nanopipet was lowered with a screw micromanipulator into a well-formed by PDMS on a glass coverslip positioned above the objective. Emulsion preparation for optical imaging followed the same procedure as previously described except that 1 mM Nile Red (Aldrich) in toluene was used instead of pure toluene as the basis of the 400 mM IL-PA in the toluene mixture.

2.4 Results and Discussion

2.4.1 *Fabrication and Characterization of Pipet Nanopores.*

Quartz nanopipets were prepared by laser pulling using a commercial pipet puller with detailed parameters described in the Experimental Section. Prior to their use for collision and translocation of emulsion droplets, quartz pipet nanopores were characterized by cyclic voltammetry to measure their ionic resistance and estimate their pore size.[23] Relatively large pipet nanopores between 200 and 500 nm in diameters were selected to study droplets in the 100-200 nm range. Because nanopore radii are significantly greater than the Debye length (<3 nm in 5 mM tetrabutylammonium chloride (TBACl)), nanopores of this size range show a nearly linear, Ohmic i−V response as shown in Figure S 2.1. The ionic resistance of the nanopore was determined from the inverse slope of the i−V response, and the nanopore size was estimated using the following equation:[24]

$$R_p = \frac{1}{ka}\left(\frac{1}{\pi \tan\theta} + \frac{1}{4}\right) \qquad \text{Eq 2.1}$$

where R_p is the measured ionic resistance of the pore, κ is the solution conductivity, a is the pore radius at the orifice, and θ = 8.5° is the half-cone angle of the pipet pore. The solution conductivity κ was approximated as being equal to the conductivity of a 5 mM potassium chloride solution, or approximately 0.07 S·m.[25] Using Eq 2.1, the calculated pore radius is found to be within 10% of that measured by electron microscopy.

2.4.2 *Emulsion Droplet Detection.*

Collision and coalescence of individual emulsion droplets are observed when a small negative potential is applied from inside the pipet pore relative to the outside. Figure 2.1b is a 120 s current−time trace recorded at -0.3 V on a 200 nm diameter pipet pore in water containing 5 mM

TBACl and 2 nM, 160 nm diameter toluene emulsion droplets. Three representative collision and translocation events can be seen from this current−time trace. Despite their somewhat different and random durations, these events have similar shapes indicating stochastic single particle behavior at the nanopore orifice. Figure 2.1a is our proposed three-stage process to describe their current−time response. First, each translocation event starts from tens of smaller stepwise current decreases, usually less than 10 pA, starting from the baseline current of the open pore, i_{ss} (stage 1: 20−50 s). These small current steps correspond to collision and coalescence of individual small droplets onto a droplet already trapped at the pore orifice (Figure 2.1a). The trapped droplet grows in volume as new droplets collide and coalesce, leading to stepwise increased blockages of the nanopore current. This process continues until the overall nanopore current drops to 40%−70% of its initial value. It then quickly drops after one or two additional steps reaching a very low current level corresponding to ∼5% of the nanopore's open baseline current, indicating that the nanopore is now entirely blocked by the formation of a large droplet (Figure 2.1a). This very large current blockage lasts 2-5 s (stage 2) before it drastically increases back to the original baseline current. Here we define this fast current increase as stage 3, which has the shortest duration and the greatest current change (∼95% of the total current), indicating complete translocation of the trapped large droplet (Figure 2.1a). In the following section, we present simultaneous electric and optical recordings of this process to confirm this proposed mechanism and show that individual emulsion droplets indeed collide and coalesce at the nanopore orifice, resulting in nanopore blockage and translocation of a larger droplet.

Collisions of smaller emulsion droplets at the nanopore orifice and the subsequent translocation of a coalesced larger droplet across the nanopore are primarily driven by electroosmosis and electrophoresis. To understand this, it is necessary to examine the forces

governing a droplet's movement in solution far from and near the pore orifice. Near the nanopore, the electric field is highly concentrated, and electrophoresis and electroosmosis act on the droplet. Electrophoresis is the force directly acting on the oil droplet due to its surface charge. The zeta potential of these droplets has been measured as being −15.8 mV in a salt-less solution.[21] Although this is quite weak for an emulsion, the zeta potential is altered by the addition of 5 mM TBACl in our experiments. The TBA^+ ion partitions into the toluene droplet, giving the emulsion droplets a zeta potential of +35 mV as measured with a Zetasizer Nano. Under the negative potential applied inside relative to outside, the positively charged droplets are driven inward when they enter the concentrated electric field of the nanopore. The electroosmotic flow, on the other hand, is due to the movement of positive ions along the negatively charged inner wall of the quartz nanopore. A negative potential from inside to outside creates a flow that drives species toward and into the nanopore. Outside of the nanopore, the electric field approaches zero, and oil droplets move under the influence of Brownian motion and the electroosmotic flow. As determined from later optical recordings, the electroosmosis within the nanopore creates a flow that interacts with emulsion droplets up to at least 5 μm away from the nanopore orifice. This flow is attenuated as the coalesced droplet in the nanopore grows, and eventually, only droplets in the near vicinity of the nanopore are under its influence. Given that the droplet−nanopore electrical signals shown in Figure 2.1b occur only at negative potentials, that the emulsion droplets are positively charged, and that there is noticeable convection observed up to 5 μm away from the nanopore in the optical recordings, we conclude that both electroosmosis and electrophoresis act on emulsion droplets at the nanopore. On the basis of the assumption that the quartz nanopore is fully blocked in stage 2, we examine the residual ionic current that remains during the translocation of the coalesced oil droplet. The size of the particle relative to the nanopore and its elastic nature result in a reversible >95%

blockade of the nanopore's ionic current when the applied voltage is less than ~0.3 V, for which we have been unable to find precedent in the literature. Previous studies, notably by the White group, have demonstrated the trapping and translocation of soft particles. However, these translocation events rarely resulted in more than a 67% reduction of the nanopore's baseline current. Interestingly, there is a significant voltage dependence on the ionic current blockades of these large translocations as shown in Figure 2.2a. At -0.2 V there is a nearly 99% reduction in ionic current, and at -0.4 V the current blockade was reduced to 87%.

We believe that this remarkably large current blockage at lower applied voltages is due to the elastic nature of the coalesced oil droplet and its low electric conductivity. As illustrated in Figure 2.1a (middle), the large oil droplet may readily extend itself on both sides of the nanopore orifice requiring a significant amount of force to push through. At lower voltages, the few -pA residual current in stage 2 is likely caused by ion transport in an ultrathin aqueous volume present near the negatively charged hydrophilic quartz walls. Additionally, it has been hypothesized that the concentrated electric field of a nanopore can cause charged, elastic particles to deform and elongate along the axis of the pore, increasing the aqueous volume along the nanopore walls. This effect is more significant at higher applied voltages as evidenced from the increasing residual current in Figure 2.2a. Another contribution comes from the transport of tetrabutylammonium ions (TBA^+) through the water−toluene−water interface, further discussed in a later section. After reaching a threshold voltage (~0.2 V), the movement of TBA^+ through the toluene phase is enabled in the concentrated electric field of the nanopore. The fact that the percent current blockage levels off at voltages higher than 0.7 V may indicate that the residual current is dominated by the aqueous volume between the pore walls and the oil created by the oil deformation and that volume is reaching a steady state at higher voltages. The effect of the increased electric field is evident in the

translocation time, τ, of the coalesced oil droplets as shown in Figure 2.2b. At lower applied voltages, e.g., -0.2 V, a coalesced droplet can be trapped in the nanopore indefinitely, indicating a strong affinity between the oil droplet and the pipet pore. This duration drops to less than 10 s as the voltage is increased to -0.3 V and to ∼10 ms at -0.7 V. Interestingly, further increasing the applied voltage results in a slight increase in the translocation time, which may indicate that the voltage-driven deformation of the droplet may become more significant at these voltages and the effective driving force may be reduced by such deformation. The relationship between nanoparticle translocation time and applied potential in nanopores has been investigated previously. Davenport et al. investigated the role of pore geometry on nanoparticle translocation dynamics and found electroosmosis-driven transport to be effective at slowing the transport of highly charged nanoparticles through nanopores.[26] White and co-workers found that they could balance the forces acting on nanoparticles in nanopores through the application of a pressure difference in addition to electroosmosis and electrophoresis within a nanopore.[27]

2.4.3 *Emulsion Coalescence Dynamics.*

Examining the small current steps in stage 1 enables one to study interesting single-droplet collision and coalescence dynamics. We attribute these steps to the collision and incorporation of individual oil droplets into a trapped droplet at the sensing zone of the nanopore. Each addition of a droplet to the trapped droplet results in an increase in the size of the coalesced droplet which decreases the amount of ionic current able to flow through the nanopore. These droplet additions are observed as the stepwise reduction of ionic current in a current−time trace. Figure 2.3a displays the average step height, in percent of open-pore ionic current, plotted as a function of applied voltage for detection of 160 nm diameter emulsion droplets on three different pipet pores: 200, 300, and 375 nm in diameter. Depending on the pore size and the applied voltage, each emulsion

droplet causes a decrease in the ionic current that ranges from 0.3% to 1.2%. As a reference, it is predicted using numerical simulation[28] that one should expect a resistive pulse to blockade ~3% of the ionic current for a 160 nm diameter particle translocating through a 300 nm diameter nanopore. Furthermore, an inverse relationship is observed between step height and applied potential for all three pore sizes in Figure 2.3a. In typical resistive pulse measurements of solid nanoparticles, the fraction of volume excluded by the pore remains constant regardless of voltage, and as such, the fraction of ionic current blocked remains constant.[29] The smaller current decrease and its voltage dependence are likely due to the voltage-induced particle deformation increasing the ionic current in the aqueous phase around the coalesced droplet. To fully block a 300 nm diameter nanopore, one would expect that a droplet of 300 nm in diameter or larger is required. A calculation reveals that seven 160 nm diameter droplets are required to coalesce to form a 300 nm diameter spherical-shaped droplet. This number is lower than that of our experiments, which can be explained by the elastic nature of the coalesced droplet and its strong electrostatic affinity to the negatively charged quartz walls. The elastic nature of the oil particle allows the particle to be deformed easily, likely extending itself on the two sides of the nanopore orifice. The electrostatic interaction between the positively charged oil droplet and the negatively charged quartz walls further “pulls” the oil droplet onto the quartz walls. Therefore, it may require an oil particle with a much greater volume to fully block the pipet pore. It is reasonable to believe that the coalesced oil droplet takes a dumbbell shape when the pipet pore is fully blocked. This effect was noticed during fluorescence imaging mentioned later, where the addition of a droplet sometimes changed the position of the coalesced oil droplet in the nanopore.

The step frequency, or droplet collision frequency, plotted in Figure 2.3 shows a proportional relationship with increasing voltage for each pore studied. This follows other reports

in which an increased pressure differential across the nanopore increased the detection frequency.[27] In the case of our pores this pressure is replaced with an electroosmotic flow and electrophoretic force, the magnitude of which increases with voltage. This should increase the flux of droplets to the nanopore above that expected through a purely diffusional process. The diffusion coefficient of an 80 nm radius droplet can be estimated from the Stokes-Einstein equation[21]

$$D_d = \frac{k_b T}{6\pi\eta r_d} \qquad \text{Eq 2.2}$$

where k_b is the Boltzmann constant, T is the temperature, η is the viscosity of water at 298 K, and r_d is the radius of an individual droplet. Using Eq 2.2, the calculated diffusion coefficient of an 80 nm radius droplet is 3.1×10^{-8} cm^2 s^{-1}. We can then estimate the diffusional flux of droplets to the nanopore through the equation[21]

$$f_d = 4 D_d C_d r_e \qquad \text{Eq 2.3}$$

in which C_d is the droplet concentration and r_e is the nanopore radius. From our particle concentration of 2 nM, or 1.2×10^{12} particles/mL, and a 150 nm radius nanopore, our calculated collision frequency is 0.21 Hz. This value is below all measured collision frequencies in the presence of electroosmosis in our experiment, further confirming the important role of electroosmotic flow and electrophoresis in the collision and coalescence of droplet particles.

2.4.4 *The transition from a Steplike Current Response to a Peak-Shape Response.*

An interesting transition has been observed to the shape of the small collision responses of individual emulsion droplets when the applied voltage was increased. Figure 2.4 shows detection results of 2 nM 160 nm diameter emulsion droplets collected on a 200 nm diameter pipet pore at two different voltages. At -0.3 V, a steplike current response is observed for each particle collision event. At -0.7 V, the steplike response changes to a peak-shape current response where each

collision event results in a quick and large decrease in current followed by a slower increase. The exact reason for this shape change is unknown at this moment. However, we speculate that it is caused by differences in the kinetics of redistributing an additional oil droplet onto a trapped larger droplet. The idea is based on the assumption that the coalesced oil droplet extends on both the inside and the outside of the nanopore orifice, and the incoming smaller oil droplet is added first onto the outside portion of the trapped droplet. The trapped droplet flattens out on the quartz walls due to the electrostatic interaction, elasticity, and hydrodynamic pressure exerted onto the oil surface due to the electroosmotic flow. At lower holding potentials, the electroosmotic flow is relatively small. Therefore, the added volume (due to the incoming droplet) onto the outside portion of the trapped droplet can be easily redistributed into the inside volume, yielding a steady current response. At higher potentials, however, the electroosmotic flow is much stronger, causing a stronger hydrodynamic pressure onto the surface of the trapped droplet. Therefore, the newly added volume (due to an incoming droplet) may take a longer time to redistribute into the entire droplet. Because nanopore current is mostly sensitive to changes at the nanopore orifice, we believe the spikes reflect the time it takes for the added volume to redistribute.

2.4.5 *Droplet Trapping.*

When the applied voltages are lower than -0.3 V, the coalesced emulsion droplet can become trapped at the pipet pore for an extended duration. In this potential regime, the forces near the pore orifice are strong enough to attract droplets to the pore but not strong enough to pull the large trapped droplet through the orifice. In this case there are greater than 95% ionic current blockades that last hundreds of seconds or until perturbed by increasing the potential. Figure S 2.4 shows a typical trace for one of these droplet trapping events. This process is similar to lipid bilayer experiments where the formation of a bilayer is heralded by the sudden decrease of ionic current

as a gigaohm electrical seal is formed around the bilayer.[30] The seal around the droplet is similarly strong, around 10 GΩ at lower voltages. This is perhaps best thought of as a pair of resistors in parallel, where one resistor represents the continuous aqueous volume around the droplet and the other resistor represents the flow of ionic current through the toluene−water−toluene interfaces. As the resistance around the droplet in the continuous aqueous volume becomes too great, ion transfer across the interfaces becomes preferable. In this trapped state, we hypothesize that the electroosmotic pulling force is clamped off, reducing the individual droplet collision frequency close to its diffusion-only value as described earlier. This result is important for our subsequent study of voltage-driven ion transfer across a trapped droplet.

2.4.6 *Fluorescence Imaging.*

To verify our proposed mechanism, we conducted simultaneous electric recording and fluorescence imaging of the collision of individual emulsion droplets and translocation of coalesced large droplets across the pipet pore. A lipophilic dye, Nile Red, was chosen as it partitions heavily into the toluene phase while having minimal background fluorescence in the aqueous phase.[31] Applied voltage, ionic current, and fluorescence videos were measured and recorded simultaneously. Figure 2.5 shows a 30 s current-time trace of a 400 nm diameter nanopore at -0.4 V in an aqueous solution with 5 mM TBACl containing 2 nM 160 nm diameter emulsion droplets with 1 mM Nile red dye. A coalesced emulsion droplet was initially trapped at -0.2 V in the nanopore from the beginning of the current recording, which blocks nearly the entire current. The voltage was quickly increased to -0.4 V at t = ∼4 s, resulting in an increase in the nanopore current to ∼-800 pA. A fluorescence image (top inset of Figure 2.5) was recorded at the red mark on the current-time trace showing the presence of a trapped droplet at the pore orifice. The increased voltage eventually pulls the trapped droplet through the nanopore at t = ∼6 s, resulting

in a sudden increase in the nanopore current to its open pore value of -2200 pA. The translocation was followed by small stepwise increases indicating the beginning of a subsequent collision and coalescence process. A second fluorescence image captured after the translocation event shows that a large coalesced droplet has been displaced from the pore orifice, with a new droplet forming.

After confirming the presence of the trapped oil droplet and its translocation across the nanopore, we now seek to demonstrate the ability to record the collision and coalescence processes of small individual emulsion droplets with fluorescence and electric recordings. Figure 2.6 shows a 75 s portion of the correlated current and fluorescence recordings on the same nanopore as used in Figure 2.5 focusing on the small current steps at the beginning of the coalescence process. Figure 2.6a shows the discrete changes in nanopore current as individual oil droplets collide onto the coalesced and trapped larger droplets. Figure 2.6b shows discrete increases in the fluorescence signal at the nanopore orifice which correlate well in time with current steps through the nanopore. Therefore, results in Figure 2.6 unambiguously proved our hypothesis about the collision and coalescence of individual emulsion droplets at the nanopore orifice.

Careful examination of the fluorescence and electrochemical recordings has revealed several interesting observations. First, it is confirmed that particle collision is indeed driven by electroosmotic flow. The electroosmotic flow during this period is visibly strong as evidenced by the convection of droplets within the entire field of view of the camera. This stage is seen in the few seconds at the beginning of droplet formation or immediately after the translocation of a droplet that previously occupied the orifice. As the droplet grows, the ionic current drops and the apparent electroosmotic flow decreases as can be seen in the reduction of motion of oil droplets. At this point, the droplets appear to exhibit Brownian motion except in the very near vicinity ($\sim$1 μm) of the nanopore orifice. If a droplet diffuses too closely to the pore, it is pulled into the pore

and will either join the already-formed coalesced droplet or be accelerated past the pore back into solution where it returns to Brownian motion. Second, as the oil droplet at the pore orifice grows, it can suddenly be nudged into the fully trapped state through the collision of a droplet in solution. This is seen through the correlation of a >90% ionic current blockade with a sudden increase in fluorescence, along with the apparent collision of a droplet with the trapped droplet at the nanopore orifice. As with the purely electrical measurements, the droplet can remain in the trapped state for minutes at a time or until perturbed. The introduction of a perturbation force through a potential increase causes a stronger pulling force to the coalesced and trapped droplet. This droplet movement is accompanied by a gradual weakening of the electrical seal at the pore and an increase in ionic current. The droplet is then suddenly released from its trapped state, causing a rush of droplet solution to be drawn into the pore and quick initial growth of a new oil droplet. The sudden movement of the droplet occurs simultaneously with the decrease of mean fluorescence at the nanopore orifice and an increase in ionic current. Third, there is a remarkable agreement between video and step collision analysis. As mentioned in a previous section, the droplet collision frequency at the nanopore orifice determined from current steps is higher than that estimated based on diffusion, and this is made apparent by the fluorescent imaging. The electroosmotic flow into the pore gets attenuated as the trapped droplet in the orifice grows larger over the course of an experiment. The rapid flux of droplets to the orifice immediately after a translocation demonstrates the influence of the electroosmotic flow. As the trapped droplet grows, the force pulling droplets into the pore weakens and only an area near the orifice attracts droplets, although this still creates a collision frequency above that expected through pure diffusion.

2.4.7 *Observing Ion Transfer across a Trapped Droplet.*

The strong trapping affinity at the pore orifice allows us to study ion transfer across two water/oil interfaces formed across a trapped oil droplet. A similar setup has been recently reported by Dryfe and co-workers,[32] in which they studied ion transfer across a supported liquid membrane separating two aqueous solutions using cyclic voltammetry and spectrophotometry. Their study used hydrophobic microporous poly(vinylidene fluoride) (PVDF) membrane filters (0.45 μm pore size, 125 μm thickness, 75% porosity) which also define the thickness of the supported liquid membrane. The use of a unique pipet nanopore in our work has enabled us to examine ion transfer across a single coalesced oil droplet of only a few hundred nanometers in size. It is important to note that the measured current−voltage signal can be affected by three different types of processes: the transfer of ions across the water/oil interface, the transfer of ions in the tight space between the quartz walls and the surface of the trapped oil droplet, and the transport of ions in and out of the water/oil interface (double-layer charging). The leakage current is quite small, on the order of a few to tens of pA depending on the applied voltage, as shown in Figure 2.1 as well as in Figure S 2.3 and Figure S 2.4. It shows as a linear, Ohmic response. The double-layer charging current shows up as the hysteresis between the forward and backward scan in the current−voltage curve. The ion-transfer current across the oil/ water interface, on the other hand, should happen only when the applied voltage is greater than the minimum voltage required to transfer charges.

Consecutive cyclic voltammetry was performed at 20 V/s on a droplet trapped at a 300 nm diameter nanopore with a -100 mV initial holding potential. The post-CV current returns to its initial value prior to CV scan, indicating that the gigaohm seal was kept during the scan. Figure 2.7a is a cartoon illustrating the three phases present in the system: the aqueous phase inside the pipet, A, the trapped toluene phase at the pore orifice, T, and the bulk aqueous phase in the external

solution, B. The initial concentration of TBACl in the aqueous phase was 5 mM with none present in the toluene phase. However, it is expected that the concentration of TBA^+ in the trapped toluene phase T to be nonzero due to partitioning.[33] Figure 2.7b shows a typical current−voltage response when the potential was scanned from -0.1 to +0.65 V, to -0.6 V, then back to the initial -0.1 V. A significant charging current was observed due to the relatively high scan rate. On top of the charging current, there are three pairs of voltammetric peaks with formal potentials of -0.28, 0, and 0.25 V, respectively. The two pairs of peaks on the anodic and cathodic sides of the current−voltage curve are believed to be associated with voltage-driven ion transfer processes as marked in Figure 2.7b. It is worth noting that these values agree with values reported by Dryfe and co-workers.[32] The transfer of TBA^+ from the toluene to the aqueous phase is believed to be associated with the waves at +0.15 and -0.2 V. The low potentials for this transfer when compared with the outer peaks are due to TBA^+ being better solvated in the aqueous phase than the organic phase. The middle pair of peaks at around 0 V is believed to be associated with ion transport in the ultrathin volume of aqueous solution between the oil and the quartz walls. As the potential polarity across the oil droplet was rapidly changed at 0 V, the trapped oil droplet likely undergoes a quick shape deformation which momentarily changes (increases) the ionic conductivity, leading to a current increase. The shape of the trapped droplet may quickly return to its initial shape as the potential was further scanned, resulting in a slight current decay. This initial result has demonstrated our unique ability to study ion transfer processes across a nanometer-sized oil droplet trapped at the nanopore orifice.

2.5 CONCLUSIONS

We have used the highly sensitive and fast resistive-pulse technique and fluorescence microscopy to study the collision and coalescence of individual oil droplets at the orifice of a

conical quartz nanopipet. The collision of an attoliter oil droplet onto a droplet trapped at the nanopore orifice leads to a measurable change in the nanopore's ionic conductance. Accumulation of tens of oil droplets causes a complete blockage of the nanopore by the coalesced droplet, which can stay in its fully trapped status for hundreds of seconds when a lower voltage is applied across the nanopore. On the other hand, a trapped oil droplet can be forced to translocate within several milliseconds at higher voltages. The trapped attoliter droplet can be individually and repeatedly studied with cyclic voltammetry to investigate ion transfer processes across a small nanometer-sized droplet. The entire phenomenon is examined optically using fluorescent microscopy with a lipophilic dye to confirm the hypothesis of particle collision and coalescence. To the best of our knowledge, this is the first time a solid-state nanopore is used to study collision, coalescence, and translocation of individual oil droplets and ion transfer across a nanopore-supported nanodroplet. Nile red, as a solvatochromic dye, facilitates the detection at the oil/water interface. We believe that due to Nile red's unique properties, it can be used probe the hydrophobicity of an interfaces, which is presented in Chapter 3.

2.6 FIGURES

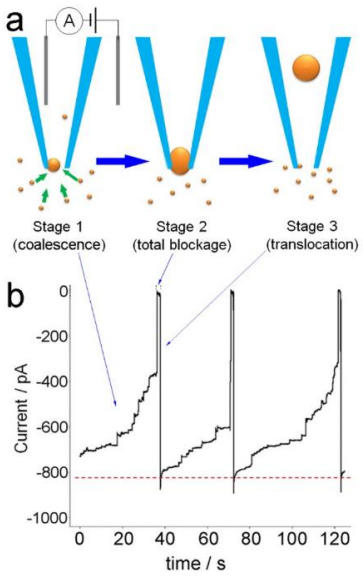

Figure 2.1. Scheme of the translocation of oil emulsions and corresponding current response

(a) Cartoon showing collision and coalescence of individual emulsion droplets at a pipet orifice and the subsequent droplet translocation. A small voltage (<1 V) is used to drive the flow of small emulsion droplets toward the pore and the ionic current is monitored. (b) Three droplet translocation events on a 200 nm diameter pipet pore in water containing 5 mM TBACl and 2 nM 160 nm diameter toluene droplets under a −0.3 V bias. Each translocation event starts from multiple smaller stepwise current decreases starting from the open pore's baseline current at ∼−820 pA (stage 1: 20−50 s in duration) followed by a quick and large current decay blocking >95% of the total current (stage 2: 2−5 s in duration). The nanopore current is seen to increase drastically back to the original baseline indicating translocation of a trapped oil droplet (stage 3: <5 ms). The small current steps (few pA) in stage 1 indicate collision and coalescence of small droplets onto a trapped oil droplet at the pore orifice. The large current decay at the end of stage 1 is due to growth of the trapped droplet exceeding a certain size limit causing a complete blockage of the pipet pore. Stage 3 has the shortest duration and the greatest current change (>95% in this case) indicating translocation of the trapped large droplet through the pore. The red dashed line in (b) marks the ionic current baseline as determined from a CV prior to droplet studies.

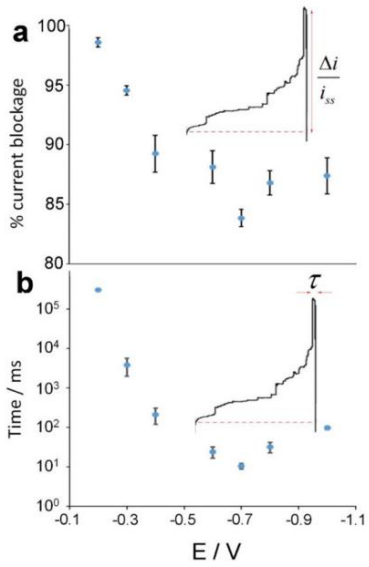

Figure 2.2 Current blockage and time caused by a coalesced droplet

(a) Plot of the percent current blockage caused by a coalesced droplet on a 200 nm diameter pipet pore as a function of the applied potential. (b) Plot of the residence time, τ, of a coalesced droplet as a function of the applied potential. Error bars are standard error.

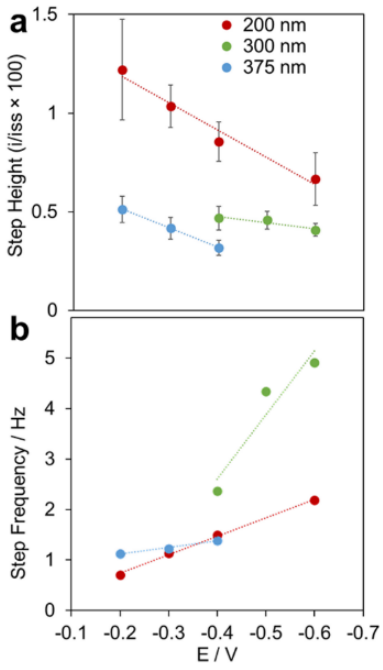

Figure 2.3 Step height and step frequency of a single oil droplet

(a) Average percent current reduction due to the addition of a single oil droplet plotted as a function of the applied potential for three different nanopores with diameters listed in the legend. The steps follow a trend of being higher for smaller pores as seen in the −0.4 V points. The steps become smaller with increased potential which is attributed to a larger ionic leakage current around and through the coalesced droplet. Error bars are standard error. (b) Frequency of current steps as a function of applied potential. Unlike step height there is no obvious trend among different pore sizes. However, steps (droplet collisions) become more frequent with applied potential among all pores studied.

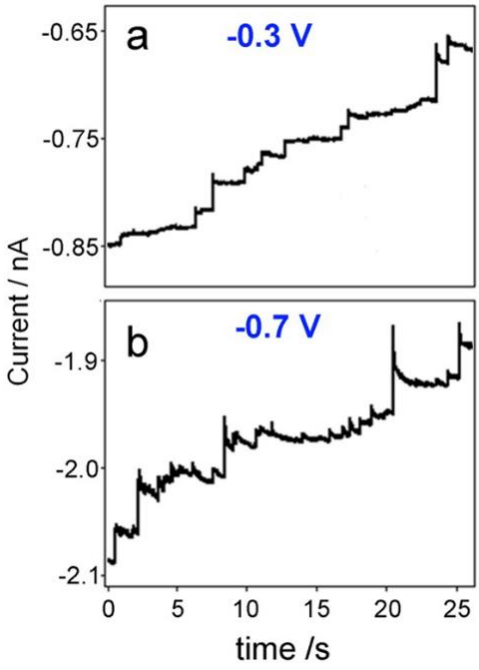

Figure 2.4 Comparison of steplike current changes observed at −0.3 V

(a) and peak-shape current changes at −0.7 V (b). A 200 nm diameter pipet nanopore was used to detect 160 nm diameter emulsion droplets. Single droplet collision and coalescence change from step-shape responses to peak-shape responses as the applied voltage was increased.

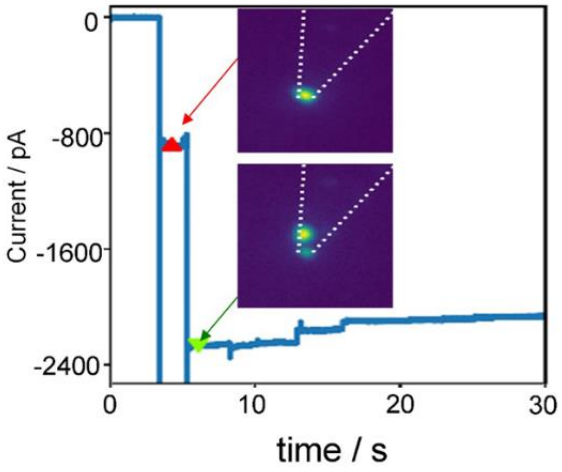

Figure 2.5 Fluorescence images and current response for the translocation of an oil droplet

Fluorescence images corresponding to points on the ionic current−time trace before (red triangle) and after (green triangle) the translocation of a coalesced oil droplet through the nanopore. The white dashed lines in the images denote the edges of the nanopipet. The bright dot in the upper image is the coalesced oil droplet with fluorescently excited Nile Red. In the lower image, the trapped droplet has moved further up into the nanopipet but is still adsorbed to the wall. At this stage, because of residue from the previous droplet or the immediate collision of new individual droplets, a new oil droplet is forming in the nanopore orifice.

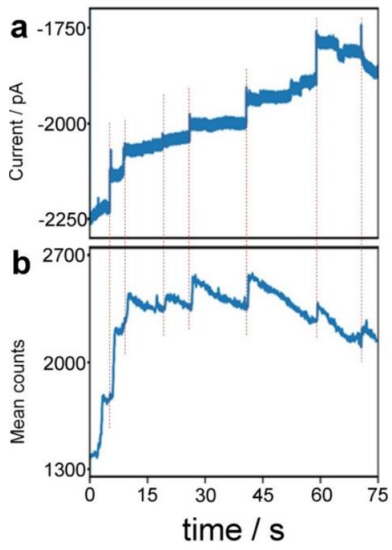

Figure 2.6 Current response and fluorescence trace for the translocation of an oil droplet

(a) Ionic current versus time for a nanopore during oil droplet collisions. (b) The corresponding fluorescence trace recorded simultaneously. Counts were measured as the mean fluorescence of a square region of pixels at the nanopore orifice.

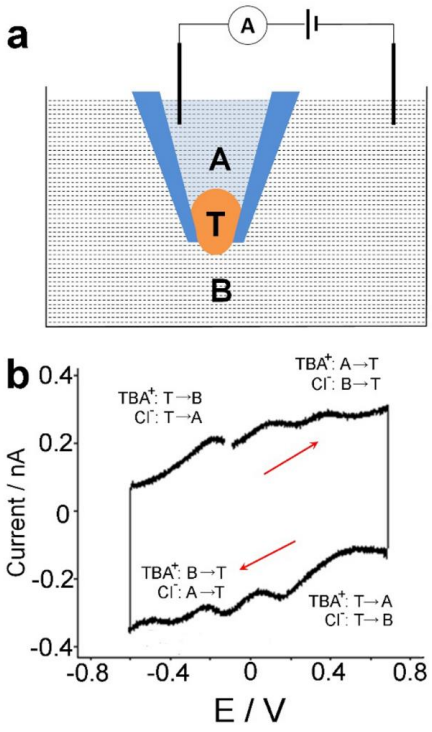

Figure 2.7 Illustration of oil emulsion and proposed ion movements

(a) Illustration of three phases present during CVs of fully trapped emulsion droplets with the aqueous nanopipet phase A, the toluene droplet phase T, and the outer beaker solution B. (b) CV at 20 V/s of a trapped droplet on a 200 nm diameter pore with proposed movement of TBA^+ and Cl^- ions. The red arrows in (b) indicate the direction of potential scan. Potential listed is the voltage applied to the inside of the nanopipette relative to the outside.

2.7 SUPPORTING INFORMATION

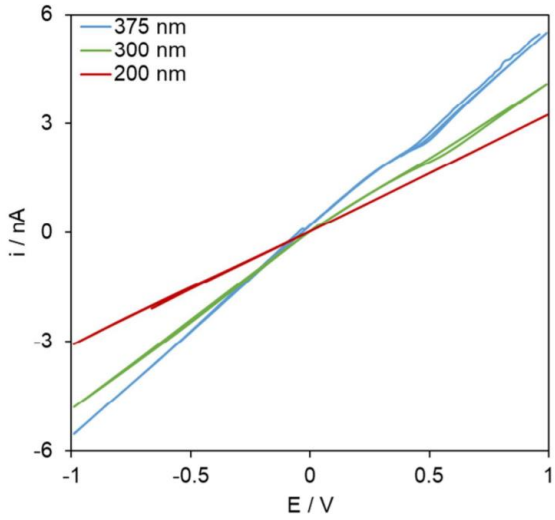

Figure S 2.1 i-V curves in 5 mM TBACl at 100 mV/s for the three pipette nanopores.

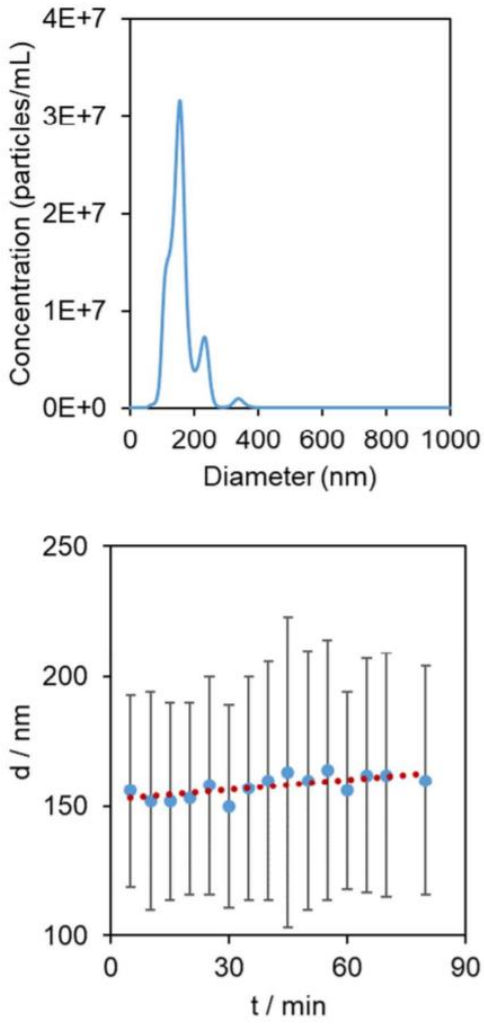

Figure S 2.2 Size distribution of emulsions and the stability of emulsion size

(Top) Typical size distribution of emulsion droplets in 5 mM TBACl following the emulsification procedure in the main text. (Bottom) An emulsion stability study showing the mean droplet diameter over time from 10 minutes to 80 minutes after emulsification. Error bars are +/- one standard error of the mean. The red dotted line is a line of best fit to the means.

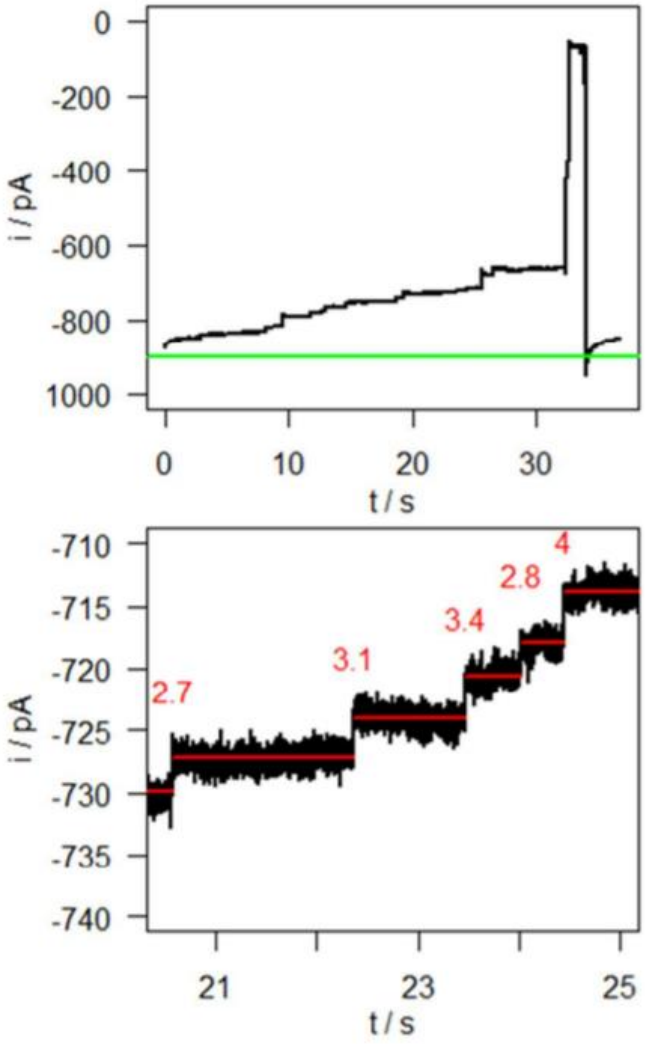

Figure S 2.3 A typical trace of droplet collision, coalescence, and eventual translocation through a nanopore

(Top) A typical trace of droplet collision, coalescence, and eventual translocation through a nanopore at -300 mV. The green line is the ionic current baseline as determined from a CV prior to droplet studies. The collision and coalescence of individual emulsion droplets in solution is seen at the nanopore orifice through few-pA steps leading up to a larger translocation event that blocks >90% of the ionic current. (Bottom) A zoom-in of part of the top trace showing individual steps with the step height in red numbering in pA.

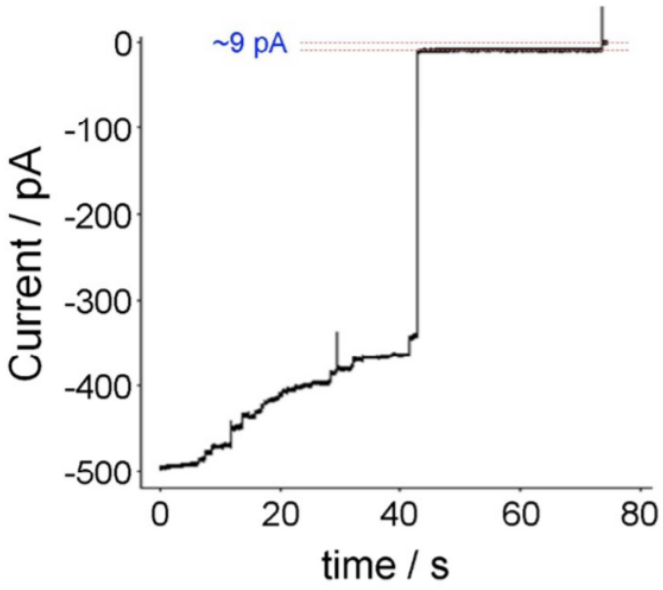

Figure S 2.4 Stepwise current trace

A 200-nm-diameter nanopore at -0.2 V featuring the stepwise decrease of ionic current before experiencing an indefinite 98.6% ionic current blockade. Typically, the droplets are stable enough in this trapped configuration to run cyclic voltammetry (CV)s at high scan rates (~20 V/s). At the 75 s mark, the potential is switched from -0.2 V to 0 V giving a large charging spike. This was done to demonstrate the magnitude of the blocked ionic current. In this case there was a 9 pA difference between the trapped state at -0.2 V and the off state at 0 V. With a 600 pA baseline at -0.2 V, as determined by the prior i-V curve, this amounts to a 98.6% ionic current blockade, or a 20 giga-ohm seal. The trapped droplet can be dislodged by increasing the magnitude of the negative potential or by switching to a positive potential to eject the droplet.

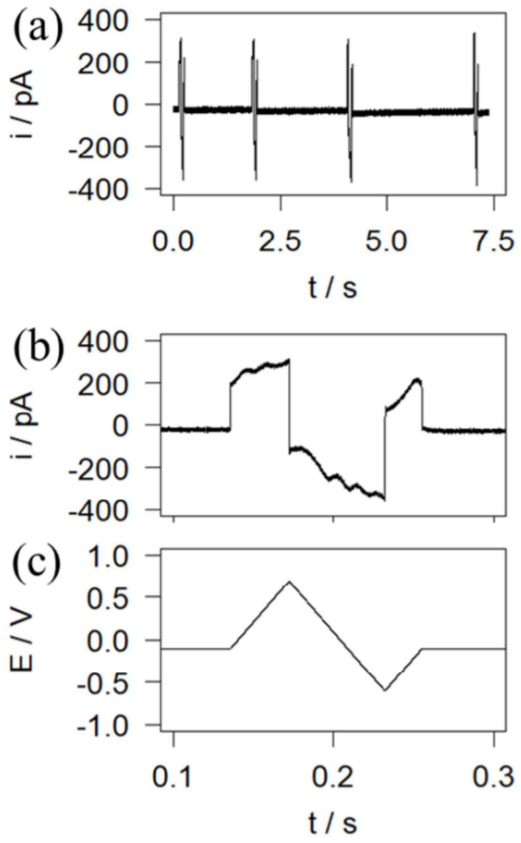

Figure S 2.5 Cyclic voltammetry of a trapped droplet

(a) 20 V/s cyclic voltammetry on a droplet being trapped with a -100 mV constant potential. The flat baseline following each CV indicates the droplet remains trapped following each CV. If the CV is too slow (5 V/s or less) the droplet will become unstable and the baseline will increase to a higher, open-pore current. (b) Zoom-in of the first CV in (a). (c) The waveform used to obtain the CV in (b).

2.8 REFERENCES

(1) Shi, W.; Friedman, A. K.; Baker, L. A. Nanopore Sensing. *Anal. Chem.* **2017**, *89*, 157–188.

(2) Li, G. X.; Zhang, Z. X.; Lin, X. Q. Fabrication of Glass Nanopore Electrodes for Single-Molecule Detection of β-Cyclodextrin. *Fenxi Huaxue/ Chinese J. Anal. Chem.* **2010**, *38*, 1698–1702.

(3) Heins, E. A.; Siwy, Z. S.; Baker, L. A.; Martin, C. R. Detecting Single Porphyrin Molecules in a Conically Shaped Synthetic Nanopore. *Nano Lett.* **2005**, *5*, 1824–1829.

(4) Harms, Z. D.; Mogensen, K. B.; Nunes, P. S.; Zhou, K.; Hildenbrand, B. W.; Mitra, I.; Tan, Z.; Zlotnick, A.; Kutter, J. P.; Jacobson, S. C. Nanofluidic Devices with Two Pores in Series for Resistive-Pulse Sensing of Single Virus Capsids. *Anal. Chem.* **2011**, *83*, 9573–9578.

(5) Zhou, K.; Li, L.; Tan, Z.; Zlotnick, A.; Jacobson, S. C. Characterization of Hepatitis B Virus Capsids by Resistive-Pulse Sensing. *J. Am. Chem. Soc.* **2011**, *133*, 1618–1621.

(6) Manrao, E. A.; Derrington, I. M.; Laszlo, A. H.; Langford, K. W.; Hopper, M. K.; Gillgren, N.; Pavlenok, M.; Niederweis, M.; Gundlach, J. H. Reading DNA at Single-Nucleotide Resolution with a Mutant MspA Nanopore and Phi29 DNA Polymerase. *Nat. Biotechnol.* **2012**, *30*, 349–353.

(7) Perera, R. T.; Fleming, A. M.; Johnson, R. P.; Burrows, C. J.; White, H. S. Detection of Benzo[a]Pyrene-Guanine Adducts in Single-Stranded DNA Using the α-Hemolysin Nanopore. *Nanotechnology* **2015**, *26*.

(8) An, N.; Fleming, A. M.; White, H. S.; Burrows, C. J. Nanopore Detection of 8-Oxoguanine in the Human Telomere Repeat Sequence. *ACS Nano* **2015**, *9*, 4296–4307.

(9) Ayub, M.; Bayley, H. Individual RNA Base Recognition in Immobilized Oligonucleotides Using a Protein Nanopore. *Nano Lett.* **2012**, *12*, 5637–5643.

(10) Ito, T.; Sun, L.; Crooks, R. M. Simultaneous Determination of the Size and Surface Charge of Individual Nanoparticles Using a Carbon Nanotube-Based Coulter Counter. *Anal. Chem.* **2003**, *75*, 2399–2406.

(11) Coulter, W. H. Means for Counting Particles Suspended in a Fluid. US Patent, 2656508. *United States Pat. Off. Patentiert am* **1953**, *20*, 1953.

(12) Pevarnik, M.; Healy, K.; Toimil-Molares, M. E.; Morrison, A.; Létant, S. E.; Siwy, Z. S. Polystyrene Particles Reveal Pore Substructure as They Translocate. *ACS Nano* **2012**, *6*, 7295–7302.

(13) Holden, D. A.; Watkins, J. J.; White, H. S. Resistive-Pulse Detection of Multilamellar Liposomes. *Langmuir* **2012**, *28*, 7572–7577.

(14) Chen, L.; He, H.; Jin, Y. Counting and Dynamic Studies of the Small Unilamellar Phospholipid Vesicle Translocation with Single Conical Glass Nanopores. *Anal. Chem.* **2015**, *87*, 522–529.

(15) Darvish, A.; Goyal, G.; Aneja, R.; Sundaram, R. V. K.; Lee, K.; Ahn, C. W.; Kim, K. B.; Vlahovska, P. M.; Kim, M. J. Nanoparticle Mechanics: Deformation Detection: Via Nanopore Resistive Pulse Sensing. *Nanoscale* **2016**, *8*, 14420–14431.

(16) Goyal, G.; Darvish, A.; Kim, M. J. Use of Solid-State Nanopores for Sensing Co-Translocational Deformation of Nano-Liposomes. *Analyst* **2015**, *140*, 4865–4873.

(17) Holden, D. A.; Hendrickson, G.; Lyon, L. A.; White, H. S. Resistive Pulse Analysis of Microgel Deformation during Nanopore Translocation. *J. Phys. Chem. C* **2011**, *115*, 2999–3004.

(18) Izquierdo, P.; Esquena, J.; Tadros, T. F.; Dederen, C.; Garcia, M. J.; Azemar, N.; Solans, C. Formation and Stability of Nano-Emulsions Prepared Using the Phase Inversion Temperature Method. *Langmuir* **2002**, *18*, 26–30.

(19) Somerville, J. A.; Willmott, G. R.; Eldridge, J.; Griffiths, M.; McGrath, K. M. Size and Charge Characterisation of a Submicrometre Oil-in-Water Emulsion Using Resistive Pulse Sensing with Tunable Pores. *J. Colloid Interface Sci.* **2013**, *394*, 243–251.

(20) Beverages, T. M.; Makhoul-mansour, M. M.; Eric, C. Emulsions : Basic Principles. **1999**.

(21) Kim, B. K.; Boika, A.; Kim, J.; Dick, J. E.; Bard, A. J. Characterizing Emulsions by Observation of Single Droplet Collisions - Attoliter Electrochemical Reactors. *J. Am. Chem. Soc.* **2014**, *136*, 4849–4852.

(22) Edwards, M. A.; German, S. R.; Dick, J. E.; Bard, A. J.; White, H. S. High-Speed Multipass Coulter Counter with Ultrahigh Resolution. *ACS Nano* **2015**, *9*, 12274–12282.

(23) Perry, D.; Momotenko, D.; Lazenby, R. A.; Kang, M.; Unwin, P. R. Characterization of Nanopipettes. *Anal. Chem.* **2016**, *88*, 5523–5530.

(24) Zhang, B.; Galusha, J.; Shiozawa, P. G.; Wang, G.; Bergren, A. J.; Jones, R. M.; White, R. J.; Ervin, E. N.; Cauley, C. C.; White, H. S. Bench-Top Method for Fabricating Glass-Sealed Nanodisk Electrodes, Glass Nanopore Electrodes, and Glass Nanopore Membranes of Controlled Size. *Anal. Chem.* **2007**, *79*, 4778–4787.

(25) Wu, Y. C.; Koch, W. F.; Pratt, K. W. Proposed New Electrolytic Conductivity Primary Standards for KCl Solutions. *J. Res. Natl. Inst. Stand. Technol.* **1991**, *96*, 191.

(26) Davenport, M.; Healy, K.; Pevarnik, M.; Teslich, N.; Cabrini, S.; Morrison, A. P.; Siwy, Z. S.; Létant, S. E. The Role of Pore Geometry in Single Nanoparticle Detection. *ACS Nano* **2012**, *6*, 8366–8380.

(27) German, S. R.; Luo, L.; White, H. S.; Mega, T. L. Controlling Nanoparticle Dynamics in Conical Nanopores. *J. Phys. Chem. C* **2013**, *117*, 703–711.

(28) Lan, W. J.; Holden, D. A.; Zhang, B.; White, H. S. Nanoparticle Transport in Conical-Shaped Nanopores. *Anal. Chem.* **2011**, *83*, 3840–3847.

(29) Luo, L.; German, S. R.; Lan, W. J.; Holden, D. A.; Mega, T. L.; White, H. S. Resistive-Pulse Analysis of Nanoparticles. *Annu. Rev. Anal. Chem.* **2014**, *7*, 513–535.

(30) Jonas, E. A.; Knox, R. J.; Kaczmarek, L. K. Giga-Ohm Seals on Intracellular Membranes: A Technique for Studying Intracellular Ion Channels in Intact Cells. *Neuron* **1997**, *19*, 7–13.

(31) Batchelor-McAuley, C.; Little, C. A.; Sokolov, S. V.; Katelh ön, E.; Zampardi, G.; Compton, R. G. Fluorescence Monitored Voltammetry of Single Attoliter Droplets. *Anal. Chem.* **2016**, *88*, 11213–11221.

(32) Velický, M.; Tam, K. Y.; Dryfe, R. A. W. Mechanism of Ion Transfer in Supported Liquid Membrane Systems: Electrochemical Control over Membrane Distribution. *Anal. Chem.* **2014**, *86*, 435–442.

(33) Deng, H.; Dick, J. E.; Kummer, S.; Kragl, U.; Strauss, S. H.; Bard, A. J. Probing Ion Transfer across Liquid-Liquid Interfaces by Monitoring Collisions of Single Femtoliter Oil Droplets on Ultramicroelectrodes. *Anal. Chem.* **2016**, *88*, 7754–7761.

Chapter 3. INVESTIGATION ON THE PHYSICAL PROPERTIES OF NANOBUBBLE USING SOLVATOCHROMIC NILE RED AND RHODAMINE 6G[2]

3.1 ABSTRACT

Firstly, we report the use of a polarity-sensitive and solvatochromic fluorophore Nile red to label and probe individual hydrogen nanobubbles on the surface of an ITO electrode. Nanobubbles are generated from the reduction of water on ITO and fluorescently imaged from the transient adsorption and desorption process of single Nile red molecules at the nanobubble surface. The ability to label and fluorescently image individual nanobubbles with Nile red suggests that the gas/solution interface is hydrophobic in nature. Compared to the short labeling events using Rhodamine fluorophores, Nile red labeled events appear to be longer in duration suggesting Nile red has a higher affinity to the bubble surface. The stronger fluorophore-bubble interaction also leads to certain nanobubbles being co-labeled by multiple Nile red molecules resulting in the observation of super-bright and long-lasting labeling events. Based on these interesting observations, we hypothesize that Nile red molecules may start clustering and form some kind of molecular aggregates when they are co-adsorbed on the same nanobubbles' surface. The ability to observe super-bright and long-lasting multi-fluorophore labeling events also allows us to verify the high stability and long lifetime of electrochemically generated surface nanobubbles. We then further study the long-lived property of nanobubbles by using rhodamine 6G (R6G) and find that

[2] Portions of this chapter are adapted with permission from: Zhuoyu P.; and Bo, Z; "Nanobubble Labeling and Imaging with a Solvatochromic Fluorophore Nile Red" *Anal. Chem*. 2021, 93, 15315−15322. Copyright (2021) American Chemical Society.

bubbles still can be detected for 15 mins without gas supplied! Moreover, we attempt to estimate the total number of nanobubbles generated at the electrode surface by the K-means algorithm.

3.2 INTRODUCTION

Surface nanobubbles are nanometer-sized gaseous pockets residing at the interface between a liquid medium (e.g, water) and a solid substrate. The presence of stable surface nanobubbles was first revealed by Lou et al. in 2000 using atomic force microscopy (AFM).[1] Surface nanobubbles are of special interest due in part to their extraordinary stability reported on different substrates, for example, highly oriented pyrolytic graphite (HOPG) substrates[2,3] and ultraflat gold surfaces.[4] The existence of stable surface nanobubbles and their remarkable longevity is not fully understood because theoretical calculations often predict nanobubbles of such dimension dissolve on a microsecond timescale due to the fast gas dissolution into the surrounding aqueous phase, driven by high Laplace pressures.[5,6,7] Apart from fundamental interest, surface nanobubbles and nanobubbles, in general, are essential in several key technological applications, including surface cleaning,[8,9] froth floatation,[10,11] nanomaterial engineering,[12] medical imaging,[13,14] catalysis[15,16], and electrolysis[17].

Two major methods have been widely used to generate surface nanobubbles, which include solvent exchange[1] and electrochemical generation[18]. The method of solvent exchange relies on the difference in gas solubility in two miscible solvents, such as ethanol and water. Bubbles are readily formed when one solvent (e.g, ethanol) in which the gas is more soluble is replaced by the other (e.g, water). With electrochemistry, on the other hand, bubbles are generated due to the chemical formation of gas molecules on the electrode surface. Bubble nucleation takes place when gas molecules reach their saturation point. In water electrolysis, for example, H_2/O_2 gases are formed by the hydrogen evolution reaction (HER) and the oxygen evolution reaction (OER) at the cathode

and anode, respectively. Due to the low solubility and slow diffusion of gas molecules, a super-saturation state can be reached when gas molecules are continuously generated at the electrode surface which is favorable for surface nanobubble formation.[19,20] The formation of gas bubbles at the solution/electrode interface can negatively impact the electrochemical reaction by blocking the electroactive surface area and reducing the overall reaction kinetics.[21] A more comprehensive understanding of the mechanisms and various factors that influence the formation, dissolution, and behavior of electrochemically generated gas bubbles is therefore of great fundamental importance.

In the past decades, surface nanobubbles have been extensively studied toward understanding their nucleation, growth, and stabilization.[22] Several imaging techniques have been well established for studying nanobubbles, including atomic force microscopy (AFM),[1,23] infrared spectroscopy,[7] transmission electron microscopy,[24] surface-plasmon resonance (SPR) imaging,[25] and fluorescence[26,27] and dark-field microscopies.[15] Besides these imaging methods, nanobubbles can also be formed and studied in-situ by monitoring the faradaic signal on a metal nanoelectrode.[28] Our group and others have been interested in the use of super-resolution fluorescence microscopy to study the electrochemical interface because it allows one to monitor certain dynamic redox processes in real time with high spatial and temporal resolution.[29,30] Toward this goal, we have reported a single-molecule fluorescence labeling approach to image H_2 and O_2 nanobubbles formed in water electrolysis using total-internal reflection fluorescence (TIRF) microscopy.[31,32] Our results show that H_2 and O_2 nanobubbles can be imaged by detecting the transient adsorption and desorption processes of single fluorophores (such as Rhodamine 6G or R6G) at the nanobubble surface. Additionally, our results suggest that these nanobubbles may form on the electrode at potentials well before an apparent faradaic current can be detected further confirming the high sensitivity of single-molecule fluorescence labeling.

Despite the fundamental importance of surface nanobubbles, our knowledge is quite limited about the chemical nature of the nanobubble surface. This is largely due to the enormous challenges in directly studying the nanobubble's gas/solution interface. The gas/liquid interface has often been studied with the help of surfactants. Ducker used tapping mode AFM to show that bubbles are stabilized by a thin layer of surface contaminants (e.g., surfactants).[33] Our group further demonstrated that the accumulation of surfactants at the bubble surface affects the structure of the gas/liquid interface (charge, hydrophobicity, etc.) from different fluorophore adsorption behaviors via TIRF measurement.[34] George et al. stated that when surfactant is enriched at the air-water interface, the polar head group favors the aqueous phase while the nonpolar tail prefers to be in the gas phase.[35] However, there has been a lack of direct studies on exploring other properties of the gas/liquid interface (e.g., hydrophobicity).

In this work, we use Nile red as a solvatochromic fluorophore to label H_2 nanobubbles on an electrode surface. We wish to probe the gas/water interface at the nanobubble surface due to the unique fluorescence behavior of Nile red in response to the local immediate environment.[36,37] Nile red can be nearly non-fluorescent in water and highly fluorescent in an organic solvent, such as acetone. By employing a polarity sensitive fluorophore, we aim to probe and further understand the hydrophobicity of nanobubble surface and study the adsorption behavior of fluorophores in a greater detail. The ability to fluorescently label and image nanobubbles using Nile red suggests that the surface of H_2 nanobubble is hydrophobic. Compared to the short labeling events using Rhodamine fluorophores, Nile red labeled events are significantly longer in duration suggesting Nile red has a higher affinity on the bubble surface. This stronger fluorophore-bubble interaction also causes nanobubbles to be co-labeled by multiple Nile red molecules leading to the observation of super-bright and long-lasting labeling events. Based on these interesting observations, we

hypothesize that Nile red molecules may start clustering and form molecular aggregates at the nanobubble surface. The ability to observe super-bright and long-lasting multi-fluorophore labeling events also allows us to verify the high stability and long lifetime of electrochemically generated surface nanobubbles. To further verify the long-term stability of surface nanobubbles, we use R6G instead of Nile red to label all possible bubbles to see how long and how many bubbles can still be detected after potential removal. Then the total number of nanobubbles are also estimated using the K-means algorithm.

3.3 Experimental Section

3.3.1 *Chemicals and Materials.*

All of the following chemicals and materials were used as received from the manufacturers: Nile red (Invitrogen, laser grade), Rhodamine 6G perchlorate (R6G) (Kodak, laser grade), acetone (J. T. Baker), sodium sulfate (Na_2SO_4; J. T. Baker, 101.8%), and indium-tin oxide (ITO)-coated microscope coverslips (SPI Supplies, sheet resistance 15-30 Ω/square). Deionized water (resistivity >18 MΩ·cm) was obtained through a Barnstead Nanopure water purification system (Thermo Scientific) and used for all aqueous solutions.

3.3.2 *Single-Molecule TIRF Microscopy.*

Single-molecule nanobubble imaging experiments were performed on a home-built TIRF system based on an Olympus IX70 inverted microscope. An Olympus Apo N 60× 1.49 NA objective (with an external 1.5× magnification on the microscope) and a 532 nm laser (CrystaLaser) source were used. With a constant 10 mW (2.5 kW/cm^2) excitation illumination, the fluorescence images were filtered with an ET590/50m emission filter (Chroma Technology Co.) and collected on an electron-multiplying CCD (EMCCD) camera (iXon Ultra 897, Andor) cooled

to -85 ^{o}C. Images were recorded at 50 ms exposure time (frame rate 19.81 Hz) and with an amplifier gain of 300. A thin polydimethylsiloxane (PDMS) film with a 2-mm-diameter hole was placed on the ITO surface to define the working electrode and the electrochemical cell, in which a 6 µL of dye-containing solution was added. A 0.5-mm-diameter Pt wire was placed in the solution as a quasi-reference electrode (QRE)/counter electrode. An EG&G 273A potentiostat (Princeton Applied Research) was used to apply the electrostatic potential across the ITO working electrode with respect to the Pt QRE.

3.3.3 *Image Analysis.*

Single-molecule fluorescence images and videos were analyzed using the ThunderSTORM plug-in in ImageJ.[38] Each single molecular fluorescence spot is described by a point spread function (PSF), which is fitted with a two-dimensional (2D) Gaussian function to localize the center position. The total number of fluorescent spots was counted as the number of detections. The number of detections was plotted versus fluorophore concentration. Error bars are reported as plus/minus one standard deviation of three repeated measurements.

3.3.4 *Single-Molecule Tracking.*

Tracking of fluorescent puncta was performed using the TrackMate plug-in in ImageJ.[39] Briefly, fluorescent puncta were detected above a user-set threshold using the Laplacian of the Gaussian (LoG) as a blob detector. Puncta were tracked and linked to other puncta in adjacent frames within a 150 nm displacement. The number of frames for one trajectory was converted to duration times using a frame rate of 19.81 Hz.

3.4 Results and Discussion

3.4.1 *Nanobubble imaging with Nile red.*

Figure 3.1A is a simple scheme of the electrochemical cell and the TIRF setup used for imaging single hydrogen nanobubbles.[31] A custom-built TIRF microscope was used to detect single fluorophore molecules (e.g., Nile red and R6G) near the surface of a transparent indium-tin oxide (ITO) electrode. A small drop of an aqueous solution containing low concentration fluorophores (pM to nM) was placed on top of the ITO surface; A negative potential was applied onto the ITO electrode vs a Pt QRE; H_2 nanobubbles were generated on the ITO electrode due to the electrochemical reduction of water ($2H_2O + 2e^- = H_2(g) + 2OH^-$). The most probable anodic reaction on the Pt QRE is the oxidation of water ($2H_2O = 4H^+ + 4e^- + O_2(g)$).[31] Nanobubbles were fluorescently labeled and imaged due to the transient adsorption and desorption of individual fluorophore molecules at the nanobubble's gas/water interface. With TIRF-based imaging, only bubbles that are smaller than ~150 nm in height may be detected due to the exponential decay of the evanescent wave with distance.[31]

In this work, we set out to use Nile red to probe the hydrophobicity of nanobubble's gas/water interface due to Nile red's unique solvatochromic behavior.[36,40] Nile red has been extensively used in biological studies to monitor various hydrophobic environments, such as intracellular lipid droplets, because they are nearly nonfluorescent in highly polar solvents such as water, but are strongly fluorescent in a nonpolar medium.[36] The solvatochromism of Nile red is explained in terms of a twisted intramolecular charge transfer (TICT) process (Figure 3.1B).[40] In a polar environment, the diethylamino group attached to the rigid ring undergoes a rotation, yielding an electron transfer and thus a non-radiative energy release. A large increase in fluorescence intensity can be expected when Nile red enters a nonpolar environment from a polar

environment. This allows Nile red to be used as an ideal fluorescent probe for nanobubble's gas/water interface. As depicted in Figure 3.1B, while Nile red molecules get adsorbed on the nanobubbles surface, it is expected that they undergo a change in their molecular configuration (i.e., untwist) and begin to fluoresce. Moreover, the use of Nile red as a nanobubble labeling agent may bring an added benefit due to its nearly nonfluorescent nature in water, which can reduce fluorescence background (noise).

Due to its poor solubility in water,[41] however, it is essential that we use a small amount of acetone to facilitate the dissolution of Nile red in the testing solution. Ratios of acetone/water have been carefully adjusted to reduce the unwanted fluorescent contaminants which may be brought into the system from the acetone. We find that a 1% acetone/water (volume) mixed solvent can be used to dissolve Nile red in the imaging solution without a significant increase in the fluorescence background (Figure S 3.1). We also confirmed that the introduction of 1% acetone into water does not generate nanobubbles from solvent mixing or exchange (Figure S 3.1).[42] Unless otherwise noted, all Nile red solutions used in this work contain 1% acetone.

Figure 3.1C displays eight fluorescence images taken from a potential scan, from 0 to -2.0 V vs. a Pt QRE, using 20 nM Nile red. A dark background can be observed when no potential is applied, or the potential is too low to reduce water. It is believed that the clean background is due to both the fluorescence quenching when fluorophores are near the conductive ITO surface and their fast diffusion and short resident time inside the evanescent field, as well as the non-fluorescence property of Nile red in water. Strong fluorescence spots are observed starting at around -0.7 V, indicating successful detection of H_2 nanobubbles. More bubbles are detected at higher negative potentials, as expected. To our knowledge, this is the first time a solvatochromic fluorophore has been used to label and image surface nanobubbles. Because Nile red is essentially

non-fluorescent in water and highly fluorescent in polar solvents, the fact that one can "see" individual fluorescence-labeled nanobubbles with Nile red as one can do with R6G and other conventional fluorophores suggests that the gas/water interface at the nanobubbles surface is indeed hydrophobic in nature. Most literatures have been focusing on studying the hydrophobicity for the interface between the bubble and solid surface, with only a few reports on solution/gas interface. Our results visually prove that the gas/solution interface is hydrophobic.[3,43,44,45,46] When a Nile red molecule collides and adsorbs onto the bubble surface, the change in solvent polarity is sufficient for it to start fluorescing. Noticed that Nile red undergoes reduction at -0.1 V vs Ag QRE, resulting in nonfluorescent reduced form NRH_2.[47] The fluorescent labeling can still be seen at a more negative potential (i.e., -1.0 V vs Pt QRE) suggests that bubbles are labeled by Nile red.

Although the general observation with Nile red is somewhat similar to our previous results with R6G and other Rhodamine dyes, Nile red molecules have exhibited several unique labeling behaviors. First, we have seen some weak but noticeable single-molecule detections of Nile red at potentials as early as -0.5 V vs Pt QRE (Figure 3.1C). Although it is difficult to believe that these detections are associated with nanobubble labeling, they may be due to changes in local polarity of the aqueous environment as H_2 molecules are initially formed from some highly active locations on the ITO. Second, unlike in the R6G case (Figure S 3.2), some of the Nile red-labeled events show a drastic increase in fluorescence intensity at potentials more negative than -1.0 V. As shown in Figure 3.1C, some of these spots with extended lifetime and high intensity are labeled with yellow boxes. In fact, their intensities can be 10 or 20 times higher than the single-molecule labeling events. As will be discussed in greater detail in the following section, this drastic increase in intensity suggests that nanobubbles are now labeled by multiple fluorophores at higher negative potentials, which is a unique feature of Nile red. Third, unlike with R6G and other Rhodamine

fluorophores where bubbles are more or less randomly and transiently labeled, Nile red tends to preferably label only a small fraction of the nanobubbles especially at potentials more negative than -1.1 V, as evidenced by higher labeling frequency (Figure 3.1C and Figure S 3.3). As one can see from Figure 3.1C, nanobubbles are labeled somewhat randomly between -0.7 and -1.1 V. However, between ~-1.1 and -1.5 V, the number of low-intensity spots starts decreasing while both the number and the locations of the higher intensity spots are relatively unchanged. Only a few high-intensity spots are seen at -2.0 V. A more detailed trace is shown in Figure S 3.4.

Figure 3.2A shows how the number of detected nanobubbles changes with potential (blue trace) in the range of interest from -0.5 to -2.0 V, when the electrode potential was scanned from 0 to -2.0 V and back to 0 V. As a comparison, we have also plotted the simultaneously recorded faradaic current on the ITO electrode (red trace) in the same graph. The frequency of nanobubble detection is defined as the counted number of nanobubbles per frame (detections per frame). While the faradaic current does not increase until about -1.2 V, the optical detection shows a fast increase starting at around -0.7 V before reaching a maximum value of about 25 bubbles/frame at about -1.0 V, which then decays at higher potentials. Compared to the current trace, the optical trace shows a significantly higher sensitivity detecting nanobubble formation at a much earlier stage. This higher sensitivity is in agreement with our previous results with R6G and can be attributed to the high sensitivity of single-molecule fluorescence labeling.[31] The initial increase in detection frequency can be explained by the increasing rate of water reduction with potential and the increasing rate of nanobubble nucleation, whereas the decay can be ascribed to the continued growth in nanobubble size. As we reported previously, nanobubbles are expected to grow in size with increasing negative potentials leading to a greater distance between the fluorophore and the ITO surface. This in turn “lifts” fluorophores away from the ITO surface or even out of the

evanescent field. Therefore, larger bubbles may not be effectively detected at higher negative potentials.

Figure 3.2B shows the fluorescence intensity (counts) of individual Nile red-labeled H_2 nanobubbles when the electrode potential was scanned from 0 to -2.0 V and back to 0 V. Each dot in the graph represents the fluorescence intensity (Y-axis) of a single nanobubble and the potential (X-axis) at which it was detected. Overall, there are 3798 detected nanobubbles collected from one potential cycle in Figure 3.2. A white horizontal dash line is given, which marks the average intensity of all nanobubbles detection events at -0.75 V. Interestingly, the fluorescence intensity of each nanobubbles detection event was seen to increase with potential, which is completely opposite to that observed with the R6G fluorophores, where fluorescence intensity was the highest at lower negative potentials when bubbles were initially detected and dropped with increasing negative potentials (Figure S 3.2).

This increasing trend in fluorescence intensity is largely due to the appearance of the super-bright spots, as seen in Figure 3.1C and Figure 3.2B. Compared to the <300 cts intensity for single Nile red-labeled nanobubbles at potentials before -1.0 V, many of these super-bright spots reached 2000 cts. A few of the ultra-bright spots even reached 6000 cts! The appearance of such super-bright spots suggests that these nanobubbles were co-labeled by multiple Nile red molecules. Although we do not know the exact number of fluorophores on each spot, it is estimated that there are at least 10 to 20 of Nile red molecules co-adsorbed on these super-bright bubbles. For example, if one assumes each Nile red molecule fluoresces independently at a 300 cts intensity, detecting a 6000 cts total intensity would mean that there are about 20 Nile red molecules co-labeling the same nanobubbles! As will be shown in a later section, we have seen a clear transition from single-

molecule labeling to multiple-fluorophore labeling as we gradually increase the Nile red concentration.

Another remarkable feature of these super-bright spots is their significantly longer duration. Compared to the short duration (~0.138 s, Figure S 3.5) for single-molecule labeled events collected before -1.0 V, most of the super-bright spots have durations longer than 3.0 s! A few events (e.g., yellow and green dots in Figure 3.2B) are even longer than 10 s! This drastic increase in the fluorophore's resident time on nanobubble surface is not completely understood at this moment. However, we believe it could reflect a stronger fluorophore-nanobubble interaction, which may be due to a change in the hydrophobicity of the gas/water interface when bubbles grow in size. A more plausible explanation is that it is likely that Nile red molecules start to form molecular aggregates or molecular clusters on nanobubbles surface due to the unique hydrophobic/hydrophilic property of the gas/water interface. The formation of aggregates/clusters may further increase their hydrophobicity leading to a stronger affinity to the bubble surface.

To further study Nile red's labeling characteristics for surface nanobubbles, we have compared nanobubble imaging results using Nile red and R6G at the same experimental conditions (Figure S 3.5 and Figure S 3.6). We again confirm that Nile red is unique to R6G because it prefers to have selective and multiple fluorophores labeling as evidenced by the higher intensity and longer duration time. Nile red would stay at the bubble surface much longer when there are multiple fluorophores absorbed at a more negative potential. More details are presented in the following section.

3.4.2 *Potential-dependent Nile red labeling.*

Figure 3.3 displays a series of random-selected fluorescence-time traces collected on ITO during a potential scan from 0 to -2.0 V vs Pt in water containing 20 nM Nile red and 1 M Na_2SO_4.

Such a comparison demonstrates how Nile red's nanobubble labeling behavior changes with increasing negative potentials. At relatively lower negative potentials, nanobubbles labeling events are characterized by an abrupt increase in intensity followed by a relatively constant intensity and a quick drop back to the baseline. Such labeling behavior is indicative of single-molecule labeling similar to nanobubble labeling with R6G. On the other hand, as the applied potential moves further in the negative direction, nanobubble labeling events start to show multiple intensity steps in each labeling event. This result strongly suggests that nanobubbles are now labeled by multiple Nile red molecules. Interestingly, some of the labeling traces at higher negative potentials show a continuously increased intensity with potential (time) and a much higher intensity value compared to the single- or multi-step traces observed at the lower negative potentials. It is likely that there are 10s of Nile red molecules involved in these super-bright spots. It is interesting to point out that most of these super-bright labeling events have a remarkably long lifetime, many of which exceed 20 s. To further examine this interesting long-lasting labeling behavior, we studied nanobubble labeling at constant -1.0 V potential with Nile red. As shown in Figure S 3.7, some nanobubbles can be labeled continuously for more than 125 s! This long lasting nanobubble labeling response further confirms that electrochemically generated surface nanobubbles can be very stable under certain conditions (More discussion on long-lived nanobubbles in the later section). These results are in stark contrast to the observations made with R6G and other Rhodamine-based dyes. For R6G, most of the labeling events are transient and shorter than 0.2 s. In addition, we could barely detect any nanobubbles labeled by two or three R6G molecules even when their concentration was above 10 nM! We also explore the labeling behaviors of Nile red at five different constant potentials, -0.8V, -0.9V, -1.0V, -1.1V, and -1.2V (Figure S 3.8). Different potentials are expected to generate bubbles of different sizes. Under various potentials, we observed similar multiple

fluorophores labeling and similar proportions of multiple fluorophore adsorptions. Interestingly, there is no significant difference in fluorophore intensities. This is somehow unexpected because, at a more negative potential, bubbles grow higher, where the fluorophores are lifted lead to a lower intensity. However, we understand that Intensity might be a good index of bubble height since there are multiple fluorophore labeling.

Because the size of electrochemically generated H_2 nanobubbles increases with potential, our results on potential dependent bubble labeling may have suggested that smaller bubbles are normally labeled by single fluorophores whereas larger bubbles are more easily labeled by multiple fluorophores. As reported from our previous study, most H_2 nanobubbles generated before -1.0 V are below 40 nm in height and they grow to more than 100 nm when the applied potential is more negative than -1.5 V.[31] A multi-fluorophore labeling event must involve a second molecule adsorbing onto a bubble surface with a Nile red already adsorbed. The increased likelihood of multi-fluorophore labeling on larger bubbles may be due to the increased collision frequency of fluorophore molecules onto the bubble surface, which is proportional to the nanobubble radius,

$$f = 2\pi DCrN_A \qquad \text{Eq 3.1}$$

where D is the diffusion coefficient of Nile red, C is its bulk concentration, r is the radius of the hemispherical nanobubble, N_A is Avogadro's number. As f increases, the probability of observing two molecules colliding on the same nanobubble increases accordingly to the Poisson statistics. As Eq 3.1 indicates, the collision frequency of Nile red with bubble surface is also proportional to the Nile red concentration. Once a Nile red molecule adsorbs on a bubble surface, the adsorption of a second Nile red molecule “sees” the first molecule is related to the average frequency of bubble adsorption. This of course is strongly related to Nile red concentration, which will be investigated in the following section.

3.4.3 *The effect of Nile red concentration.*

Most of the multi-fluorophore labeling results mentioned so far were collected using 20 nM Nile red. We expected that we would be able to observe a clear transition from single-molecule labeling to multi-fluorophore labeling if we dial down the concentration of Nile red. In Figure 3.4A**,** we compared the labeling behavior of Nile red at -1.0 V constant potential at four concentrations from 0.1 to 1.0 nM by plotting out the intensity-time traces of individually labeled nanobubbles. For each concentration, we randomly selected three labeled spots (6×6 pixels) and plotted the intensity-time trace of each spot for the same 40 s time period. There are two important observations one can readily make from these traces. First, there is an apparent increase in the nanobubble labeling frequency with increasing Nile red concentration. At 0.1 nM, each bubble was labeled only once during the 40 s period. At 0.3 and 0.5 nM, however, bubbles started to be labeled two or three times in this period. At 1.0 nM, nanobubbles were repeatedly labeled over and over. It is likely the increased labeling frequency is due to an increased collision frequency of fluorophores on to nanobubble surface for a higher concentration solution, as expected. Second, while most of the detection events at lower concentrations (0.1 to 0.5 nM) show nearly the same levels of intensity change indicating bubbles are labeled by a single fluorophore, at 1.0 nM, some labeling events start to show multiple levels of intensity changes suggesting bubbles were co-labeled by multiple fluorophores.

To give a closer look at multi-fluorophore labeling events, Figure 3.4B displays a set of nine detection events consisting of one, two, and three intensity levels. The relative uniform step size and the abrupt switching between the “on” and “off” states suggest that these stepwise fluctuations in fluorescence intensity are due to individual fluorophores adsorbing and desorbing on the bubble surface. If we define a single labeling event by identifying the initial intensity

increase and the final intensity decrease, we can count the number of discrete steps in each event (and hence the number of Nile red fluorophores involved in the labeling event). Note, an event is considered as finished when the intensity returns back to the baseline for >3 frames. And we observed from Figure 3.4C that multi-fluorophore labeling events are more frequent at higher Nile red concentrations.

Interestingly, we have found that the multi-fluorophore labeling events have a longer duration time than the summation of the duration time for single-fluorophore labeling events, which could suggest the presence of some sort of intermolecular interactions when multiple Nile red molecules are co-adsorbed on the same nanobubble surface. This is in agreement with our observation in Figure 3.2. We plotted the average time durations for events containing single, double, and triple fluorophores in Figure 3.5. The average resident times for events containing one, two, and three Nile red are 0.38, 1.2, and 2.1 s, respectively. One can see doubling and tripling the number of fluorophores indeed result in much extended resident times on the bubble surface.

The fact that we observed multi-fluorophore labeling with Nile red but not with other Rhodamine fluorophores under similar conditions suggests that there may be some kind of intermolecular interactions associated with Nile red. In other words, we believe that co-adsorbed Nile red molecules likely form some kind of molecular aggregates on bubble surfaces. Molecular aggregation of Nile red has been reported in literatures.[41,48] The observation of molecular aggregation on bubble surface is reflected from the prolonged residence time for multi-fluorophore labeling events as compared to a simple summation of the resident time of the single Nile red molecules. It is likely that these molecular aggregates have a higher affinity to the hydrophobic nanobubble surface compared to their monomers making it more difficult for aggregated Nile red molecules to leave the bubble surface.

3.4.4 *Long-lived nanobubbles.*

Nanobubbles are reported to have a long lifetime.[22] Surface nanobubbles are supplied by gas under a constant potential, so the stability is maintained. Figure S3.9 shows bubble intensity when potential supplied stops (OCP: open circuit potential). We can see that there are still bubble detections after 90 seconds, suggesting a long lifetime of electrochemically generated surface nanobubbles without gas supply. Also, intensity decreases along with time. This is an interesting observation because bubbles are expected to shrink down without gas supply, which would lead to increased intensity. This unexpected observation could be again due to multiple fluorophore labeling. Initially, bubbles are large and can be labeled by multiple fluorophores. As the bubble shrinks down, the surface area gets smaller, which provides not enough area to have more than one adsorbed molecule. Therefore, we hypothesized that the detections in later times (OCP time windows) are from single fluorophore, while the initial detections are from single and multiple fluorophore adsorptions. We also tried to validate the bubbles' long-lived stability by using R6G, which provides single fluorophore adsorption in most cases. We measured the number of detection per frame, starting from applying a constant reductive potential -1 V (yellow shaded area) for 50 s, and following by the open circuit potential (OCP, meaning no potential is applied) for 925s (Figure S 3.10). It can be seen that the number of bubble detection increases during the -1 V potential supplied, suggesting that the bubbles are nucleating. And the number of detections reaches a plateau at around frame 1,200 (not clearly shown in Figure S 3.10), implying that both bubble generation and detection are at an equilibrium state so that the number of detections is not changing. Once the potential is removed (from frame 1,500), the number of detections starts to decrease and maintain at 10 detections per frame to the end (frame 20,000). This is a very surprising finding that detections still exist after 15mins without potential supply. To further

understand how long bubbles actually exist, a "decay" constant is calculated by fitting the first-order exponential decay to the number of detections (Figure S 3.11 and Table S 3.1). The definition of decay constant here is the time at which the population of the detection is reduced to 1/e times its initial number of detections. The larger decay constant is, the more bubbles exist for a longer time. From Table S 3.1, we don't see a significant difference of decay constant in different constant voltages, implying that bubbles generated at different voltages could have similar lifetimes.

3.4.5 *Estimation of the number of bubbles at the electrode surface.*

We see that Nile red selectively labels a certain set of bubbles, and it would be of great fundamental importance to know the actual number of bubbles generated at the electrode surface. Instead of using Nile red, R6G would be more appropriate because it can label all possible bubbles via single fluorophore adsorption. To estimate the number of nanobubbles, clustering detections would be a good approach. We believe that there are hundreds of nanobubbles on the surface, and they are possibly labeled several times. The idea behind clustering is that if a bubble is in coordinate (100,100) nm, then any detections within (100-50, 100+50) would belong to the same bubble labeling (A simple explanation, the bubble here is assumed to be squared-like, and has lengths to be 100nm). To practically cluster nanobubbles, we utilized the K-means algorithm from machine learning.[49] The algorithm behind K-means is to partition detections into k clusters in which each observation is grouped to the cluster centroid with minimum distance overall.[50,51] In this study, the position of each detection is used as the input for clustering. There are several assumptions for K-means clustering in this study: 1) bubbles are spherical (circular shape); 2) Each bubble has a similar size; 3)Each bubble has equal probability to be labeled and detected. One major drawback of K-means clustering is the number of clusters k needs to be preset. A well-known method to obtain the optimal k value is by "elbow method" which originated in 1953,[52]

where the sum of squared distance between each point and the centroid in a cluster is plotted over the number of clusters (Figure S 3.12). In this plot, we can see that the distance (y-axis) will decrease and has rapid change at a point that further increase in the number of clusters does not decrease the squared distance with comparable amounts. And we called this point the “elbow point”, which is also the optimal k number ---110. The value of 110 means that detections can be clustered into 110 partitions, in our case, nanobubbles. Visualization of the clustering is shown in Figure S 3.13. We can see that detections are clustered into 110 bubbles (colors), and the size of each cluster is roughly 2.5 μm in diameter. This size estimation is larger than what we expect for nanobubbles, and we noticed that edge bubbles are larger than the central ones. All these observations imply that K-means clustering might not be an appropriate algorithm in bubble clustering. More work is needed to better estimate the number of nanobubbles generated at the electrode surface.

3.4.6 *Effect of potential scan rate on nanobubble detection.*

The nucleation and growth of nanobubbles are affected by the number of supplied hydrogen gas molecules, which is dependent on the rate of the potential scan. In Figure S 3.14, panel A shows accumulated detections using 1nM Nile red during cyclic voltammetry using 100mV/s, while panel B is in 400 mV/s. It is clearly observed that there are more detections using a lower scan rate. Bubbles only start to nucleate when surrounded gas molecules reach a saturation state. During cyclic voltammetry, the production of H_2 is heavily dependent on the rate of scanning potential. In a faster scan rate (i.e., 400 mV/s), water reduction is more frequently “on” and “off”, resulting in less continuous gas production. This leads to a harder bubble nucleation and growth and fewer nanobubble detections.

3.5 CONCLUSIONS

Our results have suggested that Nile red as a solvatochromic dye can be a useful and unique fluorophore for imaging surface nanobubbles. Nile red emits strong fluorescence once it is adsorbed at the surface of electrochemically generated H_2 nanobubbles, confirming the hydrophobic nature of the gas/water interface. Our results also suggest that Nile red molecules may form small clusters or aggregates on nanometer-sized bubble surfaces. By controlling the fluorophore concentration and the applied potential, one can selectively label a single surface nanobubble with one, two, three, and even more Nile red molecules at will. The use of Nile red and other solvatochromic fluorophores may provide some unique avenues for us to better probe and further understand the physical and chemical environment of the gas/water interface. We also confirmed the high stability and long-lived property of surface nanobubbles. By replacing Nile red with R6G, we observed that bubbles can still be detected for at least 15 mins without energy (i.e., gas) supply. The total number of nanobubbles was estimated by K-means algorithm, although more work needs to be done to validate this estimation. We believe that electrochemically generated nanobubble surfaces may be used as a unique platform for studying molecular interactions, aggregations, and even molecular reactions for fluorophore-labeled chemical species on structurally well-confined interfaces.

3.6 FIGURES

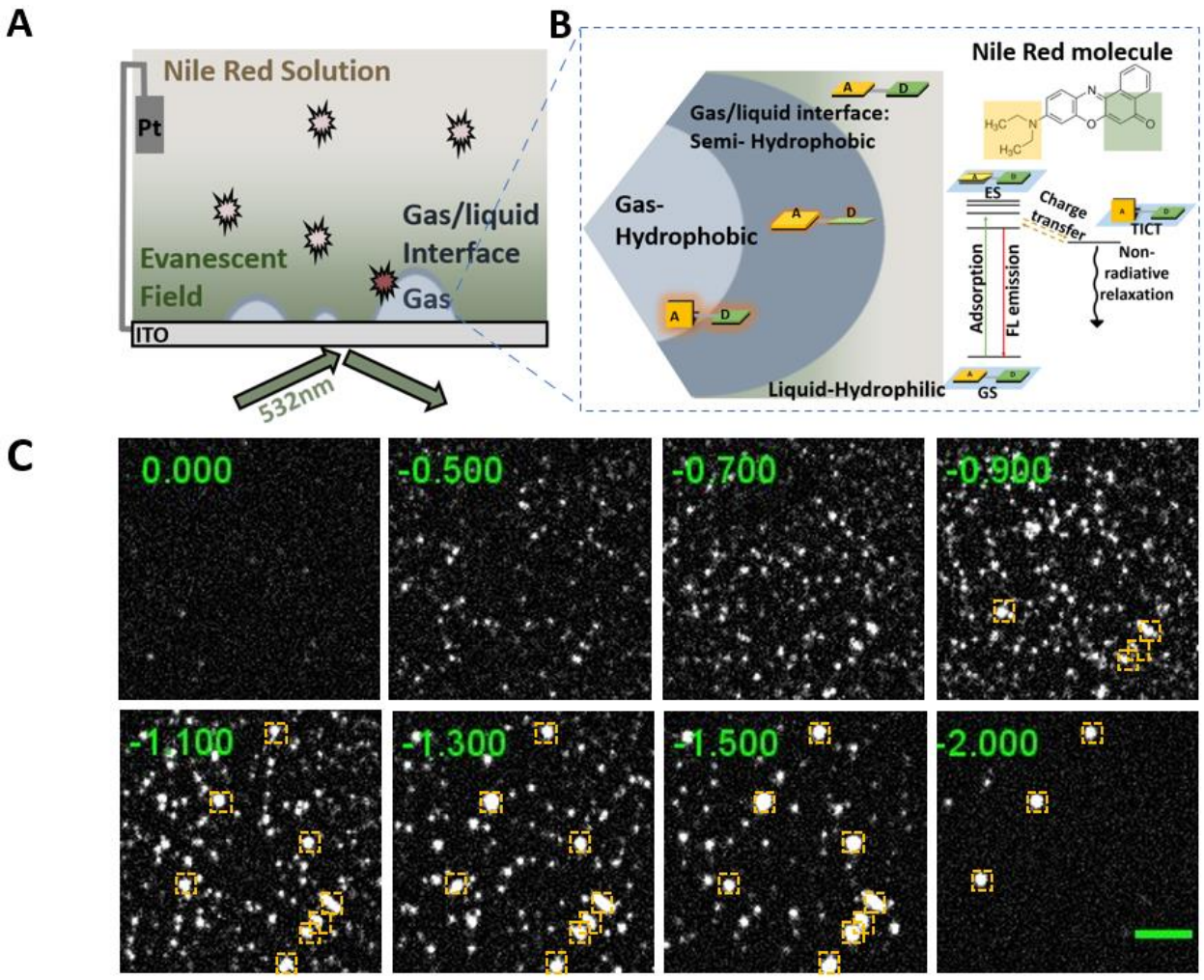

Figure 3.1.Single-bubble imaging with Nile red.

(A) Scheme of the experimental setup for imaging individual H_2 nanobubbles on an ITO electrode. (B) Nanobubbles are detected due to the adsorption of Nile red molecules at the gas/water interface. Molecular twisting of Nile red at the interface yields fluorescence. (C) A series of eight fluorescence images was taken from a 22.8×22.8 μm^2 area on an ITO electrode collected in a voltage scan at 100 mV/s from 0 to -2 V vs. Pt QRE in water containing 1 M Na_2SO_4 and 20 nM Nile red with 1% v/v acetone. (Scale bar: 5µm). Several high-intensity spots are boxed in yellow. The video was recorded at a 50 ms exposure time (frame rate: 19.81 Hz).

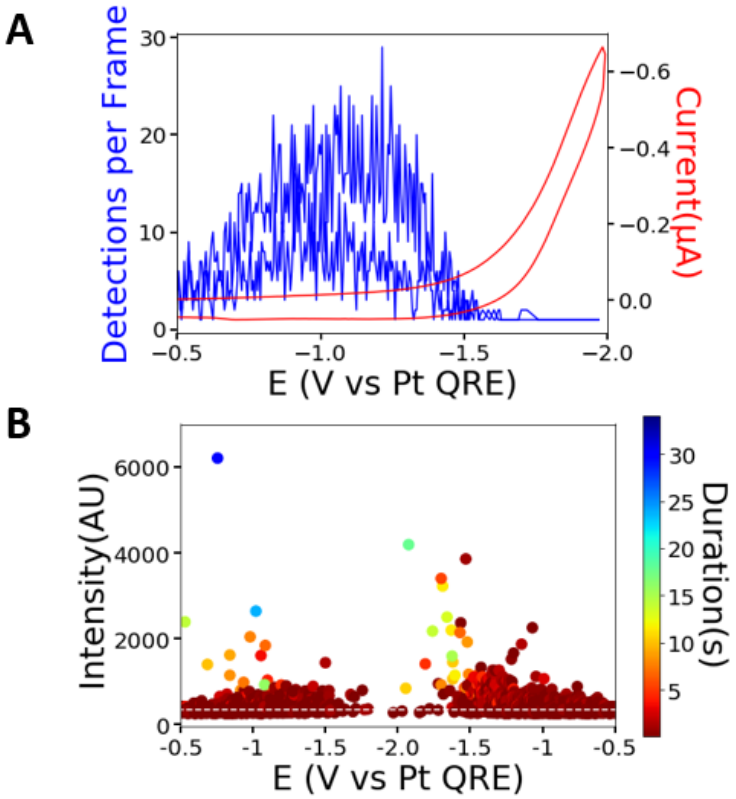

Figure 3.2 Detections per frame and long duration time of Nile red.

(A) A comparison between the rate of nanobubble detection (detections per frame) (blue) and the current-voltage response recorded on the same electrode (red). (B) A scatter plot showing the fluorescence intensity (counts) of individual H_2 nanobubbles in the potential range of interest from -0.5 to -2.0 V from the same recording. The color of an individual spot is representing the duration times(s); The color of the individual spot represents the duration of a specific labeling event.

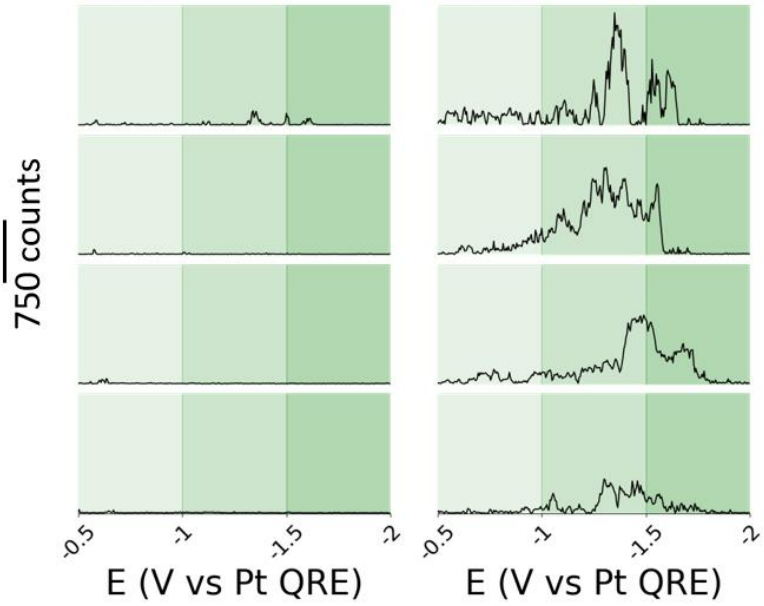

Figure 3.3 Potential-dependent nanobubble labeling with Nile red.

Representative fluorescence intensity-time traces showing eight randomly selected nanobubble labeling events detected from -0.5 V to -2.0 V. Green shaded areas from light to intense are marked to represent voltage segments from less to more negative direction. All traces were collected in a potential scan at 100 mV/s on ITO in water containing 20 nM Nile red and 1 M Na_2SO_4. Traces were obtained by averaging the total intensity of a 6×6 pixel area around the center spot.

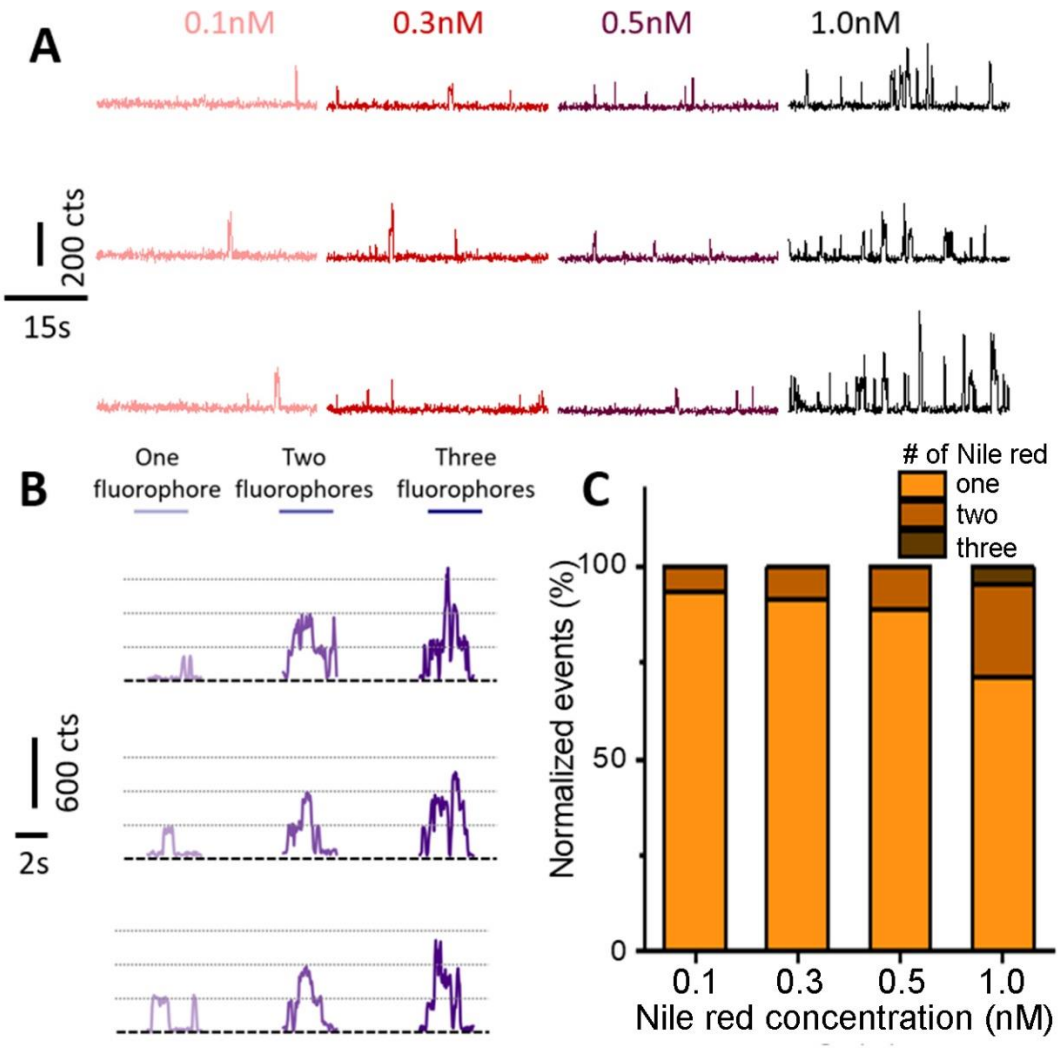

Figure 3.4 Singe-molecule nanobubble labeling at low Nile red concentrations.

(A) Fluorescence intensity−time traces showing three randomly selected bubbles detected at −1 V in water containing 0.1, 0.3, 0.5, and 1.0 nM Nile red with 1 M Na_2SO_4. Traces were obtained by averaging the total intensity of a 6 × 6 pixel area around the center spot. (B) Representative fluorescence intensity−time traces showing single and multiple fluorophore labeling were detected at -1V in water containing 1.0 nM Nile red with 1 M Na_2SO_4. (Traces were obtained by averaging the total intensity of a 6 × 6 pixel area around the center spot. (C) The frequency of different labeling behavior, color from light to dark represents more fluorophore labeling. Events (at least 200 events in total in each concentration) are normalized for each Nile red concentration.

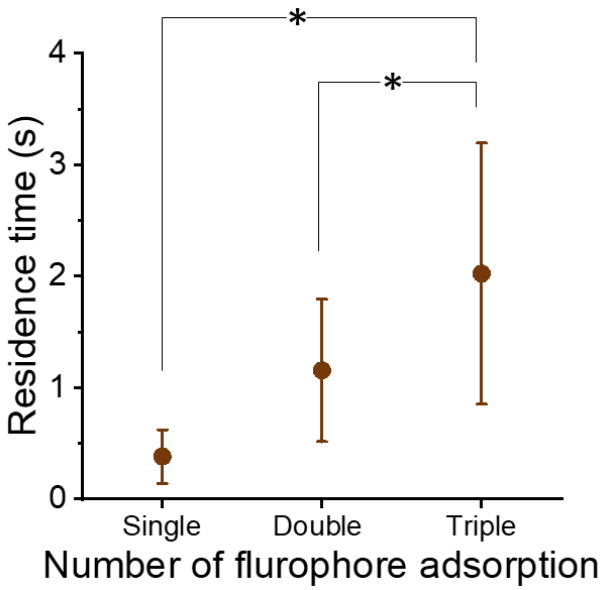

Figure 3.5 Residence time comparison

Scatter plot of the average duration time measurement for adsorption events containing single, double, and triple fluorophores. Data are collected at -1.0 V in water containing 5.0 nM Nile red with 1 M Na_2SO_4. The asterisk represents significant level (alpha) to be 0.05.

3.7 Supporting information

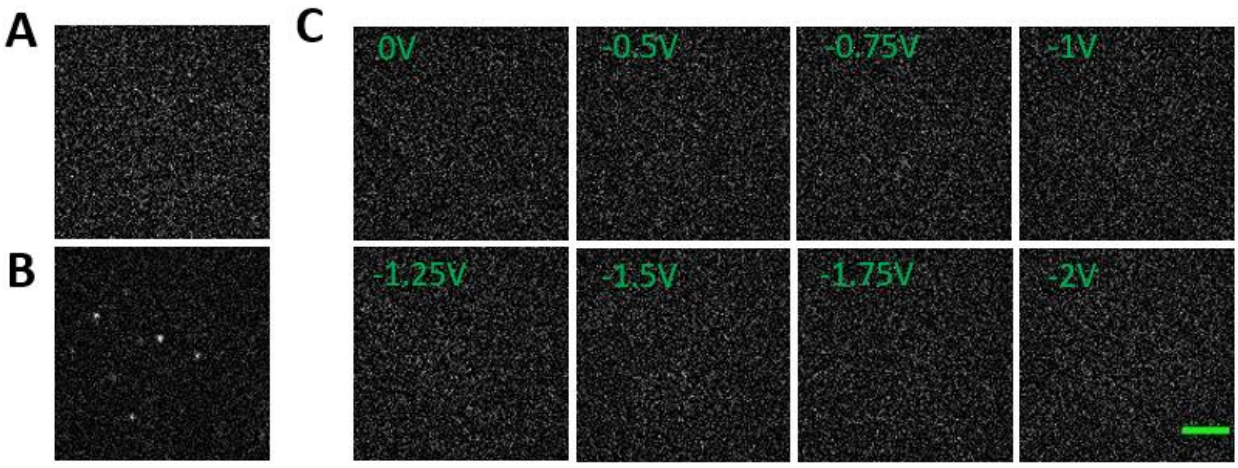

Figure S 3.1 Control experiments for solutions containing acetone.

(A) FEEM image selected from an experiment with 1 M Na_2SO_4 at a constant -1 V potential. (B) FEEM image selected from an experiment with 1 M Na_2SO_4 and 16.7% acetone at a constant -1 V potential. (C) A series of TIRF images of a 22.8 x 22.8-μm^2 area on an ITO electrode measured from a cyclic voltammetry scan from 0 V to -2 V at 100 mV/s vs. Pt QRE containing 1M Na_2SO_4 with 1% v/v acetone. (Scale bar: 5μm). Video was recorded at 0.05 s exposure time (Frame rate: 19.81Hz).

With only 1M Na_2SO_4, under a constant -1 V potential, no fluorescent spots can be detected. It indicates that pure electrolyte solution is free of fluorescent contaminants.
As an organic dye, Nile red readily dissolves in more nonpolar solvents. To proceed with water reduction, Nile red needs to be dissolved in water finally. Acetone is an ideal solvent that can serve both functions: Nile red can dissolve in acetone and acetone can be miscible with water. With 16.7% v/v acetone in water containing 1M Na_2SO_4, fluorescent contaminants are introduced (Figure S1 B). Under a constant -1V condition, H_2 bubbles are generated and are labeled by contaminants. To avoid introducing fluorescent contaminants, decreasing acetone ratio would help. With 1% v/v acetone, no fluorescent spots can be observed, suggesting that 1% acetone is free of fluorescent contaminants.

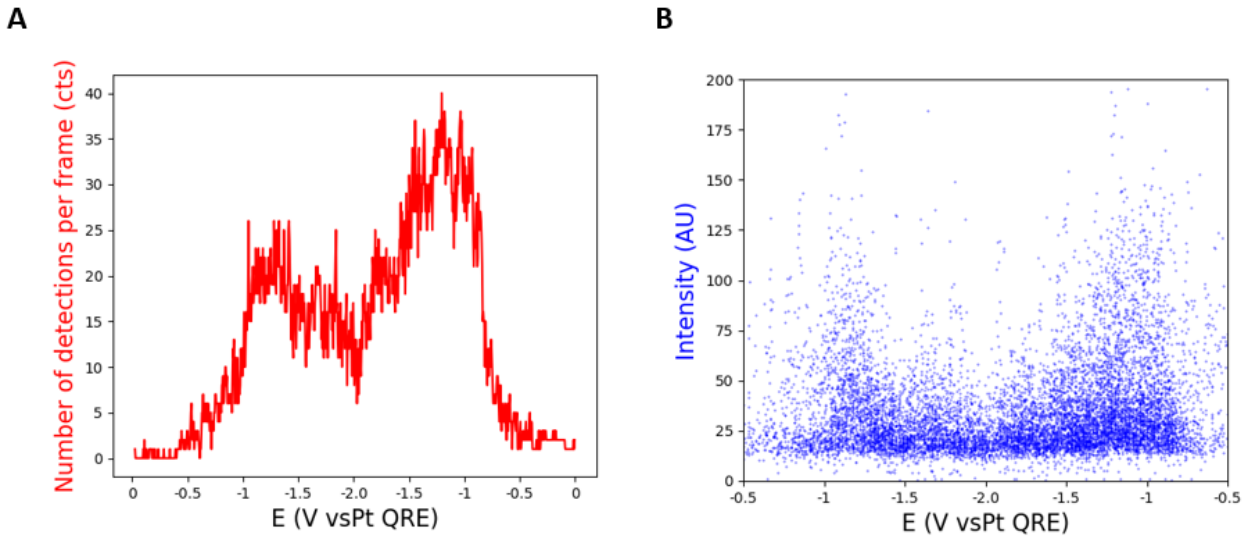

Figure S 3.2 Nanobubble labeling/imaging with R6G in a potential scan experiment.

(A) The rate of nanobubble detection (detections per frame) vs potential from a potential scan from 0 V to −2.0 V at 100 mV/s vs. Pt QRE in water containing 1 M Na_2SO_4 and 5 nM R6G with 1% acetone. (B) A scatter plot showing the fluorescence intensity (counts) of individual H_2 nanobubble detection events in the potential range of interest from −0.5 V to −2.0 V from the same recording. The photon counts of each fluorescent burst on one frame were converted from the total integrated fluorescence signal under the fitted 2D Gaussian function using ThunderSTORM.

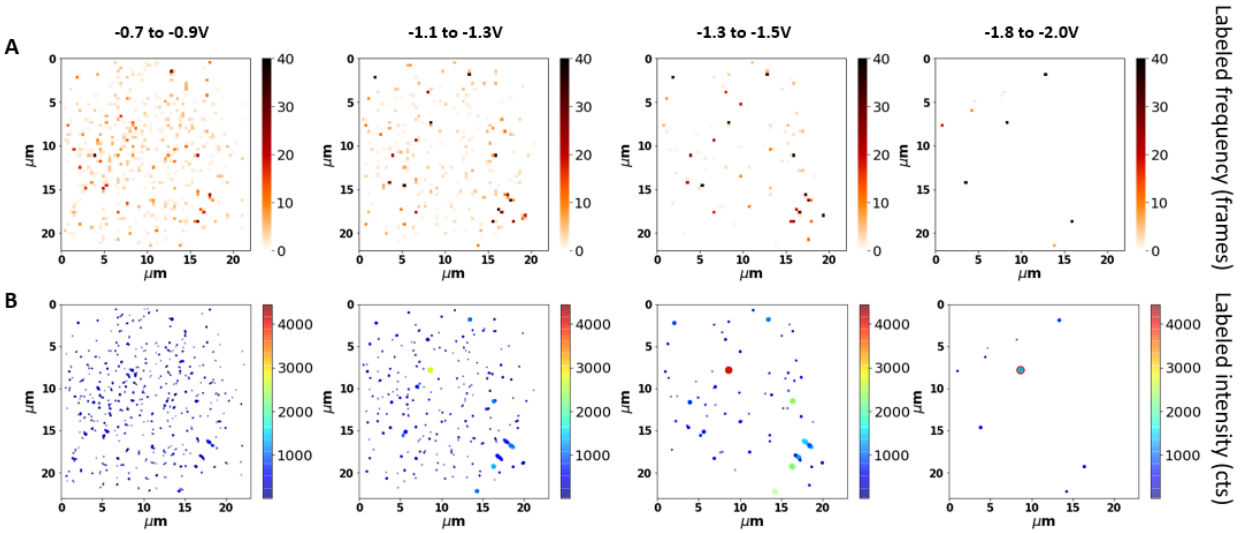

Figure S 3.3 Potential-dependent nanobubble labeling with Nile red.

Bubbles are labeled with more fluorophores and higher frequency at a more negative potential. Upper panel: four labeling frequency plots at each voltage segment. Each spot is a 2 x 2 pixel region, with color representing labeling frequency. The maximum frequency is 40 frames, meaning that bubbles are labeled at all frames in these voltage segment. Lower panel: Scatter plots showing the accumulated spatial distribution of H_2 nanobubbles with labeling intensity, represented by color and size. The larger and redder the spot, the higher intensity is. Images were recorded from a voltage scan at 100 mV/s from 0 to -2 V vs. Pt QRE in an aqueous solution containing 1 M Na_2SO_4 and 20 nM Nile red with 1% v/v acetone. The video was recorded at 50 ms exposure time (frame rate: 19.81 Hz).

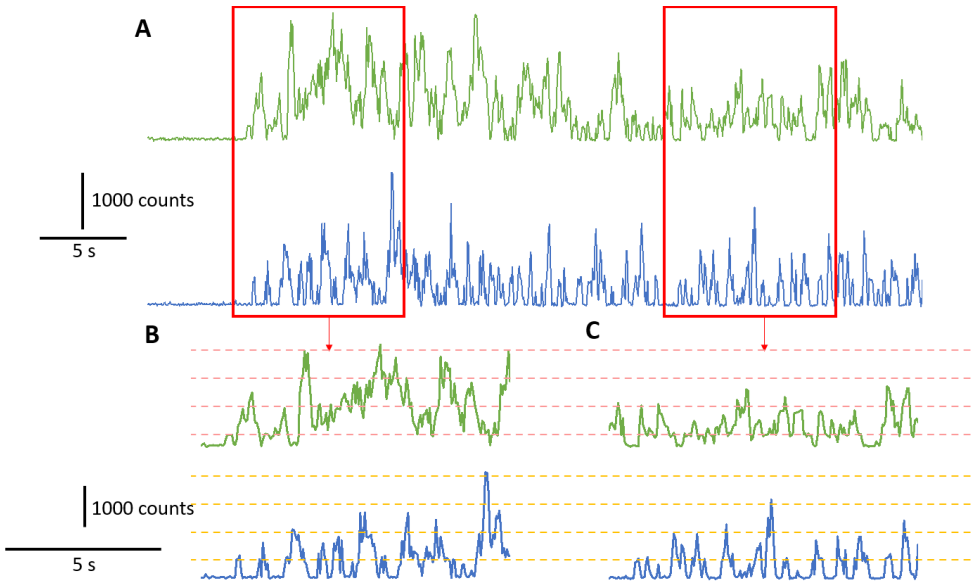

Figure S 3.4 Fluorescence intensity-time traces for nanobubbles labeling events using 15 nM Nile red.

(A) the applied voltage was at 0 V for the first 5 s and -1 V for the rest time. Panels (B) and (C) are zoom-in views of the two 10 s sessions in panel (A) after applying -1.0 V. Using high concentration, one can see that the nanobubbles labeling events are no long labeled by single molecules. Instead, the same nanobubbles were continuously labeled by multiple Nile red molecules the entire time the -1.0 V potential was applied. Fluorescence intensity-time traces for 5 nM Nile red (blue) and R6G (red) at -1 V. Traces were obtained by averaging the total intensity of a 6 × 6 pixel area around the center spot.

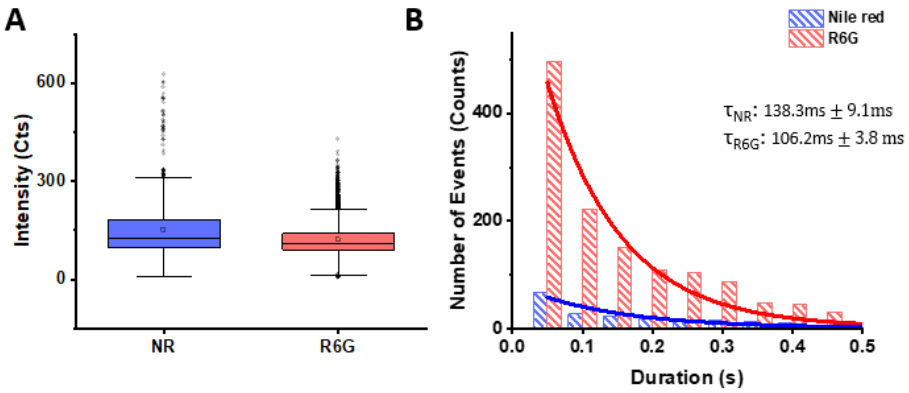

Figure S 3.5 Intensity and duration comparisons for nanobubble labeling events using Nile red and R6G.

(A) Intensity comparison box plot of 5 nM Nile red and R6G. Nanobubble events are collected under a constant -1 V applied potential (vs Pt QRE) in solutions containing 5 nM Nile red and 5 nM R6G with 1 M Na_2SO_4 electrolyte. The horizontal and vertical lines in each box represent the median and the 25^{th}–75^{th} percentiles, respectively; black dots represent outlier values. (B) Histogram of the duration of nanobubble detection events. Solid lines are the single-exponential decay that fits with time constants for Nile red and R6G: 138.3 ± 9.1 ms and 106.2 ± 3.8 ms.

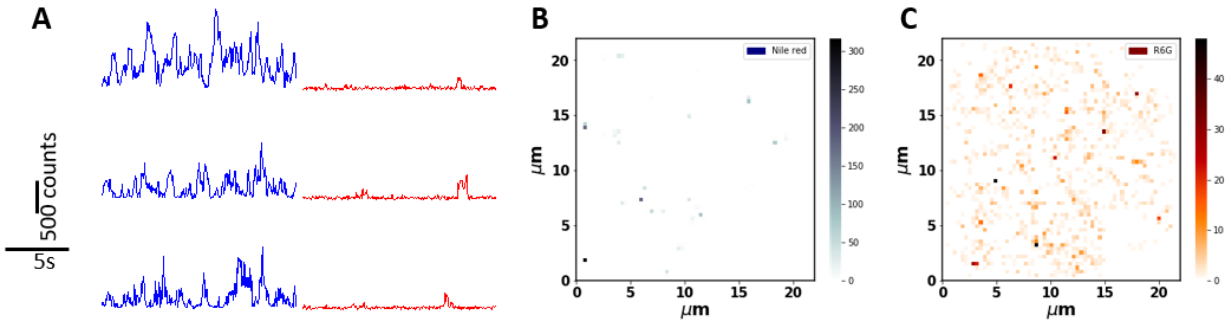

Figure S 3.6 Nanobubble labeling/imaging with 5 nM Nile red and R6G at -1 V.

(A)Fluorescence intensity-time traces for 5 nM Nile red (blue) and R6G (red) at -1 V. Traces were obtained by averaging the total intensity of a 6 × 6 pixel area around the center spot. (B) Labeling frequency plots for 5 nM Nile red (blue) and R6G (red) (C) at -1 V for total 600 frames.

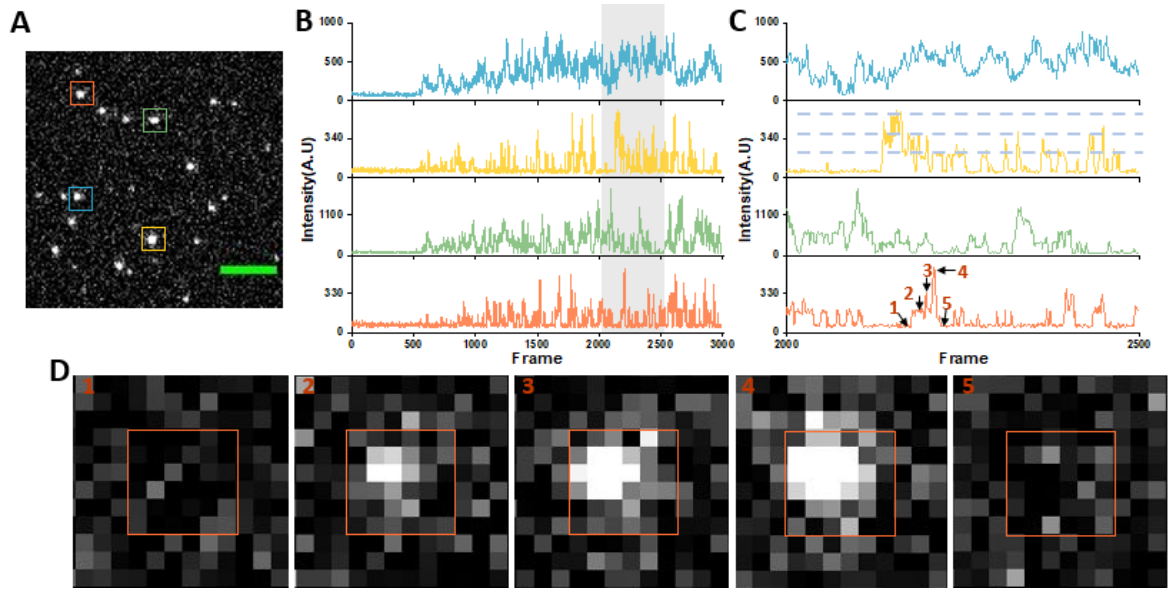

Figure S 3.7 Multi-fluorophore nanobubble labeling of 5 nM Nile red.

(A) A TIRF image taken at -1.0 V showing individual H_2 nanobubbles labeled by Nile red molecules. The locations of the four nanobubbles marked with color boxed, whose intensity traces are showing in (B) and (C). Images were taken in 5 nM Nile red and 1 M Na_2SO_4. (Scale bar, 5 μm.) Images were recorded at 19.8 frames/s with a 50-ms exposure time. In panel (B), the applied voltage was 0 V from the 1st to 500th frames and -1.0 V from the 501st to the 3000th frames. Panel (C) gives a zoom-in view of the grey shaded area in (B). Dashed blue lines were added to guide the eyes for the discrete stepwise increased in intensity. Arrows 1 to 5 mark the time points of the fluorescence images given in panel (D), which displays the fluorescence images of the same nanobubble during a three-step fluorophore labeling.

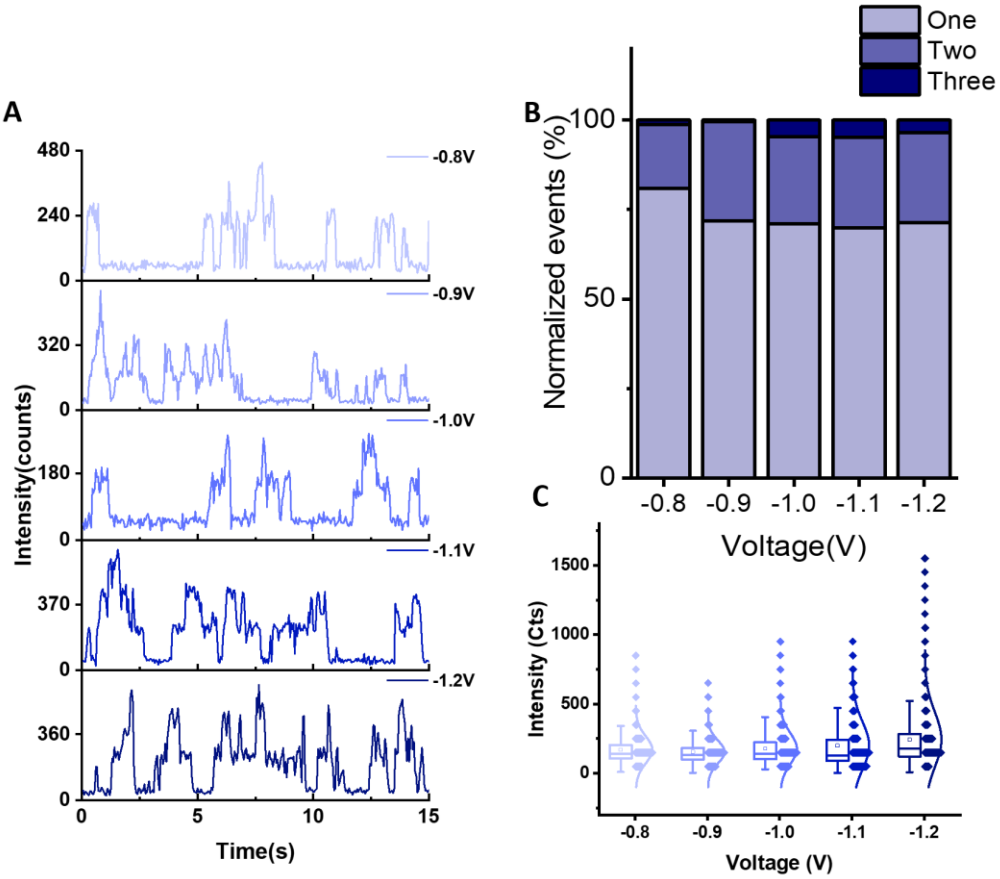

Figure S 3.8 Voltage dependency study

(A)Fluorescence intensity-time traces for 5 nM Nile red at -1 V constant potential. Traces were obtained by averaging the total intensity of a 6 × 6 pixel area around the center spot. Similar step-wise fluorescence-time traces are observed. (B) Frequency of different labeling behavior for 5nM Nile red at various constant potentials. Color from light to dark represents more fluorophore labeling. Events (at least 200 events in total in each concentration) are normalized for each condition. There is no significant difference observed across five potentials. (C) Intensity box plot for 5nM Nile red at various constant potentials. Color from light to dark represents indicates from -0.8V to -1.2V with a voltage step size of 0.1V.

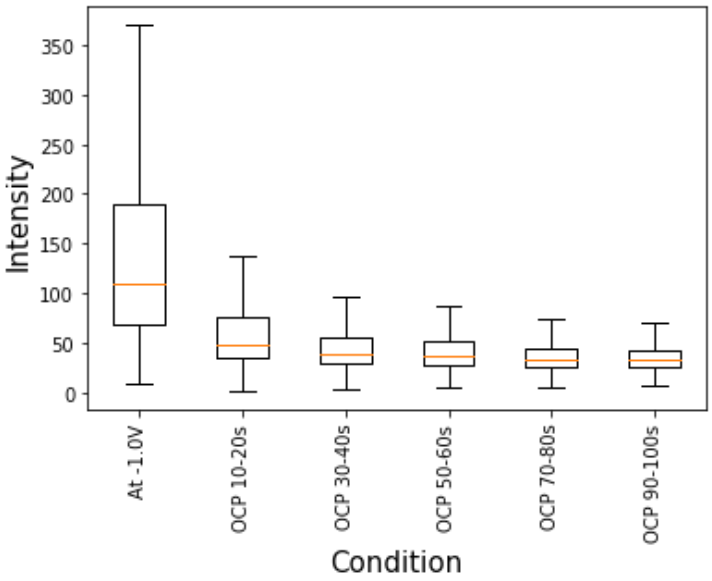

Figure S 3.9 Nanobubbles still get labeled after 90 s.

A box plot of fluorescence intensity after removing potential supplied. Measurements were taken at a constant of -1V initially, with an x-axis label at -1.0V. The potential is removed after 30 s, but measurements are continued. As labeled in the x-axis “OCT 10-20s”, meaning that this measurement was taken 10s after potential removal and total 10 s for the measurement.

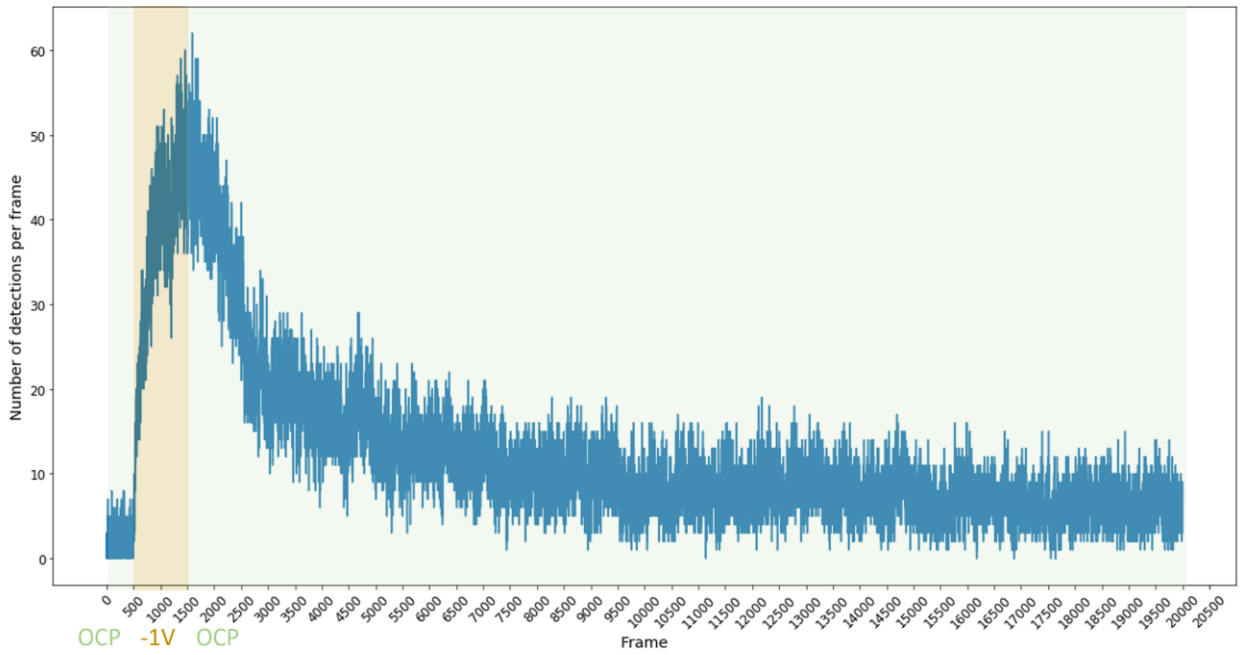

Figure S 3.10 Number of detections after potential removal.

The number of detections measured from a constant -1 V potential to open circuit potential (OCP) in a water solution containing 20nM R6G and 1M Na_2SO_4. Measurements start from OCP (green shaded, from frame 0 to frame 500), then a constant potential -1 V is applied (yellow shaded, from frame 501 to frame 1,500), and finally, OCP to the end (green shaded, from frame 1501 to 20,000).

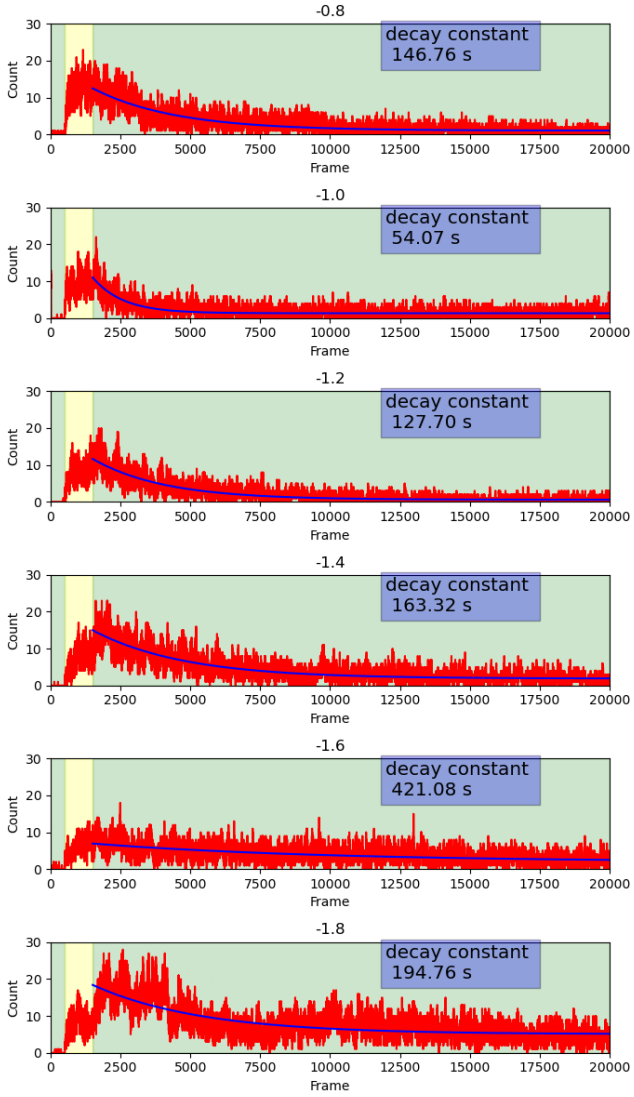

Figure S 3.11 Decay constant of the number of detections during OCP.

The number of detections are measured at different constant potentials, and the decay constant of the number of detections are extracted by fitting first-order exponential equation ($y = y_0 + Ae^{\frac{t}{\tau}}$, where y is the number of nanobubbles, y_0 is the offset of the number of nanobubbles, A is the corresponding number of events for time t with decay constant τ). Decay constants at various potentials are tabulated in Table S 3.1. Measurements were taken in 20 nM R6G and 1 M Na_2SO_4.

Table S 3.1.Decay constant for the number of detections during OCP.

VOLTAGE	DECAY CONSTANT (1/COUNTS)
-0.8	280.78 ± 218.98
-0.9	178.95 ± 45.75
-1.0	173.68 ± 169.15
-1.1	275.69 ±53.25
-1.2	235.23 ± 192.92
-1.4	236.62 ± 190.22
-1.8	160.59 ± 51.15

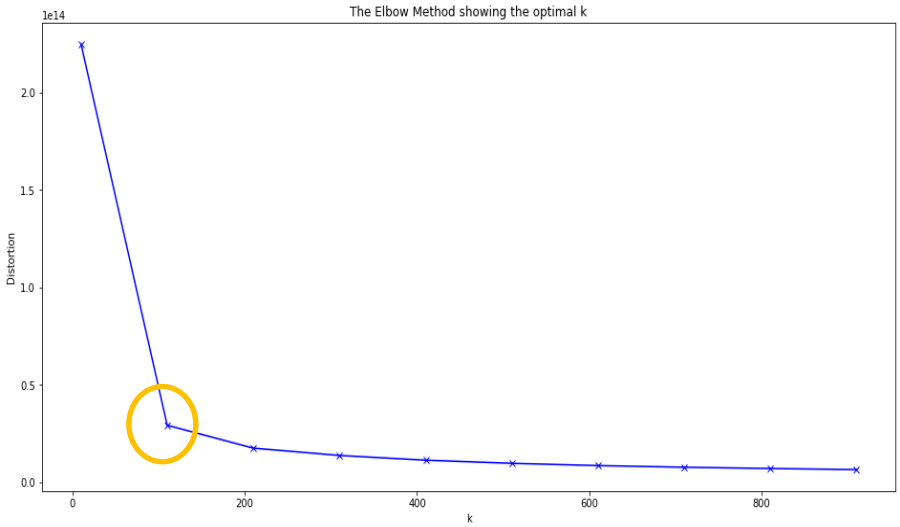

Figure S 3.12 Elbow plot for obtaining the optimal number of bubbles.

This graph is obtained by running 599,798 detections (positions of detections) in different values of k and calculating the average of within-cluster distance to the centroid (labeled as “Distance”). The yellow circle marks the “elbow” point in this plot, indicating the optimal k value is 110. Measurements are taken in a water solution containing 20 nM R6G and 1 M Na_2SO_4. Positions of detections are obtained from fitting 2D Gaussian functions using ThunderSTORM.

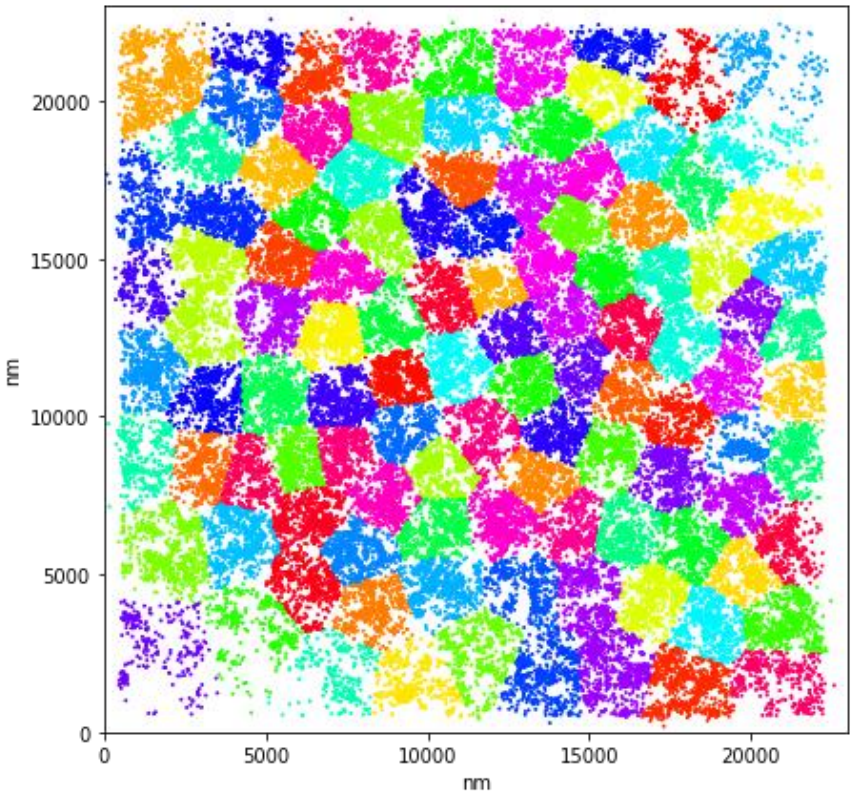

Figure S 3.13 Elbow plot for obtaining the optimal number of bubbles.

This plot is generated by using 110 clusters (nanobubbles) to label all 599,798 detections collected from 20nM R6G and 1M Na_2SO_4. Each color represents one cluster(nanobubble).

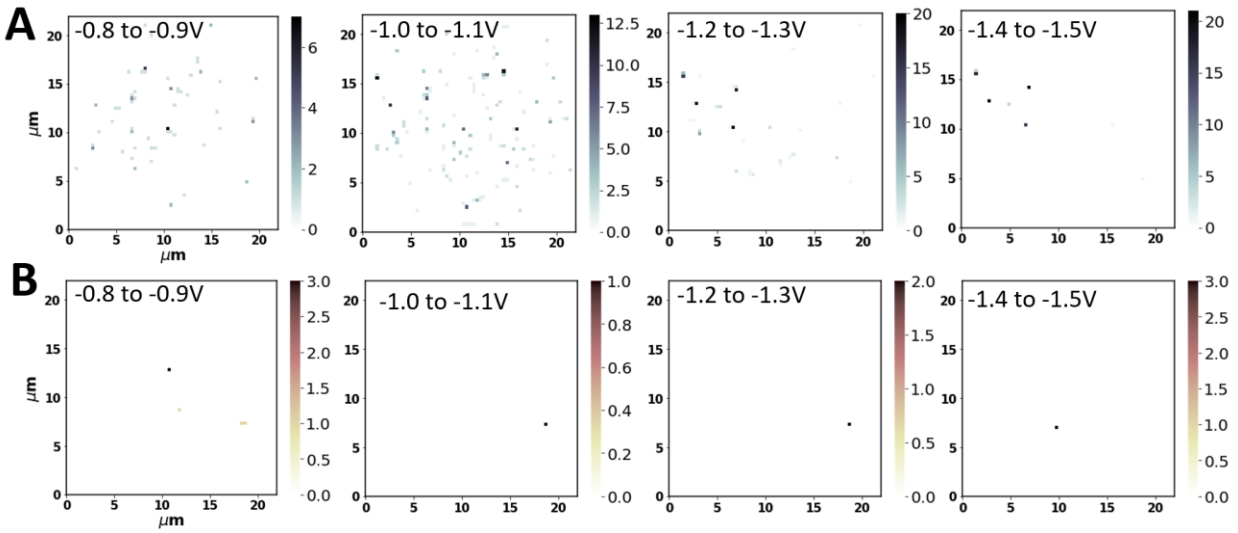

Figure S 3.14 Accumulated nanobubble detections.

Accumulated nanobubble detections using 100 mV/s (A) and 400 mV/s (B) in various potential windows. The color bar represents detection frequency. Detections are collected using 1 nM Nile red and 1M Na_2SO4. Positions of detections are obtained from fitting 2D Gaussian function using ThunderSTORM.

3.8 REFERENCES

(1) Lou, S.-T.; Ouyang, Z.-Q.; Zhang, Y.; Li, X.-J.; Hu, J.; Li, M.-Q.; Yang, F.-J. Nanobubbles on Solid Surface Imaged by Atomic Force Microscopy. *J. Vac. Sci. Technol., B Microelectron. Process. Phenom.* **2000**, *18*, 2573.

(2) Zhang, X. H.; Maeda, N.; Hu, J. Thermodynamic Stability of Interfacial Gaseous States. *J. Phys. Chem. B* **2008**, *112*, 13671–13675.

(3) Zhang, X. H.; Quinn, A.; Ducker, W. A. Nanobubbles at the Interface between Water and a Hydrophobic Solid. *Langmuir* **2008**, *24*, 4756–4764.

(4) Holmberg, M.; Kühle, A.; Garnæs, J.; Mørch, K. A.; Boisen, A. Nanobubble Trouble on Gold Surfaces. *Langmuir* **2003**, *19*, 10510–10513.

(5) Sun, Y.; Xie, G.; Peng, Y.; Xia, W.; Sha, J. Stability Theories of Nanobubbles at Solid–Liquid Interface: A Review. *Colloids Surfaces A Physicochem. Eng. Asp.* **2016**, *495*, 176–186.

(6) Lohse, D.; Zhang, X. Pinning and Gas Oversaturation Imply Stable Single Surface Nanobubbles. *Phys. Rev. E Stat Nonlin Soft Matter Phys.* **2015**, *91*, 031003.

(7) Zhang, X. H.; Khan, A.; Ducker, W. A. A Nanoscale Gas State. *Phys. Rev. Lett.* **2007**, *98*, 136101.

(8) Wu, Z. H.; Chen, H. B.; Dong, Y. M.; Mao, H. L.; Sun, J. L.; Chen, S. F.; Craig, V. S. J.; Hu, J. Cleaning Using Nanobubbles: Defouling by Electrochemical Generation of Bubbles. *J. Colloid Interface Sci.* **2008**, *328*, 10–14.

(9) Yang, S.; Duisterwinkel, A. Removal of Nanoparticles from Plain and Patterned Surfaces Using Nanobubbles. *Langmuir* **2011**, *27*, 11430–11435.

(10) FAN, M.; TAO, D.; HONAKER, R.; LUO, Z. Nanobubble Generation and Its Applications in Froth Flotation (Part II): Fundamental Study and Theoretical Analysis. *Min. Sci. Technol.* **2010**, *20*, 159–177.

(11) Lyu, T.; Wu, S.; Mortimer, R. J. G.; Pan, G. Nanobubble Technology in Environmental Engineering: Revolutionization Potential and Challenges. *Environ. Sci. Technol.* **2019**, *53*, 7175–7176.

(12) Huango, C.; Jiangs, J.; Lu, M.; Sun, L.; Meletis, E. I.; Hao, Y. Capturing Electrochemically Evolved Nanobubbles by Electroless Deposition. A Facile Route to the Synthesis of Hollow Nanoparticles. *Nano Lett.* **2009**, *9*, 4297–4301.

(13) Kang, E.; Min, H. S.; Lee, J.; Han, M. H.; Ahn, H. J.; Yoon, I. C.; Choi, K.; Kim, K.; Park, K.; Kwon, I. C. Nanobubbles from Gas-Generating Polymeric Nanoparticles: Ultrasound Imaging of Living Subjects. *Angew. Chem., Int. Ed.* **2010**, *49*, 524–528.

(14) Li, J.; Xi, A.; Qiao, H.; Liu, Z. Ultrasound-Mediated Diagnostic Imaging and Advanced Treatment with Multifunctional Micro/Nanobubbles. *Cancer Lett.* **2020**, *475*, 92–98.

(15) Li, S.; Du, Y.; He, T.; Shen, Y.; Bai, C.; Ning, F.; Hu, X.; Wang, W.; Xi, S.; Zhou, X. Nanobubbles: An Effective Way to Study Gas-Generating Catalysis on a Single Nanoparticle. *J. Am. Chem. Soc.* **2017**, *139*, 14277–14284.

(16) Xu, S.; Yu, X.; Chen, Z.; Zeng, Y.; Guo, L.; Li, L.; Luo, F.; Wang, J.; Qiu, B.; Lin, Z. Real-Time Visualization of the Single-Nanoparticle Electrocatalytic Hydrogen Generation Process and Activity under Dark Field Microscopy. *Anal. Chem.* **2020**, *92*, 9016–9023.

(17) Hammadi, Z.; Morin, R.; Olives, J. Field Nano-Localization of Gas Bubble Production from Water Electrolysis. *Appl. Phys. Lett.* **2013**, *103*, 223106.

(18) Svetovoy, V. B.; Sanders, R. G. P.; Elwenspoek, M. C. Transient Nanobubbles in Short-Time Electrolysis. *J. Phys. Condens. Matter* **2013**, *25*, 184002.

(19) Luo, L.; White, H. S. Electrogeneration of Single Nanobubbles at Sub-50-Nm-Radius Platinum Nanodisk Electrodes. *Langmuir* **2013**, *29*, 11169–11175.

(20) German, S. R.; Chen, Q.; Edwards, M. A.; White, H. S. Electrochemical Measurement of Hydrogen and Nitrogen Nanobubble Lifetimes at Pt Nanoelectrodes. *J. Electrochem. Soc.* **2016**, *163*, H3160–H3166.

(21) Mazloomi, S. K.; Sulaiman, N. Influencing Factors of Water Electrolysis Electrical Efficiency. *Renew. Sustain. Energy Rev.* **2012**, *16*, 4257–4263.

(22) Theodorakis, P. E.; Che, Z. Surface Nanobubbles: Theory, Simulation, and Experiment. A Review. *Adv. Colloid Interface Sci.* **2019**, *272*, 101995.

(23) Shangjiong, Y.; Dammer, S. M.; Bremond, N.; Zandvliet, H. J. W.; Kooij, E. S.; Lohse, D. Characterization of Nanobubbles on Hydrophobic Surfaces in Water. *Langmuir* **2007**, *23*, 7072–7077.

(24) Shin, D.; Park, J. B.; Kim, Y. J.; Kim, S. J.; Kang, J. H.; Lee, B.; Cho, S. P.; Hong, B. H.; Novoselov, K. S. Growth Dynamics and Gas Transport Mechanism of Nanobubbles in Graphene Liquid Cells. *Nat. Commun.* **2015**, *6*, 6068.

(25) Wang, Y.; Chen, J.; Jiang, Y.; Wang, X.; Wang, W. Label-Free Optical Imaging of the Dynamic Stick−Slip and Migration of Single Sub-100-Nm Surface Nanobubbles: A Superlocalization Approach. *Anal. Chem* **2019**, *91*, 4665−4671.

(26) Chan, C. U.; Ohl, C. D. Total-Internal-Reflection-Fluorescence Microscopy for the Study of Nanobubble Dynamics. *Phys. Rev. Lett.* **2012**, *109*, 174501.

(27) Su, H.; Fang, Y.; Chen, F.; Wang, W. Monitoring the Dynamic Photocatalytic Activity of Single CdS Nanoparticles by Lighting up H2 Nanobubbles with Fluorescent Dyes. *Chem. Sci.* **2018**, *9*, 1448–1453.

(28) Chen, Q.; Luo, L.; Faraji, H.; Feldberg, S. W.; White, H. S. Electrochemical Measurements of Single H2 Nanobubble Nucleation and Stability at Pt Nanoelectrodes. *J. Phys. Chem. Lett.* **2014**, *5*, 3539–3544.

(29) Sundaresan, V.; Monaghan, J. W.; Willets, K. A. Visualizing the Effect of Partial Oxide Formation on Single Silver Nanoparticle Electrodissolution. *J. Phys. Chem. C* **2018**, *122*, 3138–3145.

(30) Hao, R.; Fan, Y.; Zhang, B. Imaging Dynamic Collision and Oxidation of Single Silver Nanoparticles at the Electrode/Solution Interface. *J. Am. Chem. Soc.* **2017**, *139*, 12274−12282.

(31) Hao, R.; Fan, Y.; Howard, M. D.; Vaughan, J. C.; Zhang, B. Imaging Nanobubble Nucleation and Hydrogen Spillover during Electrocatalytic Water Splitting. *Proc. Natl. Acad. Sci. U. S. A.* **2018**, *115*, 5878–5883.

(32) Hao, R.; Fan, Y.; Anderson, T. J.; Zhang, B. Imaging Single Nanobubbles of H2 and O2 during the Overall Water Electrolysis with Single-Molecule Fluorescence Microscopy. *Anal. Chem.* **2020**, *92*, 3682–3688.

(33) Ducker, W. A. Contact Angle and Stability of Interfacial Nanobubbles. *Langmuir* **2009**, *25*, 8907–8910.

(34) Suvira, M.; Zhang, B. Effect of Surfactant on Electrochemically Generated Surface Nanobubbles. *Anal. Chem.* **2021**, 5170–5176.

(35) Hayeck, N.; Tinel, L.; George, C.; Bru, M. Interfacial Photochemistry 14 ´. *Phys. Chem. Gas-Liquid Interfaces* **2021**, 435–458.

(36) Greenspan, P.; Fowler, S. D. Spectrofluorometric Studies of the Lipid Probe, Nile Red. *J. Lipid Res.* **1985**, *26*, 781–789.

(37) Deye, J. F.; Berger, T. A.; Anderson, A. G. Nile Red as a Solvatochromic Dye for Measuring Solvent Strength in Normal Liquids and Mixtures of Normal Liquids with Supercritical and Near Critical Fluids. *Anal. Chem.* **1990**, *62*, 1552.

(38) Ovesný, M.; Křížek, P.; Borkovec, J.; Švindrych, Z.; Hagen, G. M. ThunderSTORM: A Comprehensive ImageJ Plug-in for PALM and STORM Data Analysis and Super-Resolution Imaging. *Bioinformatics* **2014**, *30*, 2389–2390.

(39) Bates, M.; Huang, B.; Dempsey, G. T.; Zhuang, X. Multicolor Super-Resolution Imaging with Photo-Switchable Fluorescent Probes. *Science (80-.).* **2007**, *317*, 1749–1753.

(40) Dutta, A. K.; Kamada, K.; Ohta, K. Spectroscopic Studies of Nile Red in Organic Solvents and Polymers. *J. Photochem. Photobiol. A Chem.* **1995**, *93*, 57–64.

(41) Ray, A.; Das, S.; Chattopadhyay, N. Aggregation of Nile Red in Water: Prevention through Encapsulation in β-Cyclodextrin. *ACS Omega* **2019**.

(42) Tan, B. H.; An, H.; Ohl, C. D. Resolving the Pinning Force of Nanobubbles with Optical Microscopy. *Phys. Rev. Lett.* **2017**, *118*, 054501.

(43) Ishida, N.; Inoue, T.; Miyahara, M.; Higashitani, K. Nano Bubbles on a Hydrophobic Surface in Water Observed by Tapping-Mode Atomic Force Microscopy. *Langmuir* **2000**, *16*, 6377–6380.

(44) Zhang, L.; Zhang, Y.; Zhang, X.; Li, Z.; Shen, G.; Ye, M.; Fan, C.; Fang, H.; Hu, J. Electrochemically Controlled Formation and Growth of Hydrogen Nanobubbles. *Langmuir* **2006**, *22*, 8109–8113.

(45) Walczyk, W.; Schönherr, H. Characterization of the Interaction between AFM Tips and Surface Nanobubbles. *Langmuir* **2014**, *30*, 7112–7126.

(46) Walczyk, W.; Schönherr, H. Dimensions and the Profile of Surface Nanobubbles: Tip-Nanobubble Interactions and Nanobubble Deformation in Atomic Force Microscopy. *Langmuir* **2014**, *30*, 11955–11965.

(47) Batchelor-McAuley, C.; Little, C. A.; Sokolov, S. V.; Katelh ön, E.; Zampardi, G.; Compton, R. G. Fluorescence Monitored Voltammetry of Single Attoliter Droplets. *Anal. Chem.* **2016**, *88*, 11213–11221.

(48) Kurniasih, I. N.; Liang, H.; Choudhary Mohr, P.; Khot, G.; Rgen, J.; Rabe, P.; Mohr, A. Nile Red Dye in Aqueous Surfactant and Micellar Solution. *Langmuir* **2015**.

(49) Jordan, A. M. I.; Mitchell, T. M. Machine Learning : Trends , Perspectives , and Prospects Published by : American Association for the Advancement of Science Linked References Are Available on JSTOR for This Article : Digitize , Preserve and Extend Access to Science Machine Learning : Tre. **2015**, *349*, 255–260.

(50) Likas, A.; Vlassis, N.; J. Verbeek, J. The Global K-Means Clustering Algorithm. *Pattern Recognit.* **2003**, *36*, 451–461.

(51) Chong, B. K-Means Clustering Algorithm : A Brief Review. *4*, 37–40.

(52) Thorndike, R. L. Who Belongs in the Family? *Psychometrika* **1953**, *18*, 267–276.

Chapter 4. APPLICATION OF LANGMUIR ISOTHERM ON ADSORPTION OF FLUOROPHORE AT NANOBUBBLE SURFACE

4.1 ABSTRACT

Molecular interaction at the nanoscale gas/liquid interface has yet to be studied in great detail. Here we report the usage of the Langmuir isotherm model to understand the kinetics of fluorophore adsorption and desorption at the nanobubble surface. Three rhodamine B (RB, neutral), rhodamine 6G (R6G, positively charged), and sulforhodamine 6G (SRG, negatively charged) are chosen to explore how charges of fluorophores would affect fluorophore adsorption and desorption at the gas/liquid interface. The Langmuir isotherm adsorption model is applied, where the equilibrium constants are obtained. Rate constants of adsorption and desorption are also determined from single-fluorophore residence times. We found that fluorophore adsorption is an exothermic and spontaneous reaction. And the driven mechanism is also discussed.

4.2 INTRODUCTION

Interfacial chemistry represents a unique environment with properties distinct from the bulk. It has been widely studied in biology,[1] ocean,[2] atmosphere,[3,4] electrochemistry,[5–8] catalysis [9] and other fields.[10] Especially, aqueous interface, such as air/water and electrode/liquid, are essential to the fundamental understanding to the remained debating topics, including but not limited to: (i) protein stability with ionic solution, also known as Hofmeister series;[11] (ii) ametropic organic molecules involvement at ocean surfaces;[12] (iii) catalytic activity, corrosion, electrolysis, at the solution/electrode interface.[13–15]

There are only few techniques that can probe the aqueous interface down to molecular level, including photoelectron spectroscopy,[16] neutron reflectivity,[17] vibrational sum-frequency generation with infrared (IR), [18–22] etc. Especially, the nonlinear optical technique stands out in this field. The Saykally group used resonant UV second harmonic generation spectroscopy, combined with computations, to study the adsorption mechanism of thiocyanate ions at the air/water interface.[23–25] The Richmond group utilized vibrational sum frequency spectroscopy to study different small organic molecules at the air/water interface to reveal molecular level information related to atmospheric aerosols study.[4,26] Nonlinear optical technique requires the sample to have a certain surface area so that light can illuminate. It hence mainly measures the ensemble average behavior of the interface, limiting its ability to study a single entity individually.

To better study single entities at the interface, single-molecule fluorescence microscopy is developed, which provides a platform to enable single entity detection.[27] Harries and coworkers studied interfacial DNA hybridization kinetics at selective capture surfaces[28,29] and measured the binding rates of protein at a phospholipid bilayer via fluorescence microscopy.[30] Our group utilized total internal reflection microscopy (TRIFM) to study single redox events at a modified ITO surface, where the adsorption, desorption, and redox dynamics were studied in detail.[7] Later, we successfully imaged the electrochemically generated surface nanobubbles via single fluorophore labeling.[5] This approach creates a unique three-phase, gas, liquid and solid, environment in nanoscale, allowing one to study different interfaces simultaneously.

To address the individual molecular interaction at surface nanobubbles and to reveal the detailed mechanistic properties, we here report the usage of the Langmuir isotherm adsorption model to elucidate the interfacial dynamics of rhodamine dyes adsorption at a nanoscale gas/liquid interface. Three rhodamine dyes with different charges, rhodamine B (RB, neutral), rhodamine 6G

(R6G, positively charged), and sulforhodamine 6G (SRG, negatively charged) are chosen. Each nanobubble is a nanoscale gas/liquid interface, and we can resolve individual fluorophores' adsorption and provide direct mechanistic insights. Through the Langmuir adsorption model, adsorption equilibrium constants, adsorption, and desorption constants are determined. We found that SRG has the greatest equilibrium constant. A negative value of free energy and enthalpy indicates that fluorophore adsorption at the gas/liquid interface is spontaneous and exothermic. In this work, we develop an innovative approach to probe gas/liquid nano-interface using TIRFM that can reveal detailed mechanistic characterizations from individual adsorbed entities.

4.3 Experimental Section

4.3.1 *Chemicals and Materials.*

All of the following chemicals and materials were used as received from the manufacturers: Rhodamine 6G perchlorate (R6G) (Kodak, laser grade), sulforhodamine G (SRG) (Aldrich Chemical Co.; dye content ~60%), Rhodamine B (RB), sodium sulfate (Na_2SO_4; J. T. Baker, 101.8%), and ITO-coated microscope coverslips (SPI Supplies, sheet resistance 15– 30 Ω/square). Deionized water (>18 MΩ·cm) was obtained through a Barnstead Nanopure water purification system and used for all aqueous solutions.

4.3.2 *Single-Molecule TIRF Microscopy.*

Single-molecule TIRF imaging experiments were performed on a home-built Olympus IX70 inverted microscope. An Olympus Apo N 60× 1.49 NA objective(with an external 1.5x magnification on the microscope) and a 532-nm green laser (CrystaLaser) source were used. With a constant 10 mW (2.5 kW/cm^2) excitation illumination, the fluorescence images were filtered with an ET590/50m emission filter (Chroma Technology Co.) and collected on an EMCCD (iXon

Ultra 897, Andor) cooled to -85C. Images were recorded at 0.05s exposure time (frame rate: 19.81Hz) and with an amplifier gain of 300. A thin polydimethylsiloxane (PDMS) film with a 2-mm–diameter hole was placed on the surface of the ITO. 6uL of dye solution was placed in the hole and a Pt wire was placed in the solution as a reference electrode (RE). The voltage was generated by a 273A potentiostat (Princeton Applied Research) and applied across the working electrode (ITO) with respect to the Pt RE.

For the temperature dependency study, the sample was mounted on a Dual Channel Temperature Controller (TC-344C, Warner Instrument). Five temperatures were set: 24°C, 30°C, 33°C, 36°C, and 39°C. Real-time temperatures were measured using an infrared thermometer(Mastercool Inc). Variations were tabulated in Table S 4.2.

4.3.3 *Image Analysis and Counting Single Molecules.*

Single-molecule fluorescence images/videos were analyzed using the ThunderSTORM plug-in in ImageJ. Each fluorescent single molecular spot is described by a point spread function (PSF), which is fitted with a two-dimensional (2-D) Gaussian function to localize the center position. The total number of fluorescent spots was counted as the number of detections. The number of detections was plotted versus fluorophore concentration. Regression analysis was used to fit an experimental curve to the Langmuir equation (eq 2), and the equilibrium constants were determined. Error bars are reported as standard error of three measurements.

4.3.4 *Single-Molecule Tracking.*

Tracking of fluorescent puncta was performed using TrackMate plug-in in ImageJ. Briefly, fluorescent puncta were detected above a user-set threshold using the Laplacian of the Gaussian (LoG) as a blob detector. Puncta were tracked and linked to other puncta within three frames within

300nm displacement. The number of frames for one trajectory was converted to duration times using a frame rate 19.81Hz.

4.4 Results and Discussion

We adopted our previously developed nanobubble generation system **(**Figure 4.1A)[5]. Briefly, a fluorophore solution is placed on the top of an ITO electrode in TIRFM. Hydrogen nanobubbles were electrochemically generated upon water reduction at potentials more negative than -0.75V vs. Pt QRE. Dye molecules are transiently adsorbed at the nanobubble surface and enable the detections of nanobubble. In this work, three water-soluble rhodamine dyes R6G, RB, and SRG are chosen for a comparison study (Figure 4.1B). They have similar excitation and emission range and feature a similar hydrophobic rhodamine core structure (conjugated ring structures) but with different head groups and charges, where RB is neutral, R6G is positively charged, and SRG is negatively charged.

To specifically focus on studying the molecular interactions at bubble interface, in this work, constant potentials, -0.8V, -0.9V, -1.0V, -1.1V, and -1.2V, are applied to obtain relatively stable nanobubbles. At 0V, water is not reduced. Solutions with dye contents have dark background due to the fast diffusion of fluorescent molecules in and out of the evanescent field, as shown in Figure S 4.1. Figure S 4.1B shows three TIRF images of 10nM RB, 5nM R6G, and 0.5nM SRG with 1M Na_2SO_4 at constant -1.0V vs. Pt QRE. When applying a constant potential that is negative enough to reduce water, hydrogen nanobubbles are generated and are labeled by a single fluorophore, allowing for nanobubble detection and counting. The similar labeling behaviors of RB and SRG validate the usage of these three rhodamine dyes in this experiment. Three fluorescent puncta of each condition are randomly selected, and their corresponding fluorescence intensity-time traces are plotted in Figure S 4.1B (More trace analysis in Figure S

4.2). The single-step abrupt increase in intensity followed by a rapid decrease to the baseline demonstrates nanobubble labeling using RB, R6G and SRG is from single-molecule adsorption. It is noticed that some fluorescent-time traces have a near constant intensity for a subsecond period after the abrupt intensity increase, such as RB cases, these near constant intensity ranges are defined as the duration time of fluorophores resident at nanobubble surface, which will be further discussed in a later section.

4.4.1 *Langmuir Model Assumptions.*

There are four assumptions for the application of the Langmuir model: 1. Each nanobubble surface is the same for single fluorophores adsorption; 2. No interaction between dye molecules and nanobubbles; 3. Each adsorption event is independent; 4. Dye adsorption is a monolayer. First, nanobubble generation is stochastic, either in size or shape. However, under a constant potential, surface nanobubbles are believed to be dynamically stable because of the following reasons: 1. Equilibrium between gas influx and outflux;[31,32] 2. Contamination layer;[33] 3. Three-phase pinning line;[34] etc. We also observed the high stability and long-lived properties of surface nanobubbles. Hence, we believe that each nanobubble has the same probability to be labeled under the same conditions. Second, hydrogen nanobubbles are chemically inert to rhodamine dyes, so dye molecules are only transiently and physically adsorbed then leave the bubble surface. These adsorption/desorption processes are expected to be very similar for individual dye and bubbles. Third, fluorophore adsorption at a bubble surface is not likely to be affected by neighbored bubble labeling events, thus all events are independent. Lastly, we have found that around 97% of the events are single-molecule labeling events, indicated by a single-step sudden increase in fluorescent intensity, followed by a steady intensity for a sub-second period, and finally, a quick decay to the baseline.[5] This also agrees with what we observed in this study (Figure 4.1B). It

suggests that molecule-molecule repulsion might prevent additional fluorophore adsorption. Therefore, single-molecule adsorption allows us to apply the Langmuir isotherm adsorption model at this gas/liquid nano-interface. And the equilibrium constants, adsorption/desorption rate constants of fluorophores could be determined.

4.4.2 *Application of Langmuir model for fluorophores adsorption at bubble surface.*

To study the single-molecule adsorption/desorption at the bubble surface, we hence derive a more appropriate Langmuir equation to describe our system from the original Langmuir single-site adsorption equation. It is a simple two-step kinetic model of fluorophores at the gas/liquid interface: the freely diffusing fluorophores and trapped fluorophores at the nanobubble surface. Fluorophores in bulk solutions are diffusing too rapidly to be detected until they are transiently adsorbed at the nanobubble surface then leave. Due to the quenching ability between ITO and fluorophores, detection of adsorbed fluorophores at the ITO surface is negligible. The abrupt increase and decrease of fluorescent intensity represent the stay/leave process of fluorophores at the nanobubble surface. These can be interpreted as adsorption/desorption, and their rates are adsorption/desorption constant, k_a and k_d respectively. The equilibrium constant of this process thus is defined in Eq 4.1,

$$K = \frac{k_a}{k_d} \qquad \text{Eq 4.1}$$

Hydrogen nanobubbles are generated stochastically at an ITO electrode at reduction potential. These dynamically stable nanobubbles are visually detected and possibly counted upon fluorophore adsorption. In other words, the number of detections can be expressed as the number of nanobubbles that are labeled in one frame. It is worth noticing that the counted numbers of nanobubbles do not represent the total number of nanobubbles generated at the surface due to the

dynamic labeling process. Derived from the original Langmuir equation[20], an equilibrium between the number of labeled nanobubbles and fluorophore concentration can be depicted using Eq 4.2,

$$\gamma^* = \frac{\gamma K[F]}{1+K[F]} \qquad \text{Eq 4.2}$$

where γ^* is the number of detections/nanobubbles, γ is the estimated number of available nanobubbles, K is the equilibrium constant, and $[F]$ is the concentration of fluorophore. At low fluorophore concentration, $[F] \ll K^{-1}$, Eq 4.2 simplifies to a linear relationship

$$\gamma^* \approx \gamma K[F] \qquad \text{Eq 4.3}$$

where the number of nanobubbles is linear with the concentration of fluorophore, with a sensitivity that depends on the number of available nanobubbles γ.

Experiments were performed under five reduction potentials -0.8V, -0.9V, -1.0V, -1.1V and -1.2V. All potentials are negative enough to reduce water and generate H_2 nanobubbles. The concentration of fluorophores is increased accordingly to approach labeling equilibrium. However, concentrations cannot be too high due to the limiting quenching ability of ITO as well as the resolution limit of single-molecule counting. In Figure 4.2, equilibrium curves at various potentials are displayed. Data points with error bars in the y-axis are standard errors from three repetitive experiments. The dash curves are fitted Langmuir curve using Eq 4.2. As we discussed above, at a low concentration region, a linear relationship between the number of nanobubbles and fluorophore concentration is observed, agreeing with the Langmuir approximation. The curves gradually level off as concentrations of fluorophore increase, approaching the equilibrium state (Eq 4.3). Among these three dyes, it is obvious both R6G and RB equilibrated at higher concentration of fluorophores than SRG, and thus SRG is the most effective fluorophore in labeling nanobubbles. Equilibrium constants are plotted for a more direct comparison (Figure 4.2). SRG has the absolute greatest equilibrium constant, suggesting that there are more adsorbed SRG

molecules than freely diffusing SRG in the bulk solution, compared to RB and R6G. In other words, SRG likes to be at the bubble surface and have more effective collisions, resulting in more detections at a lower concentration. Based on the molecular structures (Figure 4.3), SRG is negatively charged with two sulfonate groups and a neutral and hydrophobic rhodamine core structure in a neutral solution. The easier adsorption of SRG could be attributed to the preferred molecular orientation of SRG at the bubble surface, where the rhodamine core group is landing at the interface. The adsorption process is likely driven by the hydrophobic interaction. On the other hand, both RB and R6G have a charged rhodamine group, making the adsorption process is less favored.

For each fluorophore, the equilibrium constants have no significant difference between voltages (Two-way ANOVA test). In theory, applying more negative potential results in more hydrogen gas production, suggesting more nanobubbles could be nucleated or some of them grow larger. Surface area and surface curvature of nanobubbles with the size of nanobubbles, which could potentially affect fluorophore landing and result in different equilibrium constants. We see that equilibrium constants are not statistically different in all voltages, which suggests that fluorophore adsorption at nanobubble surface might not be affected by the geometry of bubbles, or minor changes in voltages do not result in a large change in bubble geometry. In TIRFM, the excitation light intensity decays exponentially with distance from the electrode surface, resulting in lower fluorescence intensity for fluorophores that are farther away from the surface. With that saying, the larger/higher the bubble is, the weaker the intensity is. From intensity box plots (Figure S 4.2), however, there is no significant difference in various voltages. Moreover, concentrations have no effect on fluorophore adsorption at the nanobubble surface. And concentration and voltages are two independent factors that do not interfere with nanobubble labeling.

4.3.3 Determination of Adsorption and Desorption Rates.

Although equilibrium constants have already shown the dynamics of nanobubbles labeling using different fluorophores, knowledge of fluorophore binding and unbinding rates can provide more insights into the interactions between fluorophores and nanobubbles surfaces. Individual spots from frame to frame in videos can be tracked using TrackMate plug-in in ImageJ. By plotting the single-molecule residence time histogram, the time constant of fluorophores can be estimated by fitting with first-order exponential decay (Eq 4.4).

$$y = y_0 + Ae^{-\frac{t}{\tau}} \qquad \text{Eq 4.4}$$

where y is the number of nanobubbles, y_0 is the offset of the number of nanobubbles, A is the corresponding number of events for time t with the time constant τ. The exponential fits the cumulative residence time histograms, and τ is determined. We refer τ as the duration time constant, representing the time a fluorophore is adsorbed at the bubble surface. An example of duration time distributions with single-exponential decay fit is shown in Figure 4.3A. A summary of the duration time constant for each fluorophore is plotted in Figure 4.3B, where the error bars represent the standard errors of three repetitive experiments. In Figure 4.3B, we see that SRG has the shortest duration time constant, which could be due to the electrostatic repulsion between negatively charged SRG and bubble surface. Both RB and R6G have a longer duration time than SRG. As we discussed before, fluorophores are likely to have a preferred molecular orientation when adsorbed. Once molecules are adsorbed, electrostatic interactions play a more significant role because molecules can “feel” the negative charge of the bubble. In this case, the desorption process would be mainly driven by the electrostatic interaction between fluorophores and the bubble surface. Rhodamine cores of R6G and RB are positively charged, so once they are

absorbed, the electrostatic attraction would hold the molecules tighter and result in a longer duration time. Nevertheless, the electrostatic repulsion between the negatively charged SRG and negatively charged bubble surface would repel SRG from the interface, leading to a shorter duration time. Also, there is no obvious trend observed between τ and applied potentials for each fluorophore respectively, implying that bubble size might not have a significant impact on τ.

Desorption rate constant k_d can be determined using Eq 4.5: [28]

$$k_d = \frac{1}{\tau} \qquad \text{Eq 4.5}$$

And combined with eq 4.1, adsorption rate constant k_a can be determined using Eq 4.6:

$$k_a = k_d * K \qquad \text{Eq 4.6}$$

It should be noticed that adsorption/desorption rates of fluorophores are derived from the duration time, which could be affected by photobleaching and photoblinking because these processes also result in the disappearance of a fluorescent spot. As observed and reported, rhodamine dyes have a much longer lifetime than residence time, which therefore should have negligible effect in determining τ. The impact of photoblinking can be reduced by bridging neighboring frames with returning fluorescence at the same spot, which could be done in TrackMate plug-in in ImageJ. Adsorption/desorption rates of RRB, R6G, and SRG at different potentials are calculated and are plotted in Figure 4.3 C and D. Desorption rate constant is the reciprocal of τ, so SRG has the greatest k_d, indicating very fast desorption of SRG at the bubble surface because of electrostatic repulsion. Also, we found that SRG has the greatest adsorption rate constant among rhodamine dyes (Figure 4.3D). This fast reaction of adsorption is attributed to the hydrophobic interaction between the neutral rhodamine cores and the hydrophobic bubble surface.

4.4.3 *Thermodynamics of Dye Molecules Adsorption.*

To further explore the interaction between fluorophores at nanobubble surfaces, we performed the experiments under different temperatures, so that thermodynamic properties of fluorophore adsorption can be determined. For each dye molecules adsorption at the bubble surface, five temperatures are set, 24°C, 30°C, 33°C, 36°C, and 39°C respectively, and -1.0V constant potential is applied for all measurements. Temperature variations are tabulated in Table S 4.1. We believe that temperatures could potentially affect bubble nucleation, generation, and fluorophore adsorption. Firstly, we want to understand how equilibrium constants change with various temperatures.

Figure S 4.5 displays three Langmuir model fittings of RB, R6G, and SRG at five temperatures under -1 V constant potential. The equilibrium constant (K) is determined and tabulated in Table S 4.2. We found that the equilibrium constants decrease with increased temperatures, meaning adsorption is exothermic. This is confirmed by plotting the logarithm of the equilibrium constant, K, versus reciprocal of temperature, 1/T. The resulting straight line will have a slope equal to $\Delta H^{\circ}/R$ and an intercept equals to $\Delta S^{\circ}/R$, where ΔH and ΔS can be extracted (Figure S 4.6). The negative values of ΔH again indicate dye molecules' adsorption is exothermic, meaning that the heat is released to its surrounding environment during the adsorption process. A higher temperature would impede this process, resulting in a decrease in the equilibrium constants. And the values of ΔH are comparable to reported values of adsorption thiocyanate ions to the liquid water surface.[14] The ΔS of adsorption refers to the change of randomness at the gas/water interface. When molecules get adsorbed to the surface, the freedom of movement of itself becomes restricted, resulting in a decreased entropy (negative ΔS). It might seem to contradict the Second Law of Thermodynamics which states that the entropy change of the universe usually is positive.

It still holds for the adsorption process because the entropy of the system does decrease but is compensated by a greater increase in the entropy of the surroundings. In this study, both RB and R6G have negative ΔS due to the adsorption process, as expected. Interestingly, SRG has a positive ΔS, indicating that SRG adsorption creates a more disordered system. It is possible that when SRG gets adsorbed at the interface, solvated water molecules are replaced by gas molecules, resulting in gaining more translational entropy than is lost by adsorbed dye molecules. An increased degree of randomness of sorbate at the gas/water interface suggests a more thermodynamically favorable condition for SRG adsorption, in agreement with the greatest equilibrium constant. Moreover, Gibbs free energy can be obtained by $\Delta G = \Delta H - T\Delta S$. We can see that the adsorption process is spontaneous because of the negative values of Gibbs free energy(Table S 4.3).[35]

Time constants τ are determined using the aforementioned method[30,32] and plotted in Figure S 4.7. There are large variations on τ, which could be due to the heterogeneity of ITO electrode that results in heterogeneous bubble formation or geometry. Desorption and adsorption rate constants can also be calculated and are plotted in Figure S 4.8**.** From Arrhenius plots, we can obtain rate constants for three rhodamine dyes at different concentrations (Figure S 4.9, Figure S 4.10 and Figure S 4.11**)**. It is noticeable that desorption rates do not have a consistent trend as a function of temperature, but we observe that adsorption rates decrease as temperature elevates for all three conditions. Moreover, we can use Arrhenius expression $k = Ae^{\frac{-E_a}{RT}}$ to obtain activation energy for adsorption and desorption (Figure S 4.12). We can see that the activation energy for adsorption is negative across three fluorophores, possibly implying that adsorption rate would decrease by increasing temperature. At higher temperatures, the solubility of dye molecules increased, suggesting that interaction forces between solvents and solutes could be stronger than the forces between dye molecules and bubble surface. Therefore, dye molecules are less likely to

be adsorbed, resulting in decreased rates at a higher temperature. More comprehensive work needs to be done to further address this observation.

4.5 CONCLUSIONS

In sum, this is the first report of using the Langmuir adsorption model to investigate dye molecules adsorption at a nanoscale gas/liquid interface. By utilizing single-molecule fluorescence microscopy, we can resolve individual nanobubble labeling behavior. Fluorophore labeling is a two-step physical adsorption. By employing the Langmuir model, we could determine adsorption equilibrium constants, rate constants of adsorption, and desorption. We found that both hydrophobic and electrostatic interaction between fluorophores and bubble surfaces would contribute to fluorophore adsorption and desorption. Moreover, voltage and concentration of dye have negligible contributions to fluorophore labeling at the bubble surface. We then experimented with different temperatures, where thermodynamic properties can be extracted. We discovered that fluorophore adsorption at the bubble surface is spontaneous and exothermic, suggested by the negative values of ΔG and ΔH. We understand that a more comprehensive study is needed to fully understand the molecular interaction at this nanoscale gas/liquid interface. The ability to study molecular adsorption individually at a nanoscale interface is revolutionary in the interfacial study. We believe this pioneering work would provide a fundamental technique for future applications in nanoscale interfacial study.

4.6 FIGURES

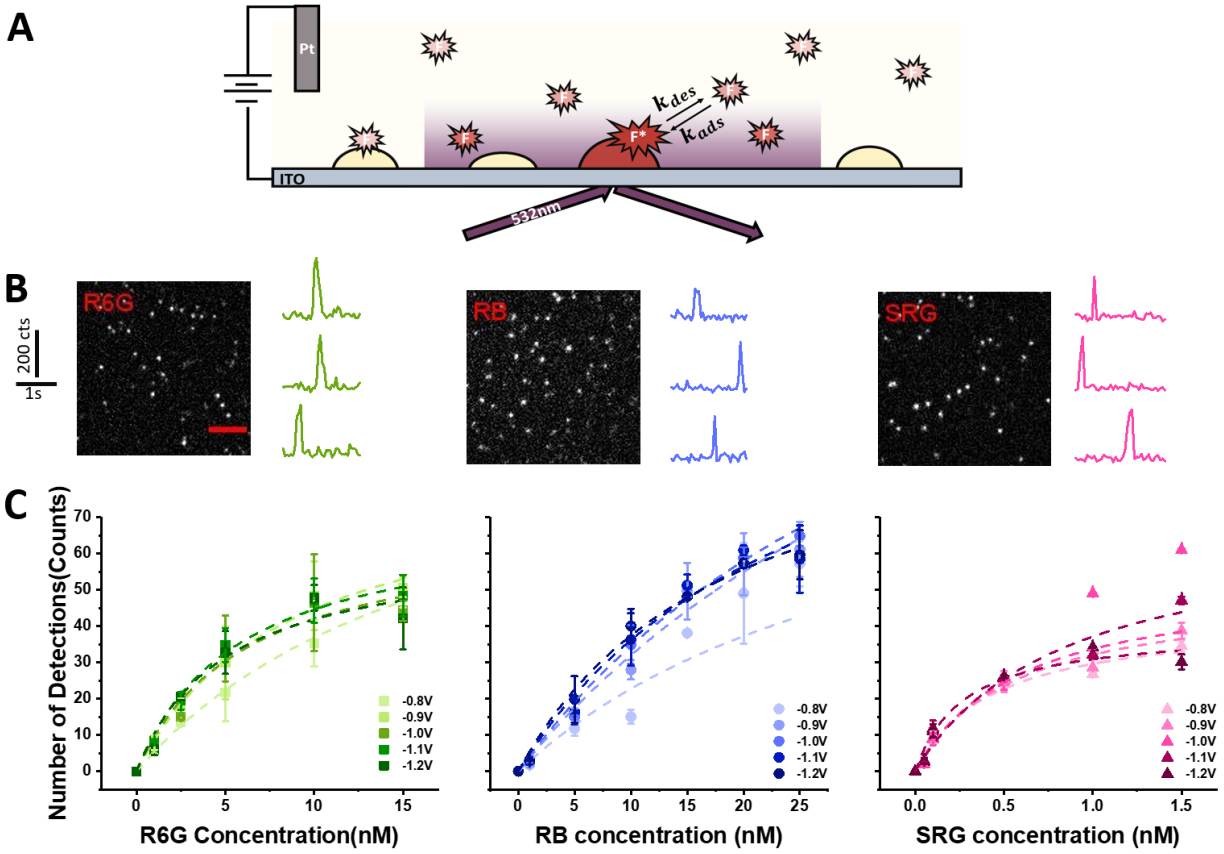

Figure 4.1 Single fluorophore adsorption of rhodamine dyes and the application of Langmuir isotherm model.

A) A scheme of the experimental setup used for imaging electrochemically generated H 2 nanobubbles. F represents fluorophores, which are used to label nanobubbles that are imaged by TIRF microscopy. B). A series of TIRF images of a 22.8 × 22.8-μm^2 area on an ITO electrode taken from a constant -1.0V potential versus Pt QRE in water containing 1 M Na_2SO_4 and 10 nM RB, 5nM R6G and 0.5nM SRG respectively. Fluorescence images were recorded at 19.81 frames per second with a 50-ms exposure time. (Scale bar, 5 μm). Fluorescence intensity−time traces showing three randomly selected nanobubbles detected at -1 V constant potential are shown to the right of TIRF images. Traces were obtained by averaging the total intensity of a 6 × 6 pixel area around the center spot. (Scale bar, 200 fluorescence counts and 1 s.) C). Langmuir adsorption isotherm model fitting for RB, R6G and RB at five potential conditions. Color from light to dark represents an increase in voltage, step size -0.1V. Dash lines represent the Langmuir adsorption fitting curve using Eq 4.2. Error bars in y-axis in data points are standard error from three repetitive measurements.

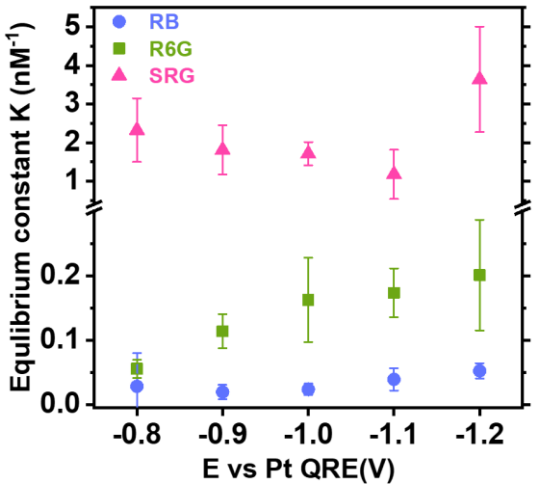

Figure 4.2 Equilibrium constants for RB, R6G and SRG at five different applied potentials. Error bars in y directions are standard errors from three repetitive experiments.

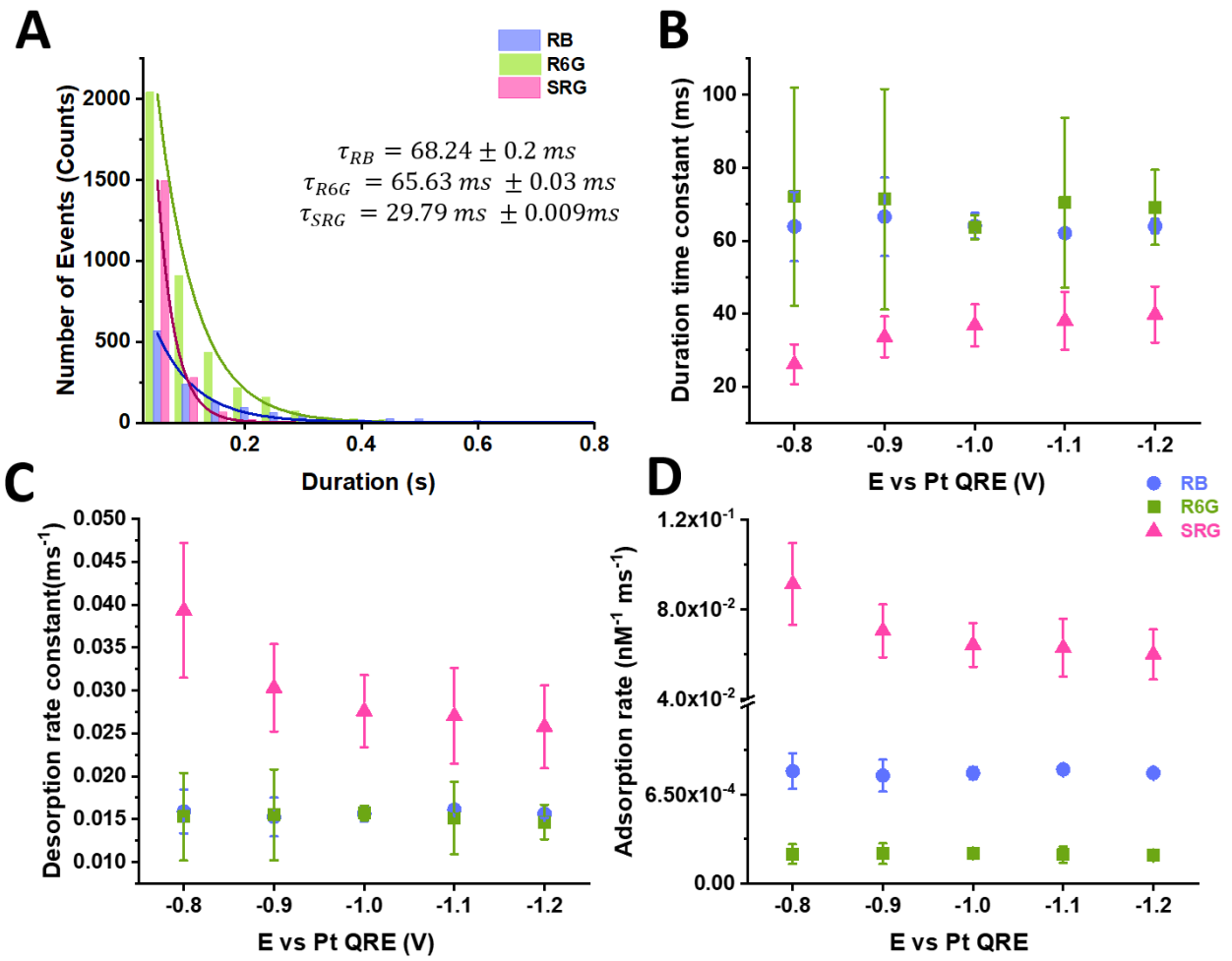

Figure 4.3 Residence time of fluorophores.

(A)An example histogram of the duration of nanobubble detection events. Nanobubble events are collected under a constant -1 V applied potential (vs Pt QRE) in electrolyte solutions containing 5 nM R6G, 5 nM RB, and 0.05 nM SRG with 1M Na_2SO_4. Solid lines are the single-exponential decay fits with time constants of 68.24 ± 0.2 ms, 65.63 ± 0.03 ms, and 29.79 ± 0.009 ms. (B) Scatter plot of fluorophore duration time (ms) under different constant potentials, -0.8 V, -0.9 V, -1.0 V, -1.1 V and -1.2 V. Rate constants of desorption (C) and adsorption (D) for R6G, RB, and SRG. Error bars in y directions are standard errors from three repetitive experiments.

4.7 Supporting Information

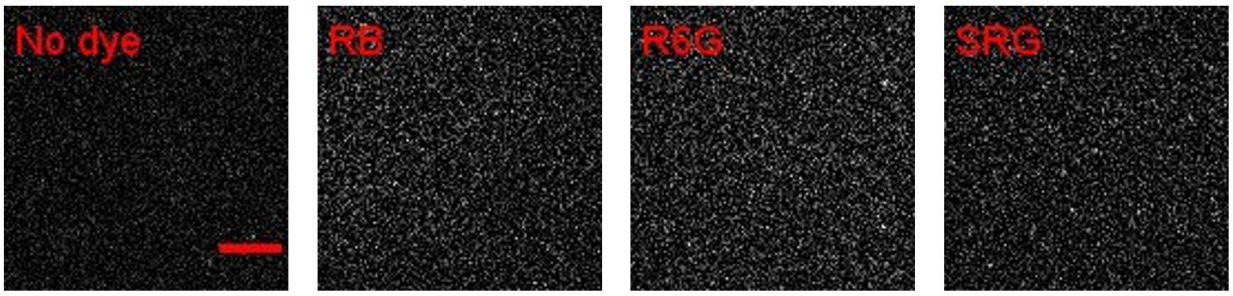

Figure S 4.1 TIRF images of control experiments.

A series of TIRF images of a 22.8 × 22.8-μm^2 area on an ITO electrode taken from a constant 0V potential versus Pt QRE in water containing 1 M Na_2SO_4 and no dye, 10 nM RB, 5nM R6G and 0.5nM SRG respectively. Fluorescence images were recorded at 19.81 frames per second with a 50-ms exposure time. (Scale bar, 5 μm.) Images were adjusted at the same brightness and contrast level.

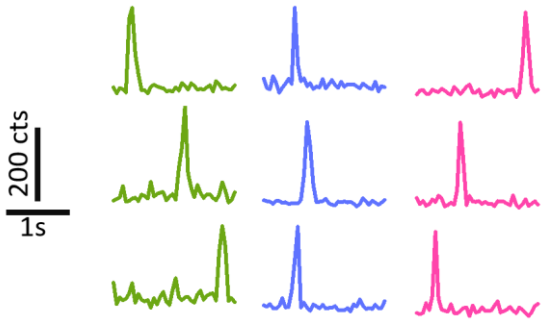

Figure S 4.2 Additional fluorescence and time traces for R6G, RB and SRG.

Fluorescence intensity−time traces showing three randomly selected fluorophore labeling at -1 V constant potential in a water solution containing 5 nM R6G(green), 5nM RB(blue), 0.5nM SRG(pink)and 1 M Na_2SO_4. Traces were obtained from videos recorded at 19.81 frames per second with a 50-ms exposure time, by averaging the total intensity of a 6 × 6 pixel area around the center spot. (Scale bars, 200fluorescence counts and 1s.)

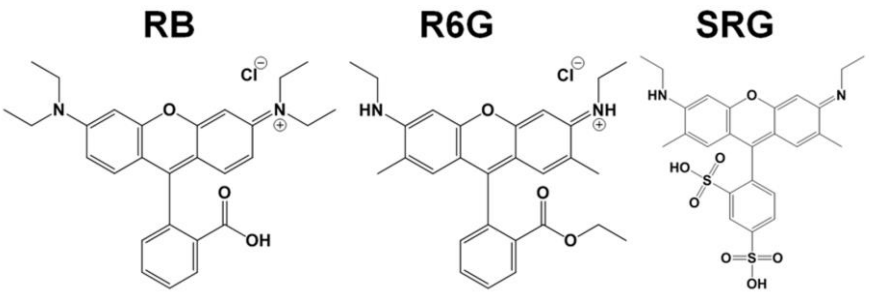

Figure S 4.3 Molecular Structure of RB, R6G and SRG

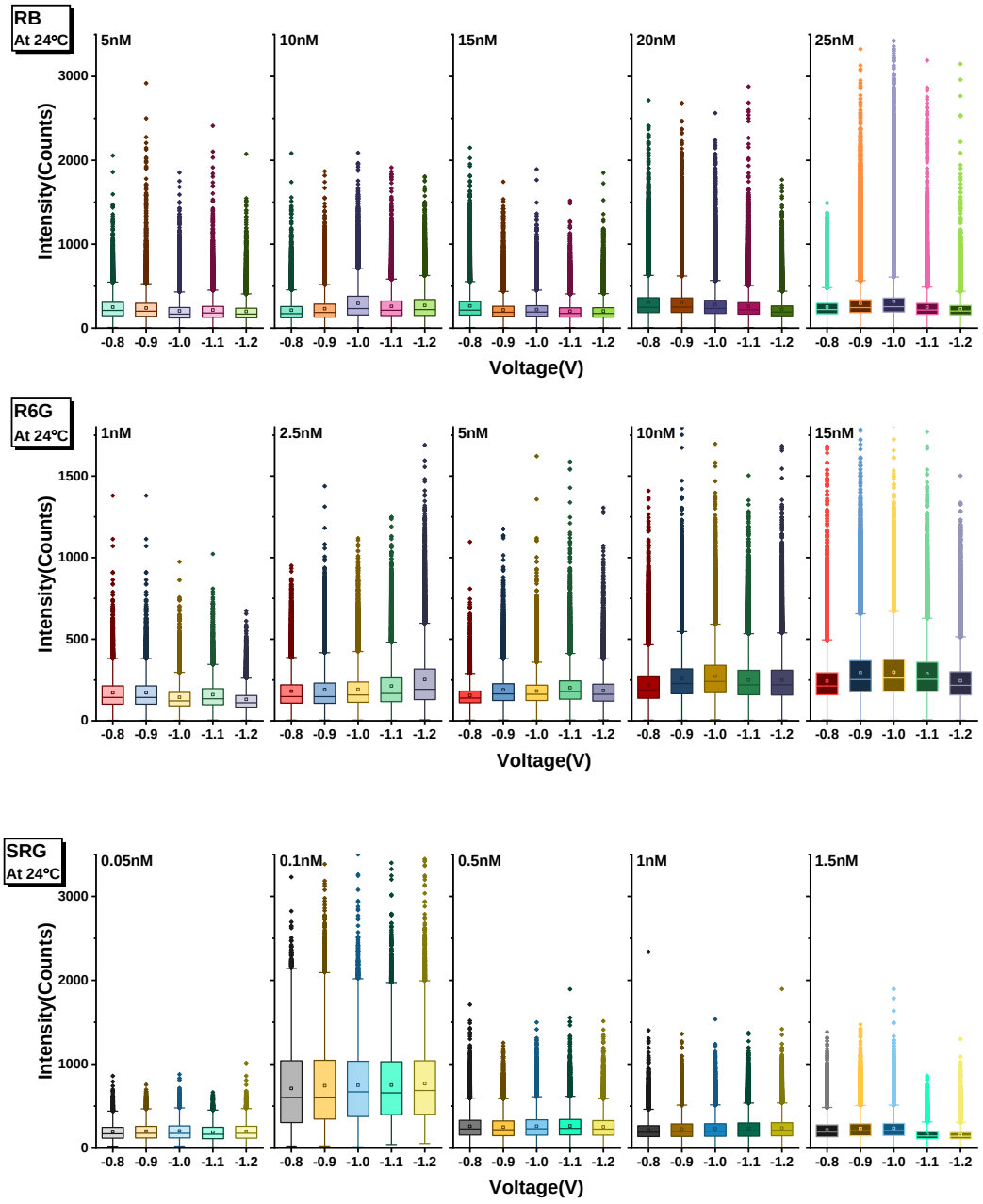

Figure S 4.4 Intensity Comparisons for RB, R6G, and SRG at various constant potentials. Box plots for intensity variation as a function of voltage for RB, R6G and SRG respectively.

Table S 4.1 Temperature variations.

Actual temperatures measured by infrared thermometer. Standard deviations from at least three measurements.

Set temperature (°C)	**Actual temperature(°C) (standard deviation)**
24	24.60 (0.00)
30	30.18 (0.88)
33	33.31 (0.62)
36	36.57 (0.35)
39	40.63 (0.57)

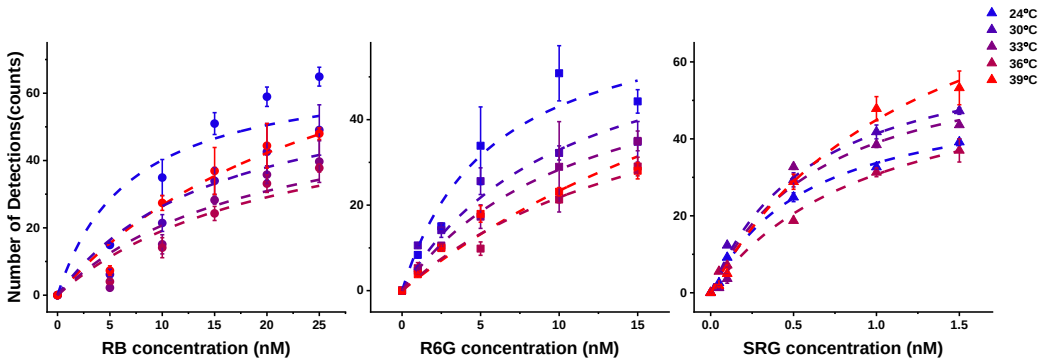

Figure S 4.5 Langmuir Model at various temperature

Five temperatures are set: 24°C, 30°C, 33°C, 36°C, and 39°C. Actual temperatures were measured and tabulated in Table S 4.1. Bubbles are generated at -1.0V constant potential. Symbol circle, square, and triangle represent RB, R6G and SRG respectively. Dotted lines are fitted Langmuir equation, and the extracted equilibrium constants are tabulated in Table S 4.2. Error bars on y-axis are standard deviations from three measurements.

Table S 4.2 Equilibrium constant K at various constant potential for RB, R6G and SRG. Equilibrium constants from Langmuir equation Eq 4.2 at different temperatures.

Set temperature(°C)	*RB K(nM^{-1})*	*R6G K(nM^{-1})*	*SRG K(nM^{-1})*
24	0.14 ± 0.041	0.17 ± 0.031	1.70 ± 1.68
30	0.06 ± 0.012	0.10 ± 0.013	1.64 ± 0.47
33	0.05 ± 0.010	0.09 ± 0.0025	1.54 ± 0.75
36	0.05 ± 0.0075	0.06 ± 0.0049	1.02 ± 0.32
39	0.04 ± 0.0029	0.03 ± 0.0029	0.80 ± 0.25

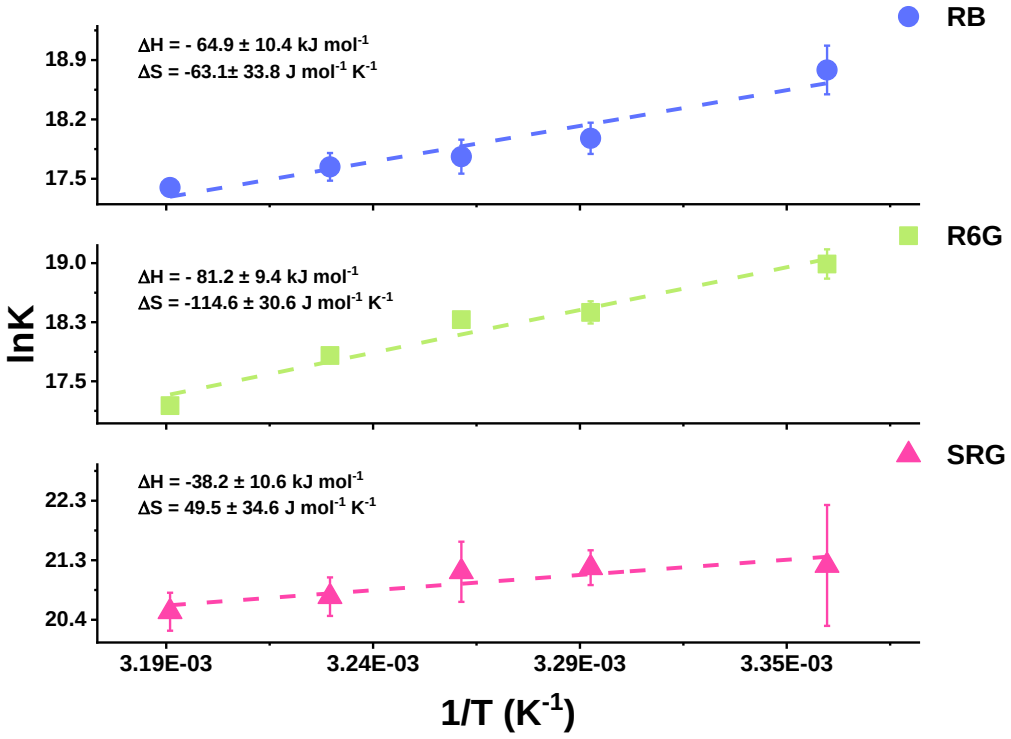

Figure S 4.6 Determination of adsorption enthalpy and entropy of dye molecules at bubble surface.

Linear fit of natural log of the adsorption equilibrium constant versus the reciprocal temperature for three dyes respectively. Actual temperatures are used (Table S 4.1), and x-axis error of temperature are neglected in plots.

Table S 4.3 Gibbs free energy G at various constant potential for RB, R6G and SRG.

Calculated free energy using $\Delta G = -RTlnK$. Actual temperature is used, and the unit of equilibrium constant K is converted from nM^{-1} to M^{-1} for calculation.

Set temperature(°C)	*RB ΔG (kJ mol^{-1})*	*R6G ΔG (kJ mol^{-1})*	*SRG ΔG (kJ mol^{-1})*
24	-46.50 ± 13.34	-47.96 ± 8.51	-52.62 ± 51.81
30	-45.34 ± 8.34	-46.33 ± 6.33	-53.51 ± 15.17
33	-45.25 ± 9.07	-46.58 ± 1.34	-53.89 ± 26.44
36	-45.43 ± 7.40	-45.93 ± 4.03	-53.42 ± 16.76
39	-45.38 ± 3.60	-44.92 ± 4.26	-53.48 ± 16.57

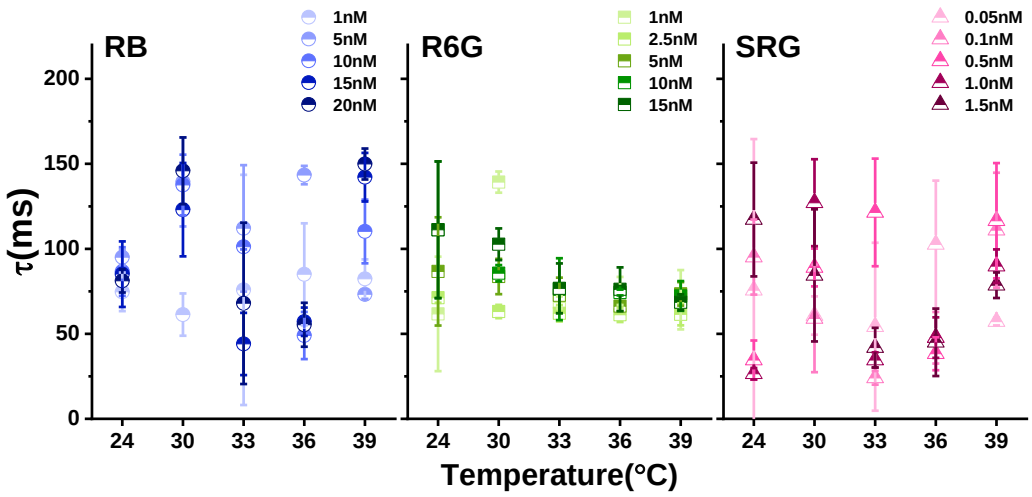

Figure S 4.7 Scatter plots for time constants τ for RB, R6G, and SRG.

Time constant τ were determined by fitting first-order exponential decay in residence time histogram distribution. Error bars in y-axis are standard errors from three measurements.

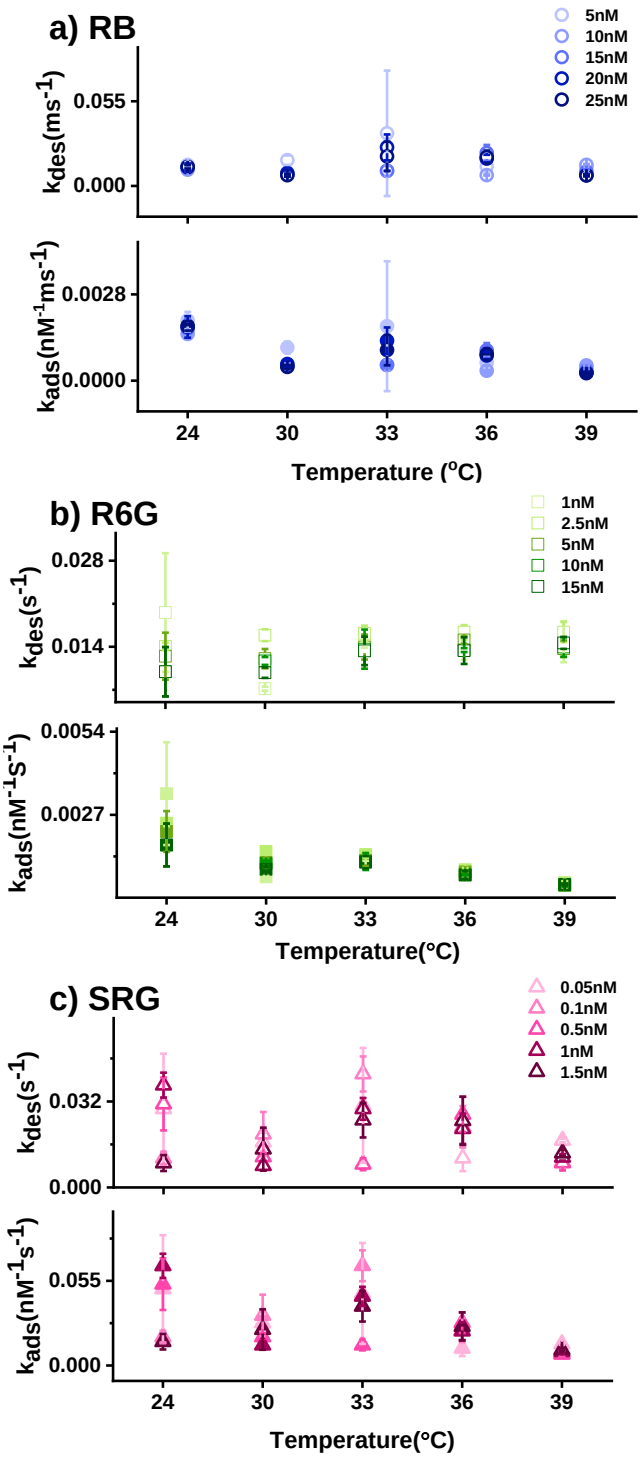

Figure S 4.8 Desorption and adsorption rates for RB (a), R6G(b), and SRG(c) respectively.

Rate constants of desorption are determined using Eq 4.5, and rate constants of adsorption are determined using Eq 4.1. Error bars in y-axis are standard errors from three measurements.

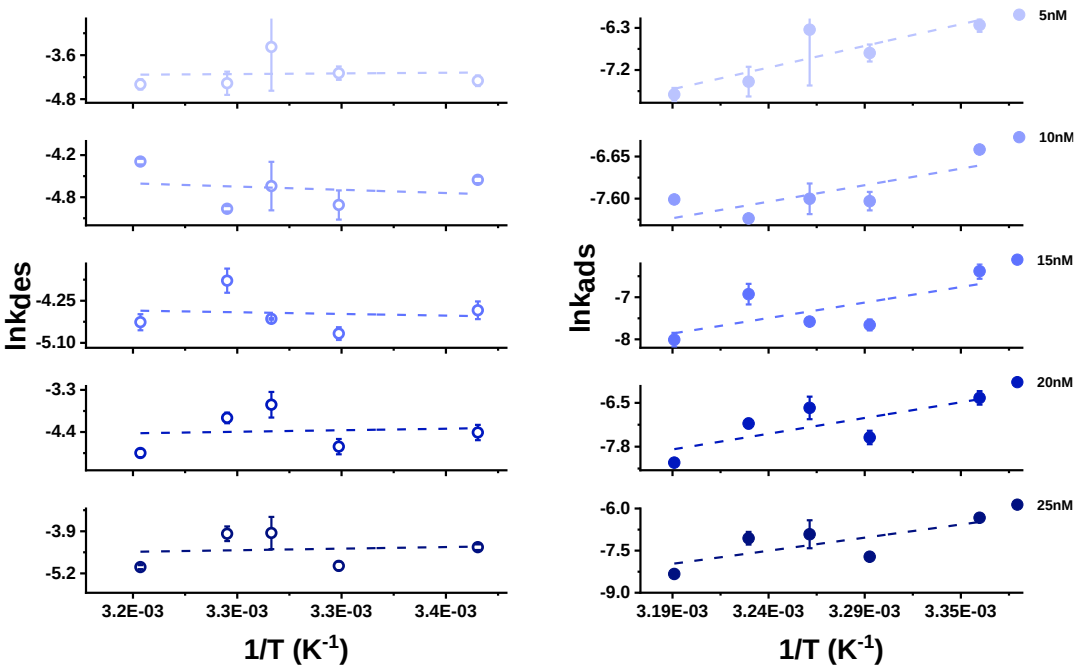

Figure S 4.9 Arrhenius plots for desorption and adsorption for RB

The linear dash line is the best fit line for natural log of desorption rate (left column) or adsorption rate (right column) versus the reciprocal of temperature. Error bars in y-axis are standard errors from three measurements.

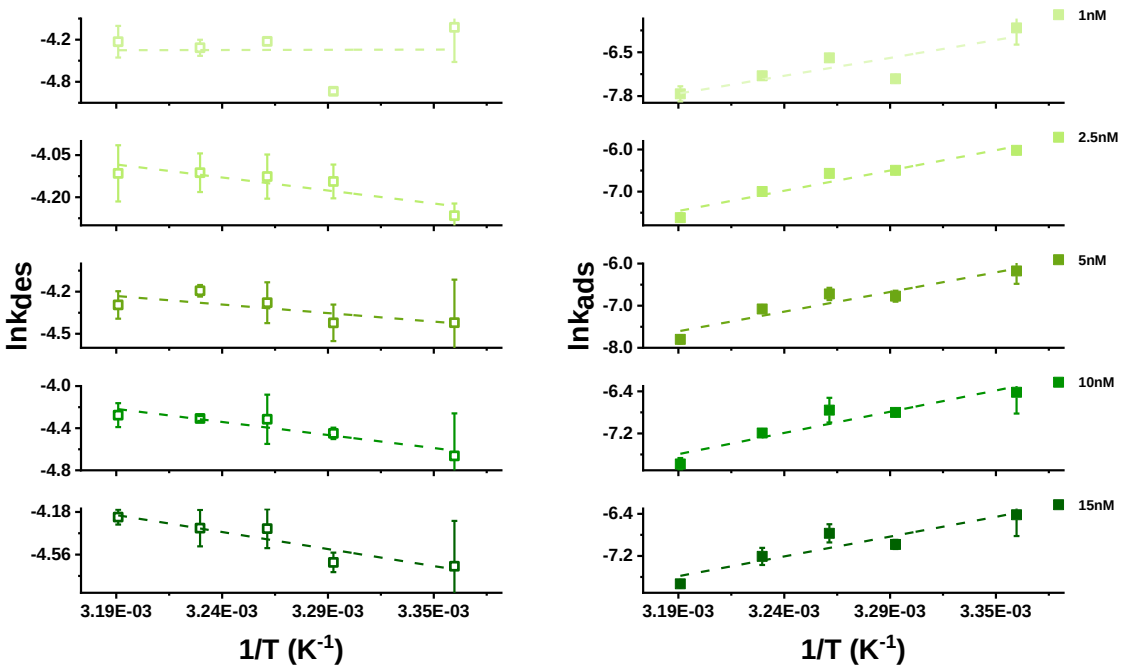

Figure S 4.10 Arrhenius plots for desorption and adsorption for R6G

The linear dash line is the best fit line for natural log of desorption rate (left column) or adsorption rate (right column) versus the reciprocal of temperature. Error bars in y-axis are standard errors from three measurements.

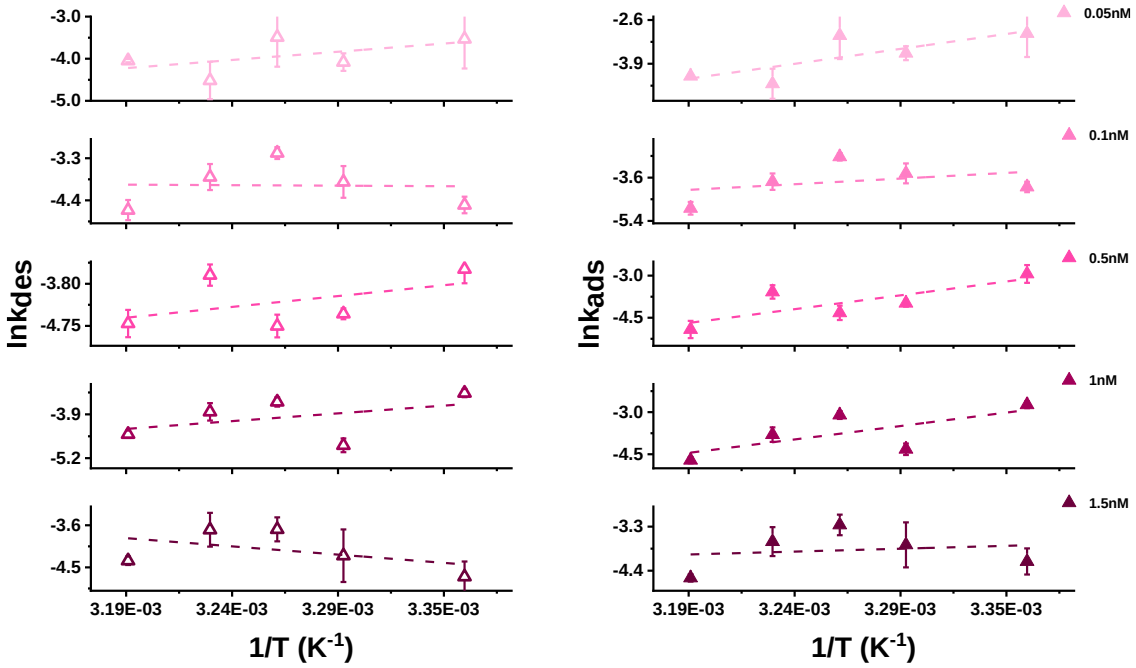

Figure S 4.11 Arrhenius plots for desorption and adsorption for SRG

The linear dash line is the best fit line for natural log of desorption rate (left column) or adsorption rate (right column) versus the reciprocal of temperature. Error bars in y-axis are standard errors from three measurements.

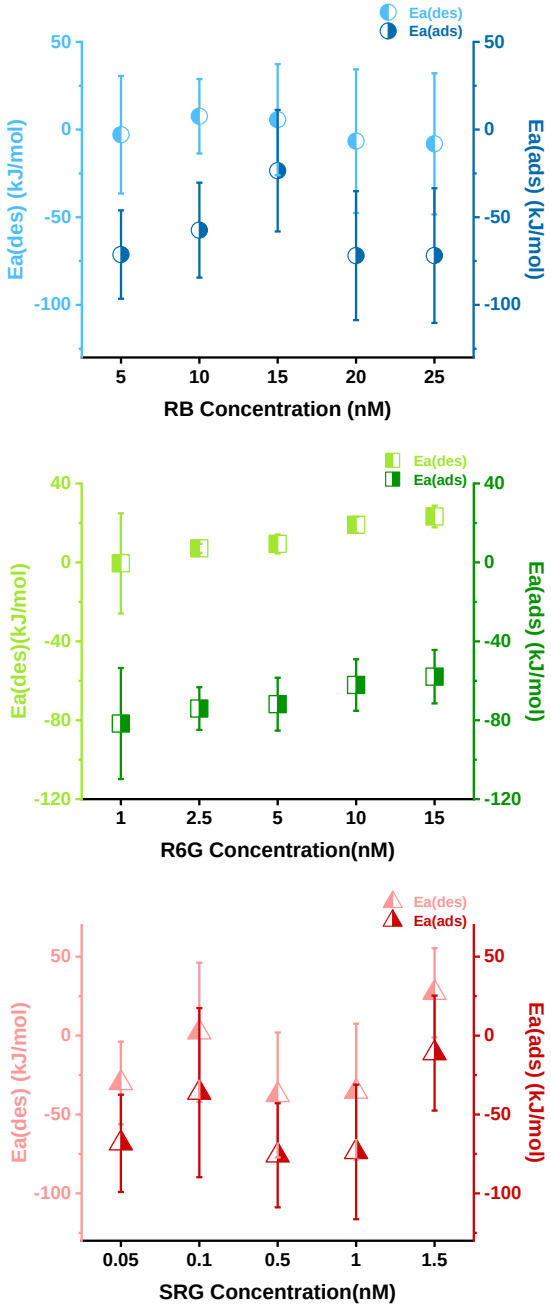

Figure S 4.12 Activation energy of desorption (left x-axis) and adsorption (right x-axis) for rhodamine dyes.

Various concentrations are also plotted for comparison. Error bars in y-axis are standard deviations.

4.8 REFERENCES

(1) Heberle, J.; Riesle, J.; Thiedemann, G.; Oesterhelt, D.; Dencher, N. A. Proton Migration along the Membrane Surface and Retarded Surface to Bulk Transfer. *Nature* **1994**, *370*, 379–382.

(2) Cunliffe, M.; Engel, A.; Frka, S.; Gašparović, B. Ž.; Guitart, C.; Murrell, J. C.; Salter, M.; Stolle, C.; Upstill-Goddard, R.; Wurl, O. Sea Surface Microlayers: A Unified Physicochemical and Biological Perspective of the Air-Ocean Interface. *Prog. Oceanogr.* **2013**, *109*, 104–116.

(3) Abbatt, J. P. D. Interactions of Atmospheric Trace Gases with Ice Surfaces: Adsorption and Reaction. *Chem. Rev.* **2003**, *103*, 4783–4800.

(4) Wren, S. N.; Gordon, B. P.; Valley, N. A.; McWilliams, L. E.; Richmond, G. L. Hydration, Orientation, and Conformation of Methylglyoxal at the Air-Water Interface. *J. Phys. Chem. A* **2015**, *119*, 6391–6403.

(5) Hao, R.; Fan, Y.; Howard, M. D.; Vaughan, J. C.; Zhang, B. Imaging Nanobubble Nucleation and Hydrogen Spillover during Electrocatalytic Water Splitting. *Proc. Natl. Acad. Sci. U. S. A.* **2018**, *115*, 5878–5883.

(6) Oja, S. M.; Guerrette, J. P.; David, M. R.; Zhang, B. Fluorescence-Enabled Electrochemical Microscopy with Dihydroresorufin as a Fluorogenic Indicator. *Anal. Chem.* **2014**, *86*, 6040–6048.

(7) Lu, J.; Fan, Y.; Howard, M. D.; Vaughan, J. C.; Zhang, B. Single-Molecule Electrochemistry on a Porous Silica-Coated Electrode. *J. Am. Chem. Soc.* **2017**, *139*, 2964–2971.

(8) Suvira, M.; Zhang, B. Effect of Surfactant on Electrochemically Generated Surface Nanobubbles. *Anal. Chem.* **2021**, 5170–5176.

(9) Zope, B. N.; Hibbitts, D. D.; Neurock, M.; Davis, R. J. Reactivity of the Gold / Water Interface During Selective Oxidation Catalysis Linked References Are Available on JSTOR for This Article : Reactivity of the Gold / Water Interface. *J. Colloid Interface Sci.* **2019**, *330*, 74–78.

(10) James, R. O.; Healy, T. W. Adsorption of Hydrolyzable Metal Ions at the Oxide-Water Interface. III. A Thermodynamic Model of Adsorption. *J. Colloid Interface Sci.* **1972**, *40*, 65–81.

(11) Zhang, Y.; Cremer, P. S. Interactions between Macromolecules and Ions: The Hofmeister Series. *Curr. Opin. Chem. Biol.* **2006**, *10*, 658–663.

(12) Knipping, A. E. M.; Lakin, M. J.; Foster, K. L.; Jungwirth, P.; Tobias, D. J.; Dabdub, D.; Interfacial, I.; Knipping, E. M.; Lakin, M. J.; Foster, K. L.; et al. Experiments and Simulations of Chemistry on Aqueous NaCl Aerosols. **2020**, *288*, 301–306.

(13) Chen, P.; Zhou, X.; Shen, H.; Andoy, N. M.; Choudhary, E.; Han, K. S.; Liu, G.; Meng, W. Single-Molecule Fluorescence Imaging of Nanocatalytic Processes. *Chem. Soc. Rev.* **2010**, *39*, 4560–4570.

(14) Carrasco, J.; Hodgson, A.; Michaelides, A. A Molecular Perspective of Water at Metal Interfaces. *Nat. Mater.* **2012**, *11*, 667–674.

(15) Limmer, D. T.; Willard, A. P.; Madden, P.; Chandler, D. Hydration of Metal Surfaces Can Be Dynamically Heterogeneous and Hydrophobic. *Proc. Natl. Acad. Sci. U. S. A.* **2013**, *110*, 4200–4205.

(16) Orlando, F.; Waldner, A.; Bartels-Rausch, T.; Birrer, M.; Kato, S.; Lee, M. T.; Proff, C.; Huthwelker, T.; Kleibert, A.; Van Bokhoven, J.; et al. The Environmental Photochemistry of Oxide Surfaces and the Nature of Frozen Salt Solutions: A New in Situ XPS Approach. *Top. Catal.* **2016**, *59*, 591–604.

(17) Taylor, D. J. F.; Thomas, R. K.; Penfold, J. The Adsorption of Oppositely Charged Polyelectrolyte/Surfactant Mixtures: Neutron Reflection from Dodecyl Trimethylammonium Bromide and Sodium Poly(Styrene Sulfonate) at the Air/Water Interface. *Langmuir* **2002**, *18*, 4748–4757.

(18) Chen, Y. R. Surface Properties Probed by Second-Harmonic and Sum-Frequency Generation. *Nature* **1989**, *337*, 519.

(19) Hore, D. K.; Beaman, D. K.; Richmond, G. L. Surfactant Headgroup Orientation at the Air/Water Interface. *J. Am. Chem. Soc.* **2005**, *127*, 9356–9357.

(20) Eisenthal, K. B. Second Harmonic Spectroscopy of Aqueous Nano- and Microparticle Interfaces. *Chem. Rev.* **2006**, *106*, 1462–1477.

(21) Johnson, C. M.; Baldelli, S. Vibrational Sum Frequency Spectroscopy Studies of the Influence of Solutes and Phospholipids at Vapor/Water Interfaces Relevant to Biological and Environmental Systems. *Chem. Rev.* **2014**, *114*, 8416–8446.

(22) Bonn, M.; Nagata, Y.; Backus, E. H. G. Molecular Structure and Dynamics of Water at the Water-Air Interface Studied with Surface-Specific Vibrational Spectroscopy. *Angew. Chemie - Int. Ed.* **2015**, *54*, 5560–5576.

(23) Onorato, R. M.; Otten, D. E.; Saykally, R. J. Adsorption of Thiocyanate Ions to the Dodecanol/Water Interface Characterized by UV Second Harmonic Generation. *Proc. Natl. Acad. Sci. U. S. A.* **2009**, *106*, 15176–15180.

(24) Otten, D. E.; Shaffer, P. R.; Geissler, P. L.; Saykally, R. J. Elucidating the Mechanism of Selective Ion Adsorption to the Liquid Water Surface. *Proc. Natl. Acad. Sci. U. S. A.* **2012**, *109*, 701–705.

(25) McCaffrey, D. L.; Nguyen, S. C.; Cox, S. J.; Weller, H.; Alivisatos, A. P.; Geissler, P. L.; Saykally, R. J. Mechanism of Ion Adsorption to Aqueous Interfaces: Graphene/Water vs. Air/Water. *Proc. Natl. Acad. Sci. U. S. A.* **2017**, *114*, 13369–13373.

(26) Plath, K. L.; Valley, N. A.; Richmond, G. L. Ion-Induced Reorientation and Distribution of Pentanone in the Air-Water Boundary Layer. *J. Phys. Chem. A* **2013**, *117*, 11514–11527.

(27) Hao, R.; Peng, Z.; Zhang, B. Single-Molecule Fluorescence Microscopy for Probing the Electrochemical Interface. *ACS Omega* **2020**, *5*, 89–97.

(28) Peterson, E. M.; Manhart, M. W.; Harris, J. M. Single-Molecule Fluorescence Imaging of Interfacial DNA Hybridization Kinetics at Selective Capture Surfaces. *Anal. Chem.* **2016**, *88*, 1345–1354.

(29) Peterson, E. M.; Reece, E. J.; Li, W.; Harris, J. M. Super-Resolution Imaging of Competitive Unlabeled DNA Hybridization Reveals the Influence of Fluorescent Labels on Duplex Formation and Dissociation Kinetics. *J. Phys. Chem. B* **2019**, *123*, 10746–10756.

(30) Myers, G. A.; Gacek, D. A.; Peterson, E. M.; Fox, C. B.; Harris, J. M. Microscopic Rates of Peptide−Phospholipid Bilayer Interactions from Single-Molecule Residence Times. **2012**.

(31) Bartell, F. E., Tudor L. Thomas, and Y. F. Thermodynamics of Adsorption from Solutions. IV. Temperature Dependence of Adsorption. *J. Phys. Chem.* **1951**, *55*, 1456–1462.

(32) Hao, R.; Fan, Y.; Zhang, B. Imaging Dynamic Collision and Oxidation of Single Silver Nanoparticles at the Electrode/Solution Interface. *J. Am. Chem. Soc.* **2017**, *139*, 12274−12282.

Chapter 5. ONGOING AND FUTURE WORK

5.1 SINGLE NANOELECTRODE

We primarily focused on using TIRF microscopy to study surface nanobubbles generated on a macro-ITO (a circular area with a diameter of 2mm) electrode via fluorophore labeling. Bubbles are generated stochastically at the ITO surface, It, however, limits our ability to further investigate the individual bubbles' generation and growth. Besides imaging, White and coworkers have been working on the electrogenerated single nanobubbles at a nanodisk electrodes, where the i-V response was associated with bubble nucleation (Figure 5.1).[1-4] In Figure 5.1B, as the electrode potential is scanned towards negative, the current from H_2 generation begins to increase (negative sign denotes a cathodic current). After passing through the peak current, the current suddenly drops, indicating the formation of a nanobubble at the electrode surface that partially blocks the proton transfer to the electrode surface. This method enables a direct and quick responsive measurement for nanobubble generation. However, it is limited to its critical condition for nanobubble formation, such as electrode size and proton concentration. Thus, we aim to combine TIRF imaging and single nanoelectrode to further study nanobubble nucleation and growth. There are many fundamental topics could be studied by doing this experiment, such as 1) the critical condition forming nanobubbles; 2) effect of size and shape of the nanobubbles; 3) the time required to label nanobubble after it is formed, etc.

The fabrication is illustrated in Figure 5.2. The transparent ITO acts as a working electrode, allowing light transmittance for TIRF imaging. A thin layer of nitride is deposited using Plasma-enhanced chemical vapor deposition (PECVD), then sputter coated with 20 nm chromium to act

as a hard mask. The mask is patterned with focused ion beam (FIB), then a nanometer size region of ITO is exposed by reactive ion etching of the nitride.

5.2 DUAL-COLOR LABELING

Fluorescence microscopy enables noninvasive imaging of biological samples.[5] The availability of multicolored fluorophores and the ability to label specific targets enable visualization of molecular interactions in biological samples.[6,7] Dual-color fluorescence microscopy with sub-diffraction resolution (20-30nm) were reported.[8,9] To utilize the stochastic reconstruction, we hypothesized that having multiple fluorophores may enable to extract useful information about a bubble's lateral dimension. The idea is illustrated in Figure 5.3. This is based on the assumption that dye molecules can freely move at bubble surface, resulting in multiple dye molecules coexist at the same bubble. This could give a slight difference in the detection location, enabling us to estimate the lateral dimension of a bubble.

5.3 EMISSION SPECTRUM OF NILE RED AT BUBBLE SURFACE

In Chapter 3, we observed that Nile red can label nanobubble, indicating that the gas/liquid interface is somehow nonpolar enough to enable Nile red to fluoresce. However, the transition of hydrophobicity from water to gas phase is rarely studied. There are some fundamental questions could be explored: 1) how thick is gas-liquid interface; 2) how does the size of bubbles affect the thickness of the interface; 3) how does the transition of hydrophobicity of interface look like from water to gas phase. To answer these questions, Nile red is an ideal fluorophore since its emission spectra red shifts from nonpolar to polar medium. In other words, by measuring the emission spectrum of Nile red at bubble surface, the surface hydrophobicity can be determined. Toward this goal, there are two approaches: 1) spectrally resolved STORM (SR-STORM).[10] 2) spectrometer.

By replacing the camera with spectrometer would be a straightforward way to collect emission spectrum. This method requires an additional signal magnification so that the single molecule fluorescence emission can be captured by the spectrometer. SR-STORM would be preferred since it can obtain both spatial and spectral information. SR-STORM was developed by Xu and coworkers in 2015.[11,12] Theoretically, a single molecule emits fluorescent that can be dispersed into a spectrum. In the case of multiple molecules, spectrum of each molecule could be measured simultaneously. To avoid spectrum overlapped, Xu and coworkers demonstrated that by selectively photo-switching fluorophores, fluorescence can be dispersed into induvial spectra.[11,12] This method allows spectrum measurement and superlocalization of millions of single molecules within minutes. Scheme of SR-STORM is shown in Figure 5.4. To obtain the spatial and spectral information of a randomly located single molecule, it is essential to decouple the two without sacrificing the obtained signal. Xu and coworkers employed a dual-objective setup where the emitted light was traveling through two paths (Figure 5.4; paths 1 and 2). The image obtained through path 1 was used to determine the position of each molecule. While in path 2, a dispersing prism was placed to generate spectra of the same molecules. By coupling SR-STORM to our current TIRF setup, we are able to obtain the Nile red emission spectrum at the bubble surface, which can be used to estimate the hydrophobicity of gas/liquid interface.

5.4 FIGURES

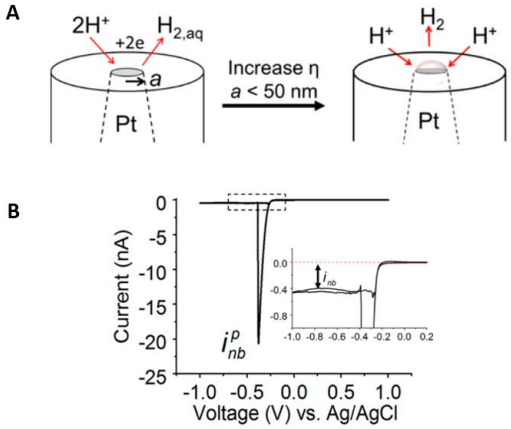

Figure 5.1 Scheme of a single nanoelectrode for bubble generation and current response of a single Pt electrode

(A) Schematic of the electrochemical formation of an individual nanobubble at a Pt nanodisk electrode with a radius of a <50 nm (B) Cyclic voltammogram (CV) recorded for a 27-nm-radius Pt electrode immersed in a deoxygenated 0.5 M H_2SO_4 solution (scan rate = 100 mV/s). The transport-limited current associated with the electroreduction of H^+ drops suddenly at ∼−0.4 V versus Ag/AgCl because of the nucleation and rapid growth of a H_2 nanobubble. The inset shows a residual current after the formation of a nanobubble. Reprinted with permission from Luo, L.; White, H. S. Electrogeneration of Single Nanobubbles at Sub-50-nm-Radius Platinum Nanodisk Electrodes. *Langmuir* **2013**, *29*, 11169–11175 (ref 1). Copyright 2013 American Chemical Society.

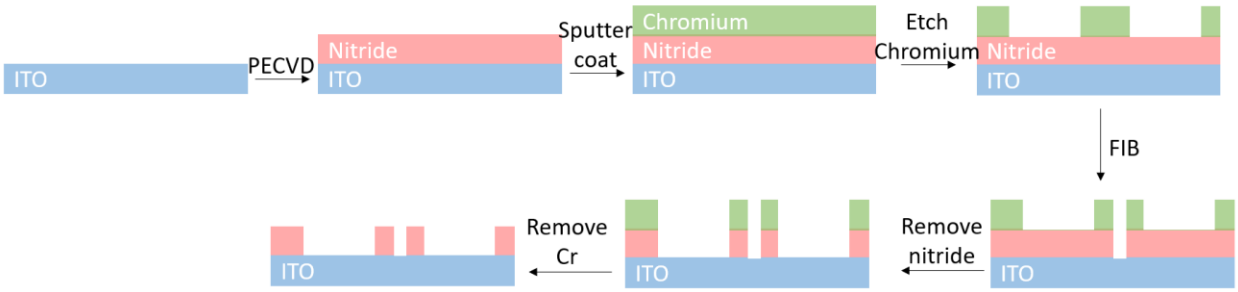

Figure 5.2 Schematic of single nanoelectrode fabrication

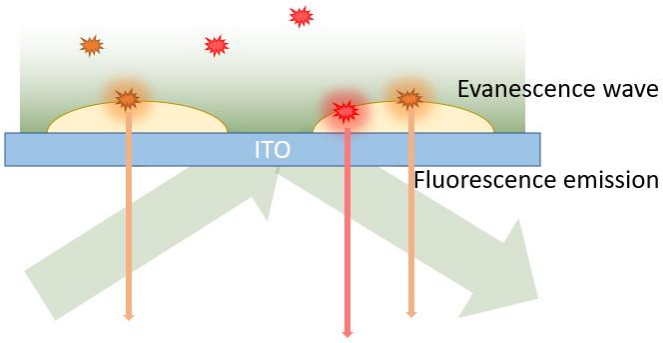

Figure 5.3 Schematic of dual-color labeling.

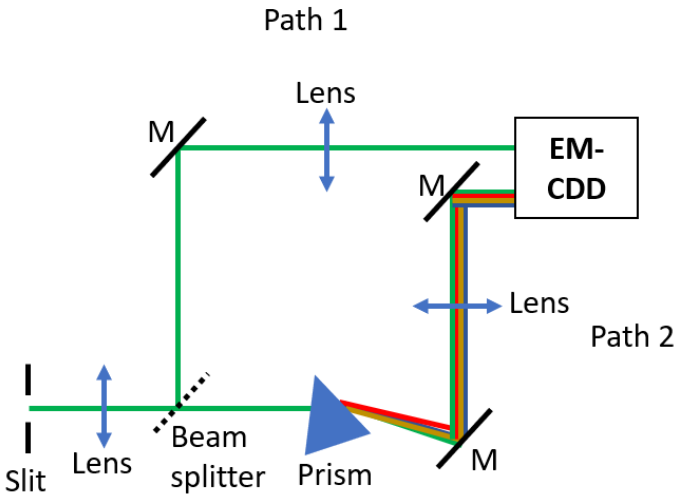

Figure 5.4 Schematic of SR-STROM setup

5.5 REFERENCES

(1) Luo, L.; White, H. S. Electrogeneration of Single Nanobubbles at Sub-50-Nm-Radius Platinum Nanodisk Electrodes. *Langmuir* **2013**, *29*, 11169–11175.

(2) German, S. R.; Chen, Q.; Edwards, M. A.; White, H. S. Electrochemical Measurement of Hydrogen and Nitrogen Nanobubble Lifetimes at Pt Nanoelectrodes. *J. Electrochem. Soc.* **2016**, *163*, H3160–H3166.

(3) German, S. R.; Edwards, M. A.; Chen, Q.; White, H. S. Laplace Pressure of Individual H2 Nanobubbles from Pressure-Addition Electrochemistry. *Nano Lett.* **2016**, *16*, 6691–6694.

(4) Chen, Q.; Luo, L.; Faraji, H.; Feldberg, S. W.; White, H. S. Electrochemical Measurements of Single H2 Nanobubble Nucleation and Stability at Pt Nanoelectrodes. *J. Phys. Chem. Lett.* **2014**, *5*, 3539–3544.

(5) Ettinger, A.; Wittmann, T. Fluorescence Live Cell Imaging. *Methods Cell Biol* **2014**, *123*, 77–94.

(6) Chen, X.; Liu, Z.; Li, R.; Shan, C.; Zeng, Z.; Xue, B.; Yuan, W.; Mo, C.; Xi, P.; Wu, C.; et al. Multicolor Super-Resolution Fluorescence Microscopy with Blue and Carmine Small Photoblinking Polymer Dots. *ACS Nano* **2017**, *11*, 8084–8091.

(7) Abdeladim, L.; Matho, K. S.; Clavreul, S.; Mahou, P.; Sintes, J. M.; Solinas, X.; Arganda-Carreras, I.; Turney, S. G.; Lichtman, J. W.; Chessel, A.; et al. Multicolor Multiscale Brain Imaging with Chromatic Multiphoton Serial Microscopy. *Nat. Commun.* **2019**, *10*, 1–14.

(8) Andresen, M.; Stiel, A. C.; Fölling, J.; Wenzel, D.; Schönle, A.; Egner, A.; Eggeling, C.; Hell, S. W.; Jakobs, S. Photoswitchable Fluorescent Proteins Enable Monochromatic Multilabel Imaging and Dual Color Fluorescence Nanoscopy. *Nat. Biotechnol.* **2008**, *26*, 1035–1040.

(9) Shroff, H.; Galbraith, C. G.; Galbraith, J. a; White, H.; Gillette, J.; Olenych, S.; Davidson, M. W.; Betzig, E. Dual-Color Superresolution Imaging of Genetically Expressed Probes within Individual Adhesion Complexes. *Proc. Natl. Acad. Sci. U. S. A.* **2007**, *104*, 20308–20313.

(10) Zhang, Z.; Kenny, S. J.; Hauser, M.; Li, W.; Xu, K. Ultrahigh-Throughput Single-Molecule Spectroscopy and Spectrally Resolved Super-Resolution Microscopy. *Nat. Methods* **2015**, *12*, 935–938.

(11) Fölling, J.; Bossi, M.; Bock, H.; Medda, R.; Wurm, C. A.; Hein, B.; Jakobs, S.; Eggeling, C.; Hell, S. W. Fluorescence Nanoscopy by Ground-State Depletion and Single-Molecule Return. *Nat. Methods* **2008**, *5*, 943–945.

(12) Rust, M.; Bates, M.; Zhuang, X. Sub-Diffraction-Limit Imaging by Stochastic Optical Reconstruction Microscopy (STORM). *Nat. Methods* **2006**, *3*, 793–795.

VITA

Zhuoyu Peng was born and raised in Guangdong, China, where she finished her high school. In 2015, she received the degree of Bachelor of Science in Chemistry at the University of Michigan, Ann Arbor. The following September, she joined the University of Washington to pursue her Ph.D in chemistry.